Ultrafast Mid-IR Nonlinear Optics in Gas-filled Hollow-core Photonic Crystal Fibers

Habib, Selim

Publication date:
2017

Document Version
Publisher's PDF, also known as Version of record

DTU Fotonik
Department of Photonics Engineering

Ultrafast Mid-IR Nonlinear Optics in Gas-filled Hollow-core Photonic Crystal Fibers

PhD Thesis

Md. Selim Habib
April 2017

Ultrafast Infrared and Terahertz Science
Department of Photonics Engineering
Technical University of Denmark
Kgs. Lyngby, DK-2800.

Abstract

Invention of hollow-core fiber has been proven an ideal medium to study light-gas interaction. Tight confinement of light inside hollow-core fiber allows unremitting and tailored interaction between light and gas over long distances. In this work, we used a special kind of hollow-core fiber – hollow-core anti-resonant (HC-AR) fiber to study the various nonlinear effects filled with Raman free noble gas. One of the main striking features of HC-AR fiber is that ~99.99% light can be guided inside the central hollow-core region, which significantly enhances damage threshold level. HC-AR fiber can sustain 10s of μJ pulse energies, tolerate mutiple-watts of average powers, provide a clean spatial mode profile and give flexible beam handling and delivery. It also offers relatively low-loss, broadband guidance, and low anomalous group-velocity dispersion (GVD). Both the dispersion and nonlinearity can be tuned by simply changing the pressure of the gas while at the same time providing extremely wide transparency ranges. In this thesis, we propose several low-loss broadband guidance HC-AR fibers and investigate soliton-plasma dynamics using HC-AR fiber filled with noble gas in the mid-IR.

The combined action of self-focusing self-phase modulation (SPM) and anomalous GVD allows strong soliton self-compression down to sub-single cycle duration inside HC-AR fiber. The peak intensity at the maximum temporal compression can reach over 10^{14} W/cm^2 which is sufficient to ionize the gas and form a plasma.

We investigate numerically soliton-plasma interaction in a noble-gas-filled silica HC-AR fiber pumped in anomalous dispersion regime at 3.0 μm. We observe multiple soliton self-compression stages due to distinct stages where either the self-focusing or the self-defocusing nonlinearity dominates. Specifically, the parameters may be tuned so the

competing plasma self-defocusing nonlinearity only dominates over the Kerr self-focusing nonlinearity around the soliton self-compression stage, where the increasing peak intensity on the leading pulse edge initiates a competing self-defocusing plasma nonlinearity acting nonlocally on the trailing edge, effectively preventing soliton-formation there. As the plasma switches off after the self-compression stage, self-focusing dominates again, initiating another soliton self-compression stage in the trailing edge. This process is accompanied by supercontinuum generation spanning $1-4$ μm. We also demonstrate coherence of the supercontinuum and find that the spectral coherence drops as the secondary compression stage is initiated.

Resumé

Opfindelsen af hul-kerne fiberen har vist sig et ideelt medie til at studere lys-gas interaktion. Tæt indespærring af lys i en hul-kerne fiber tillader utrættelig og skræddersyet vekselvirkning mellem lys og gas over lange afstande. I dette arbejde anvendte vi en særlig slags hul kerne anti-resonant (HC-AR) fiber til at undersøge de forskellige ikke-lineære effekter i Raman fri ædelgas. Et af de vigtigste slående træk ved HC-AR fiber er at ~99,99 % af lyset let kan føres ind i den centrale hulkerne region, hvilket væsentligt forøger tærsklen for optisk skade på fiberen. HC-AR fiber kan opretholde mere end J puls energi, tolerere adskillige Watt gennemsnitseffekt, give en ren rumlig mode profil og give fleksibel lysstråle håndtering og levering. Den medfører også relativt lavt tab, bredbåndet lysledning, og lav anomal gruppe-hastighed dispersion (GVD). Både dispersionen og ikke-lineariteten kan ændres ved blot at ændre trykket af gassen, og på samme tid give ekstremt brede bånd med spektral gennemsigtighed. I denne afhandling foreslår vi flere lav–tabs, bredbåndede og lysledende HC-AR fibre, og undersøger soliton-plasma dynamik igennem HC-AR fibre fyldt med ædelgas i mid-IR.

Den kombinerede virkning af selv-fokusering, selvfasemodulation (SPM) og anomal GVD tillader stærk soliton selv-kompression ned til under en enkelt optiskcyklus varigheden inde HC-AR fiberen. Topintensiteten ved den maksimale tidsmæssige kompression kan nå over 10^{14} W/cm^2, hvilket er tilstrækkeligt til at ionisere gas og danne et plasma.

Vi undersøger numerisk soliton-plasma interaktion i en ædel-gasfyldt silikat HC-AR fiber pumpet i det anormale dispersions regime ved 3,0 μm. Vi observerer flere soliton selv-kompressionstrin på grund af forskellige stadier, hvor enten den selv-fokuserende eller den selv-

defokuserende ikke-linearitet dominerer. Mere specifikt kan parametrene indstilles således at den konkurrerende plasma selv-defokuserende ikke-linearitet kun dominerer over den Kerr selv-fokuserende ikke-linearitet omkring soliton selv-kompressionstrinnet, hvor den stigende topintensitet forrest på impulskanten sætter gang i en konkurrerende selv-defokuserende plasma ikke-linearitet, der påvirker pulsen ikke-lokalt på bagkanten, hvilket effektivt forhindrer soliton-formation. Som plasmaet slukker efter selv-kompressionstrinnet vil selv-fokusering igen dominere, hvilket giver anledening til endnu et soliton selv-kompressionstrin på bagkanten af pulsen. Denne proces ledsages af superkontinuum generering der breder sig over 1-4 μm. Vi demonstrerer også kohærensen af dette superkontinuum og finder, at den spektrale kohærens falder når den sekundære kompressions fase påbegyndes.

Preface

The PhD project titled "Ultrafast mid-IR nonlinear optics in gas-filled hollow-core photonic crystal fibers," was performed at the Department of Photonics Engineering (DTU Fotonik), Technical University of Denmark during a three-year period from 2014-2017. The PhD project is funded by basic funding of the Department of Photonics Engineering. The project was supervised by Associate Professor Morten Bache as main supervisor and Professor Ole Bang as co-supervisor.

Md. Selim Habib
April 14, 2017

Acknowledgements

I would like to thank, most of all, my supervisors Associate Professor Morten Bache and Professor Ole Bang for giving me the opportunity to work with the exciting topics in the field of gas-filled hollow-core fibers. I also wish to express my sincere gratitude for their contribution to the actual research presented in this thesis, for the guidance in writing the publications and preparing the thesis. I would also like to thank for your fruitful scientific discussions and suggestions, for generously sharing your knowledge, without which it would not be possible to finish this project. I do really learn a lot during my PhD and happy to work with you.

During my external stay at CREOL, The College of Optics and Photonics, University of Central Florida, USA, I had the opportunity to work with Professor Rodrigo Amezcua-Correa. I would also like to thank Dr. Jose Enrique Antonio-Lopez for helping in drawing hollow-core anti-resonant fiber and measuring the transmission and loss spectra of hollow-core anti-resonant fiber.

I wish to thank all of my colleagues and friends at DTU Fotonik for their continuous support. I would like to thank Dr. Irnis Kubat (now at NKT Photonics), Dr. Christian Rosenberg Petersen, Ivan Bravo Gonzalo, and Rasmus Dybbro Engelsholm for fruitful discussions regarding nonlinear optics.

I would like to thank Anders Nysteen, Xing Liu, Christine Pepke Pedersen, Abebe Tilahun Tarekegne, Simon Lehnskov Lange, Daena Madhi, Md Nooruzzaman, Kabir Hossain, and so on for various scientific and non-scientific discussions at my office.

I would also like to thank Dr. John Travers, Dr. Muhammad Saleh, and Dr. Wonkeun Chang for fruitful discussion with the unidirectional pulse propagation equation and ionization rate equation.

I wish to thank Dr. Francesco Poletti, Dr. Walter Belardi, and Dr. Mattia Michieletto for useful discussion with the hollo-core fiber modelling.

Special thanks to Dr. Christos Markos for various scientific discussion with me on hollow-core fiber design, gas-filled fibers and fruitful discussion on my research papers.

Last but not the least; I would like to thank my parents, family members, and all of my teachers for the continuous support during my study.

Finally, my lovely wife Maisha Roushan, I am really grateful for your continuous inspiration and support, being with me away from our family members during the past two years. I would like to dedicate my thesis to my parents and my wife.

Abbreviations

ADK	Ammosov, Delone, and Krainov
ARROW	Anti-resonant reflecting optical waveguide
FWHM	Full width half maximum
GNLSE	Generalized Nonlinear Schrödinger equation
GVD	Group velocity dispersion
HC-AR	Hollow-core anti-resonant
HOMER	Higher-order-mode extinction ratio
mid-IR	Mid Infrared
Near-IR	Near Infrared
NLSE	Nonlinear Schrödinger equation
OSA	Optical spectrum analyzer
PPT	Perelomov, Popov and Terent'ev
SEM	Scanning electron microscope
SPM	Self-phase modulation
SMF	Single-mode fiber
UPPE	Unidirectional pulse propagation equation
UV	Ultra-violet
DUV	Deep ultra-violet
ZDW	Zero dispersion wavelength

List of Publications

Journal Publications

Paper I **M. S. Habib**, O. Bang, and M. Bache, "Low-loss hollow-core silica fibers with adjacent nested anti-resonant tubes," Opt. Express, **23**, 17394 (2015).

Paper II **M. S. Habib**, O. Bang, and M. Bache, "Low-loss single-mode hollow-core fiber with anisotropic anti-resonant elements," Opt. Express, **24**, 8429 (2016).

Paper III **M. S. Habib**, O. Bang, and M. Bache, "Low-loss hollow-core anti-resonant fibers with semi-circular nested tubes," IEEE J. Sel. Top. Quantum Electron. **22**, 4402107 (2016).

Paper IV **M. S. Habib**, C. Markos, O. Bang, and M. Bache, "Soliton-plasma nonlinear dynamics in mid-IR gas-filled hollow-core fibers," Opt. letters **42**, 2232 (2017).

Conference contributions

Paper C1 **M. S. Habib**, O. Bang, and M. Bache, "Low Loss Double-clad Hollow Core Anti-Resonant Fibers in the Mid-IR," in CLEO/Europe, Munich, paper CJP12 (2015).

Paper C2 **M. S. Habib**, O. Bang, and M. Bache, "Improved Low-loss Hollow Core Anti-Resonant Silica Mid-IR Fibers," in CLEO/Europe, Munich, paper CJP22 (2015).

Paper C3 **M. S. Habib**, O. Bang, and M. Bache, "Anisotropic Anti-resonant Elements gives Broadband Single-mode Low-loss Hollow-core Fibers," in CLEO/USA, San Jose,

paper JTu5A.99 (2016).

Paper C4 **M. S. Habib**, O. Bang, and M. Bache, "Low Loss Mid-IR Transmission Bands Using Silica Hollow-core Anisotropic Anti-resonant Fibers," in International Conference on Infrared, Millimeter and Terahertz Waves, Copenhagen, Denmark.

Paper C5 J. E. A. Lopez, **M. S. Habib**, A. V. Newkirk, G. Lopez-Galmiche, Z. S. Eznaveh, J. C. Alvarado-Zacarias, O. Bang, M. Bache, A. S, and R. Amezcua-Correa, "Anti-resonant hollow core fiber with seven nested capillaries," in IEEE photonics conference, Hawaii, USA (2016).

Paper C6 **M. S. Habib**, C. Markos, O. Bang, and M. Bache, "Multiple soliton compression stages in mid-IR gas-filled hollow-core fibers," accepted to CLEO/Europe, Munich, (2017).

Paper C7 **M. S. Habib**, C. Markos, O. Bang, and M. Bache, "Generation of multiple VUV dispersive waves using a tapered gas-filled hollow-core anti-resonant fiber," accepted to CLEO/Europe, Munich, (2017).

Paper C8 **M. S. Habib**, C. Markos, O. Bang, and M. Bache, "Curvature and position of nested tubes in hollow-core anti-resonant fibers," accepted to CLEO/Europe, Munich, (2017).

Paper C9 **M. S. Habib**, J. E. A. Lopez, A. V. Newkirk, J. C. Alvarado-Zacarias, R. Amezcua-Correa, C. Markos, O. Bang, and M. Bache, "Toward single-mode UV to near-IR guidance using hollow-core anti-resonant silica fiber," accepted to CLEO/Europe, Munich, (2017).

Author's contribution

The key results found in this PhD project are given below.

Paper I In this paper we show that re-arranging the nested anti-resonant tubes in the cladding to be adjacent has the effect of significantly reducing leakage as well as bending losses, and for reaching high loss extinction ratios between the fundamental mode and higher order modes. Our proposed design is superior with respect to obtaining the lowest leakage losses and the bend losses are also much lower than for the previous designs. Leakage losses as low as 0.0015 dB/km and bending losses of 0.006 dB/km at 5 cm bending radius are predicted at the ytterbium lasing wavelength 1.06 μm. We show that the higher-order-mode extinction ratio is more than 1500 in the range 1.0-1.1 μm around the ytterbium lasing wavelength, while in the mid-IR it can be over 100 around λ =2.94 μm.

Paper II A hollow-core fiber using anisotropic anti-resonant tubes in the cladding is proposed for low loss and effectively single-mode guidance. We show that the loss performance and higher-order mode suppression is significantly improved by using symmetrically distributed anisotropic anti-resonant tubes in the cladding, elongated in the radial direction, when compared to using isotropic, i.e. circular, anti-resonant tubes. The effective single-mode guidance of the proposed fiber is achieved by enhancing the coupling between the cladding modes and higher-order-core modes by suitably engineering the anisotropic anti-resonant elements.

Paper III The role of curvature and separation between the nested tubes on the overall loss performance and single-mode

guidance is investigated thoroughly in this paper. We find that the loss performance is quite insensitive to the curvature of the nested element, while the distance from the core boundary to the outer perimeter of the nested element is much more critical.

Paper IV We investigate numerically soliton-plasma interaction in a noble-gas-filled silica hollow-core anti-resonant fiber pumped in the mid-IR at 3.0 μm. Interestingly, we find a novel soliton dynamics scenario where multiple soliton self-compression stages are observed, which we explain as a direct consequence having distinct propagation stages with either the self-focusing or the self-defocusing nonlinearity dominates. This happens for certain system parameter ranges, mainly involving moderate gas pressure and input pulse intensities. A supercontinua covering $1-4$ μm is also observed.

Contents

Chapter 1

Introduction

Light guidance in hollow-core photonic crystal fibers (HC-PCFs) also named as hollow-core fibers (HCFs) [1]–[3] has enabled new applications due to their extraordinary properties compared to solid-core fibers: when light propagates in a gas-filled core instead of glass, it propagates faster and often with low dispersion, and the gas tolerates extremely large pulse energies and allow tunable control over dispersion and nonlinearity through pressure [4]. These fibers are promising candidates for applications such high-power [5] and ultra-short pulse delivery [6], pulse compression [7], mid-IR transmission [8], telecommunication [9], terahertz applications [10].

HCF allows diffraction-free propagation and enhanced light-gas interaction over long distances when the fiber is filled with gas. Gas-filled HCF has applications such as soliton pulse compression [11], [12], supercontinuum generation [13], UV-light generation [12], soliton-plasma dynamics [4], [11], [14], [15] and so on.

Two categories of single-material hollow-core fibers have been studied and designed in the previous decade. The first one is a hollow-core photonic bandgap (HC-PBG) fiber shown in Fig. 1.1(a), which guides light in the air-core using a 2D periodic cladding structure showing a photonic band gap [1]. Thus, the cladding does not support modes for a certain range of optical frequencies and propagation constants. In these ranges the core mode is not able to couple with cladding modes and is thus guided in the hollow air-core. However, the HC-PBG fiber suffers from limited transmission bandwidth [16], strong power overlap of the core modes with the glass cladding and high group-velocity dispersion

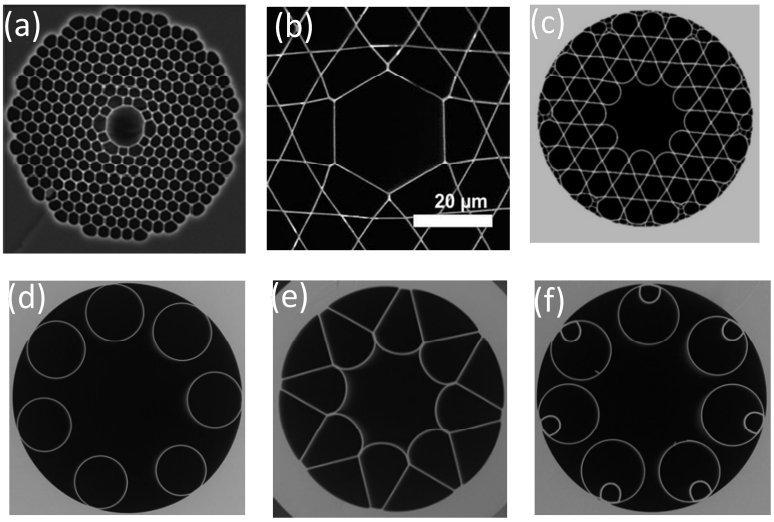

Figure 1.1. SEM image of (a) HC-PBG fiber (image courtesy: NKT photonics A/S), (b) Kagome HCF [15], (c) Hypocycloid kagome HCF [17], (d) node-free HC-AR fiber, (e) Ice-cream cone shape HC-AR fiber, and (f) Node-free nested HC-AR fiber (image courtesy (d-f): Microstructured Fibers and Devices Group, CREOL, University of Central Florida, USA).

(especially at the band-gap edges) which hinders some of the nonlinear applications such as intense few cycle pulse generation and supercontinuum generation. The lowest transmission loss reported of this kind of fiber is 1.2 dB/km at 1.62 μm [18].

The second fiber category, which guides light via inhibited coupling (IC) between the core and cladding modes and the anti-resonant effect [19]–[21], include also the so-called hollow-core anti-resonant (HC-AR) fibers. The overlap integral between the cladding modes and the core modes can be strongly reduced by carefully engineering the interaction between the cladding modes and the core modes [22]–[24]. This concept is known in quantum mechanics/condensed matter as "quasi-bound or bound state in a continuum". This type of fiber allows much broader spectral bandwidths than that achieved in HC-PBG fibers. An example of hollow-core fibers guiding via inhibited coupling is the Kagome fiber

[25], [26] which is shown in Fig. 1.1(b). Several Kagome fibers with different core shapes and sizes have been studied and developed to date for controlling the leakage loss (also known as confinement loss) and modal properties [3], [17], [25], [27]. The reported results so far in [3], [17], [25], [27] show that the core shape plays a vital role for the modal content for example when the core shape is hypocycloid type [3], [17], the power fraction in silica, and the leakage loss. The lowest reported transmission loss of a Kagome fiber was 30 dB/km at 1.55 µm, which was measured in a so-called hypocycloid-core Kagome fiber [27].

Other types of HC-AR fibers with low losses have been proposed and developed by several research groups as an alternative optical transmission medium in spectral ranges with high material loss [20], [28]–[33]. All of the proposed designs have used "negative-curvature" core boundaries (just like the hypocycloid-core Kagome fiber [3]), as these fibers offer broad transmission bands and low losses due to both a low leakage loss and a weak overlap of the core modes with the silica part of the fiber [29]–[33]. A particularly simple HC-AR fiber design is proposed where a silica capillary has a periodic arrangement of smaller silica "cladding tubes" acting as anti-resonant elements that define the negative-curvature core which is shown in Fig. 1.1(d). It was first demonstrated in [33] that such a fiber guides light even at mid-IR wavelengths above 3.5 μm, despite the very high material loss of silica in this spectral regime.

An ice-cream cone shape negative-curvature HC-AR fiber was fabricated and demonstrated [29] to have a transmission loss of only 34 dB/km at 3.05 μm, and transmission of wavelengths beyond 4 μm was also demonstrated. The fiber design is shown in Fig. 1.1(e).

Recently, a modified form of HC-AR fibers has been introduced [31], where smaller tubes are nested inside the tubes defining the core which is shown in Fig. 1.1(f). This reduces the coupling between the fundamental core mode and the cladding modes, and thereby the leakage loss

is reduced. Leakage losses at 3.05 μm were predicted to be below 0.1 dB/km using a single nested anti-resonant element in each larger tube,

The aim of this PhD project is to investigate femtosecond pulse propagation in HC-AR fiber filled with noble gas particularly in the mid-IR spectral range. Using gas-filled HC-AR fiber, we have investigated soliton-plasma dynamics and supercontinuum generation in the mid-IR. With this in mind, we have designed, fabricated and demonstrated several low-loss HC-AR fibers which offer broadband light guidance (some of the fibers guide from UV to mid-IR) and effectively single-mode operation. The fibers were fabricated and characterized at CREOL, Microstructured Fibers and Devices Group, University of Central Florida, USA.

Chapter 2 will discuss the nonlinear optical pulse propagation equation such as unidirectional pulse propagation equation (UPPE) and Generalized Schrödinger nonlinear pulse propagation equation (GNLSE). The basic linear and nonlinear effects in fibers are discussed in this chapter.

In **Chapter 3** we will discuss the guiding mechanism and modal properties of 4 different types of HC-AR fiber. We will show that how arrangement of the anti-resonant cladding tubes affect the loss performance and single-mode operation.

Chapter 4 describes the role of the shape and position of the nested tubes of HC-AR fiber in terms of loss performance and single-mode operation.

Chapter 5 introduces a novel HC-AR fiber in which cladding tubes are anisotropic in shape. We will show that anisotropic tube HC-AR fiber has better loss performance and single-mode operation compared to the circular tube HC-AR fiber. We will also discuss the transmission and loss spectrum of some novel HC-AR fibers.

Chapter 6 presents the modal properties of gas-filled HC-AR fiber. Various models to calculate group velocity dispersion (GVD) of gas-

filled HC-AR fiber is discussed. Finally, soliton dynamics and UV light generation is also presented.

In **Chapter 7** we will discuss the optical pulse propagation in gas-filled HC-AR in the high intensity regime. Using gas-filled HC-AR fiber, soliton-plasma dynamics is investigated in the mid-IR.

Finally, a summary of this thesis and final remarks are presented in **Chapter 8.**

References

[1] J. C. Knight, J. Broeng, T. A. Birks, and P. S. J. Russel, "Photonic band gap guidance in optical fibers," *Science*, vol. 282, no. 5393, pp. 1476, 1998.

[2] R. F. Cregan *et al.*, "Single-mode photonic band gap guidance of light in air," *Science*, vol. 285, no. 5433, pp. 1537, 1999.

[3] Y. Y. Wang, N. V Wheeler, F. Couny, P. J. Roberts, and F. Benabid, "Low loss broadband transmission in hypocycloid-core Kagome hollow-core photonic crystal fiber," *Opt. Lett.*, vol. 36, no. 5, pp. 669, 2011.

[4] P. S. J. Russell, P. Hölzer, W. Chang, A. Abdolvand, and J. C. Travers, "Hollow-core photonic crystal fibres for gas-based nonlinear optics," *Nat. Photonics*, vol. 8, no. 4, pp. 278, 2014.

[5] G. Humbert *et al.*, "Hollow core photonic crystal fibers for beam delivery," *Opt. Express*, vol. 12, no. 8, pp. 1477, 2004.

[6] F. Gèrôme, P. Dupriez, J. Clowes, J. C. Knight, and W. J. Wadsworth, "High power tunable femtosecond soliton source using hollow-core photonic bandgap fiber, and its use for frequency doubling," *Opt. Express*, vol. 16, no. 4, pp. 2381, 2008.

[7] F. Gérôme, K. Cook, A. George, W. J. Wadsworth, and J. C. Knight, "Delivery of sub-100 fs pulses through 8 m of hollow-core fiber using soliton compression," *Opt. Express*, vol. 15, no. 12, pp. 7126, 2007.

[8] A. Urich, R. R. J. Maier, F. Yu, J. C. Knight, D. P. Hand, and J. D. Shephard, "Flexible delivery of Er:YAG radiation at 2.94 μm with negative curvature silica glass fibers: a new solution for minimally invasive surgical procedures," *Biomed. Opt. Express*, vol. 4, no. 2, pp. 193, 2013.

[9] F. Poletti *et al.*, "Towards high-capacity fibre-optic communications at the speed of light in vacuum," *Nat. Photonics*, vol. 7, pp. 279, 2013.

[10] H. Bao, K. Nielsen, H. K. Rasmussen, P. U. Jepsen, and O. Bang, "Fabrication and characterization of porous-core honeycomb bandgap THz fibers," *Opt. Express*, vol. 20, no. 28, pp. 29507, 2012.

[11] W. Chang *et al.*, "Influence of ionization on ultrafast gas-based nonlinear fiber optics," *Opt. Express*, vol. 19, no. 21, pp. 21018, 2011.

[12] J. C. Travers, W. Chang, J. Nold, N. Y. Joly, and P. St. J. Russell,

"Ultrafast nonlinear optics in gas-filled hollow-core photonic crystal fibers [Invited]," *J. Opt. Soc. Am. B*, vol. 28, no. 12, pp. A11, 2011.

[13] A. Ermolov, K. F. Mak, M. H. Frosz, J. C. Travers, and P. S. J. Russell, "Supercontinuum generation in the vacuum ultraviolet through dispersive-wave and soliton-plasma interaction in a noble-gas-filled hollow-core photonic crystal fiber," *Phys. Rev. A - At. Mol. Opt. Phys.*, vol. 92, no. 3, pp. 033821, 2015.

[14] M. F. Saleh *et al.*, "Theory of photoionization-induced blueshift of ultrashort solitons in gas-filled hollow-core photonic crystal fibers," *Phys. Rev. Lett.*, vol. 107, no. 20, pp. 203902, 2011.

[15] P. Hölzer *et al.*, "Femtosecond nonlinear fiber optics in the ionization regime," *Phys. Rev. Lett.*, vol. 107, no. 20, pp. 203901, 2011.

[16] F. Benabid and P. J. Roberts, "Linear and nonlinear optical properties of hollow core photonic crystal fiber," *J. Mod. Opt.*, vol. 58, no. 2, pp. 87, 2011.

[17] B. Debord *et al.*, "Hypocycloid-shaped hollow-core photonic crystal fiber Part I: Arc curvature effect on confinement loss," *Opt. Express*, vol. 21, no. 23, pp. 28597, 2013.

[18]P. Roberts *et al.*, "Ultimate low loss of hollow-core photonic crystal fibres," *Opt. Express*, vol. 13, no. 1, pp. 236, 2005.

[19] F. Couny, F. Benabid, P. J. Roberts, P. S. Light, and M. G. Raymer, "Generation and photonic guidance of multi-octave optical-frequency combs," *Science*, vol. 318, no. 5853, pp. 1118, 2007.

[20] F. Poletti, "Nested antiresonant nodeless hollow core fiber," *Opt. Express*, vol. 22, no. 20, pp. 23807, 2014.

[21] M. Michieletto, J. K. Lyngsø, C. Jakobsen, J. Lægsgaard, O. Bang, and T. T. Alkeskjold, "Hollow-core fibers for high power pulse delivery," *Opt. Express*, vol. 24, no. 7, pp. 7103, 2016.

[22] M. S. Habib, O. Bang, and M. Bache, "Low-loss hollow-core silica fibers with adjacent nested anti-resonant tubes," *Opt. Express*, vol. 23, no. 13, pp. 17394, 2015.

[23] M. S. Habib, O. Bang, and M. Bache, "Low-loss single-mode hollow-core fiber with anisotropic anti-resonant elements," *Opt. Express*, vol. 24, no. 8, pp. 8429, 2016.

[24] M. S. Habib, O. Bang, and M. Bache, "Low-loss Hollow-core Anti-Resonant Fibers with Semi-Circular Nested Tubes," *IEEE J. Sel. Top. Quantum Electron.*, vol. 22, no. 2, pp. 4402106, 2016.

[25] F. Couny, F. Benabid, and P. S. Light, "Large-pitch kagome-structured hollow-core photonic crystal fiber," *Opt. Lett.*, vol. 31, no. 24, pp. 3574, 2006.

[26] Y. Y. Wang, F. Couny, P. J. Roberts, and F. Benabid, "Low loss broadband transmission in optimized core-shape Kagome hollow-core PCF," *Lasers Electro-Optics Quantum Electron. Laser Sci. Conf. (QELS), 2010 Conf.*, pp. 4–5, 2010.

[27] Y. Wang *et al.*, "Hollow-core photonic crystal fibre for high power laser beam delivery," *High Power Laser Science and Eng.*, vol. 1, no.1, pp. 17, 2013.

[28] A. D. Pryamikov, A. S. Biriukov, A. F. Kosolapov, V. G. Plotnichenko, S. L. Semjonov, and E. M. Dianov, "Demonstration of a waveguide regime for a silica hollow-core microstructured optical fiber with a negative curvature of the core boundary in the spectral region > 3.5 μm," *Opt. Express*, vol. 19, no. 2, pp. 1441, 2011.

[29] F. Yu, W. J. Wadsworth, and J. C. Knight, "Low loss silica hollow core fibers for 3-4 μm spectral region," *Opt. Express*, vol. 20, no. 10, pp. 11153, 2012.

[30] A. N. Kolyadin, A. F. Kosolapov, A. D. Pryamikov, A. S. Biriukov, V. G. Plotnichenko, and E. M. Dianov, "Light transmission in negative curvature hollow core fiber in extremely high material loss region," *Opt. Express*, vol. 21, no. 8, pp. 9514, 2013.

[31] W. Belardi and J. C. Knight, "Hollow antiresonant fibers with reduced attenuation," *Opt. Lett.*, vol. 39, no. 7, pp. 1853, 2014.

[32] W. Belardi and J. C. Knight, "Hollow antiresonant fibers with low bending loss," *Opt. Express*, vol. 22, no. 8, pp. 9514, 2014.

[33] A. F. Kosolapov *et al.*, "Demonstration of CO_2-laser power delivery through chalcogenide-glass fiber with negative-curvature hollow core," *Opt. Express*, vol. 19, no. 25, pp. 25723, 2011.

Chapter 2

Nonlinear optical pulse propagation in fibers

In this chapter, the basic principles of nonlinear pulse propagation in fiber have been discussed. The pulse propagation is derived from the well-known Maxwell's equation and expressed in this work as a function of real electric field. We will mainly focus on the unidirectional pulse propagation equation (UPPE) [1][2] optical carrier resolved propagation model. In this thesis, the optical pulse propagation in the fiber has been studied using the UPPE. Finally, basic nonlinear effects in fibers are discussed which are based on the nonlinear Schrödinger equation (NLSE).

2.1 Maxwell's wave equation

The propagation of an electromagnetic wave is governed by the Maxwell's equation and can be written as in the point form [3]–[6]

$$\nabla . \mathbf{E} = \frac{\rho}{\epsilon_0} \tag{2.1}$$

$$\nabla . \mathbf{B} = 0 \tag{2.2}$$

$$\nabla \times \mathbf{E} = -\frac{\partial \mathbf{B}}{\partial t} \tag{2.3}$$

$$\nabla \times \mathbf{H} = \mathbf{J} + \frac{\partial \mathbf{D}}{\partial t} \tag{2.4}$$

$$\mathbf{B} = \epsilon_0 \mathbf{H} + \mathbf{M}$$

$$\mathbf{D} = \epsilon_0 \epsilon_r \mathbf{E} + \mathbf{P},$$

where $\mathbf{E}$ and $\mathbf{H}$ indicate electric filed and magnetic field, $\mathbf{D}$ and $\mathbf{B}$ indicate electric and magnetic flux density, $\mathbf{J}$ and ρ indicate current density and charge density, ϵ_0 and μ_0 are the vacuum permittivity and

permeability, ϵ_r is the relative permittivity, $\mathbf{P}$ and $\mathbf{M}$ present electric and magnetic polarization. Symbols in **bold** present vector quantities. The nabla symbol "∇" denotes Laplacian operator, "$\nabla.$"and "$\nabla\times$" denote divergence and curl operator.

In a region, where there is no charge ($\rho = 0$) and no current ($\mathbf{J} = 0$), and in a non-magnetic medium such as in optical fiber $\mathbf{M} = 0$, Maxwell's equations reduce to

$$\nabla.\,\mathbf{E} = 0 \tag{2.5}$$

$$\nabla.\,\mathbf{B} = 0 \tag{2.6}$$

$$\nabla \times \mathbf{E} = -\frac{\partial \mathbf{B}}{\partial t} \tag{2.7}$$

$$\nabla \times \mathbf{H} = \frac{\partial \mathbf{D}}{\partial t} = \frac{\partial(\epsilon_0 \epsilon_r \mathbf{E} + \mathbf{P_{NL}})}{\partial t}, \tag{2.8}$$

To derive the Maxwell's wave equation, we use the following equations

$$\nabla \times \nabla \times \mathbf{E} = \nabla(\nabla.\,\mathbf{E}) - \nabla^2 \mathbf{E}, \tag{2.9}$$

The second term of Eq. (2.9) can be omitted assuming that the longitudinal field component of the fundamental mode is negligibly small. Using the formulas (2.7) and (2.8), Eq. (2.9) can be written as

$$\begin{aligned} \nabla^2 \mathbf{E} = \left(\nabla \times \frac{\partial \mathbf{B}}{\partial t}\right) &= \mu_0 \frac{\partial}{\partial t}(\nabla \times \mathbf{H}) \\ &= \mu_0 \frac{\partial}{\partial t}\left(\epsilon_0 \frac{\partial(\epsilon_r \mathbf{E})}{\partial t} + \frac{\partial \mathbf{P_{NL}}}{\partial t}\right), \end{aligned} \tag{2.10}$$

The Maxwell's wave equation in time domain can be written as

$$\nabla^2 \mathbf{E} - \frac{1}{c^2}\frac{\partial^2}{\partial t^2} \int_{-\infty}^{t} \epsilon_r(t-t')\mathbf{E}dt' = \mu_0 \frac{\partial^2 \mathbf{P_{NL}}}{\partial t^2}\,, \tag{2.11}$$

where $c = \frac{1}{\sqrt{\epsilon_0 \mu_0}}$ is the velocity of light in vacuum.

In frequency domain the Maxwell's wave equation can be written as

$$\nabla^2 \mathbf{E}(\omega) + \frac{\omega^2 n^2(w)}{c^2} = -\mu_0 \omega^2 \mathbf{P_{NL}}(\omega), \tag{2.12}$$

where $n(\omega)$ is the frequency dependent effective mode index which is related to the relative permittivity, ϵ_r by the following relation

$$\epsilon_r(\omega) = \left(n(\omega) + \frac{i\alpha(\omega)c}{2\omega}\right)^2, \tag{2.13}$$

where ω is the angular frequency and α is absorption coefficient.
The induced electric polarization $\mathbf{P}$ can is expressed in terms of linear and nonlinear polarization as [5]

$$\mathbf{P} = \mathbf{P_L} + \mathbf{P_{NL}}, \tag{2.14}$$

where $\mathbf{P_L}$ and $\mathbf{P_{NL}}$ is the linear and nonlinear polarization respectively. The linear polarization is related with the linear susceptibility,$\chi^{(1)}$ with the following relation

$$\mathbf{P_L} = \epsilon_0 \int_{-\infty}^{t} \chi^{(1)}(t-t').\mathbf{E}(r,t'). \tag{2.15}$$

The nonlinear polarization is related to the third order susceptibility, $\chi^{(3)}$ which is expressed as [5]

$$\begin{aligned}\mathbf{P_{NL}} = \epsilon_0 \iiint_{-\infty}^{t} &\chi^{(3)}(t-t_1, t-t_2, t-t_3) \\ &\vdots\ \mathbf{E}(r,t_1)\mathbf{E}(r,t_2)\mathbf{E}(r,t_3)dt_1dt_2dt_3.\end{aligned} \tag{2.16}$$

The third order susceptibility $\chi^{(3)}$ gives rise to the Kerr effect. The Kerr effect is an intensity dependent modification of the refractive index, which leads to phenomena such as self-phase modulation (SPM), cross-phase modulation (XPM) and four-wave mixing (FWM). The intensity dependent refractive index can be expressed as

$$\Delta n = n_2|E|^2; \qquad n_2 = \frac{3\chi^{(3)}}{4c\epsilon_0 n_0^2}, \tag{2.17}$$

where $|E|^2$ is the intensity of the pulse.

2.2 Pulse propagation equation

2.2.1 Unidirectional pulse propagation equation

To derive the UPPE, we assume the pulse propagation in the positive z-direction and disregard any transverse variations in the fields [7]. We consider the electric and nonlinear polarization fields are polarized in the same direction. In scalar from the wave equation can be written as

$$(\partial_z^2 - \frac{n^2(\omega)}{c^2}\partial_t^2)E(z,t) = \mu_0 \partial_t^2 P_{NL}(z,t). \tag{2.18}$$

The electric field propagating in the z-direction is written as

$$E(z,t) = \frac{1}{2\pi}\int_{-\infty}^{\infty} A(z,\omega)e^{i(\beta(\omega)z-\omega t)}d\omega, \tag{2.19}$$

where A is the amplitude of the electric field and $\beta(\omega)$ is the propagation constant. In the above equation the electric field is a real quantity, therefore $E(z,t) = E^*(z,t)$ and $A(z,-\omega)e^{i\beta(-\omega)z} = A^*(z,\omega)e^{-i\beta(\omega)z}$. If we consider only positive frequencies, Eq. (2.19) can be separated two integrals as

$$E(z,t) = \frac{1}{2\pi}\int_{0}^{\infty} A(z,\omega)e^{i(\beta(\omega)z-\omega t)}d\omega + \frac{1}{2\pi}\int_{0}^{\infty} A^* e^{-i(\beta(\omega)z-\omega t)}d\omega, \tag{2.20}$$

Using Eq. (2.18) and Eq. (2.20), we can write

$$\begin{aligned}
&\frac{1}{2\pi}\int_{0}^{\infty}(\frac{\partial^2 A}{\partial z^2} + 2i\beta(\omega)\frac{\partial A}{\partial z} - \beta^2(\omega)A)e^{i(\beta(\omega)z-\omega t)}d\omega \\
&+\frac{1}{2\pi}\int_{0}^{\infty}(\frac{\partial^2 A^*}{\partial z^2} + 2i\beta(\omega)\frac{\partial A^*}{\partial z} - \beta^2(\omega)A^*)e^{-i(\beta(\omega)z-\omega t)}d\omega \\
&-\frac{1}{c^2}\frac{\partial^2}{\partial t^2}\int_{-\infty}^{t} n^2(t-t')E(z,t')dt' \\
&\qquad = -\frac{\mu_0}{2\pi}\int_{-\infty}^{\infty}\omega^2 P_{\mathrm{NL}}(z,\omega)e^{-i\omega t}d\omega,
\end{aligned} \tag{2.21}$$

We know that the convolution of refractive index with the electric field is a real quantity and the right side in Eq. (2.21) is also real, we have $n^2(-\omega) = n^2(\omega)$ and $P_{\mathrm{NL}}(z,-\omega) = P^*_{\mathrm{NL}}(z,\omega)$.
Therefore, Eq. (2.21) can be written as

$$\begin{aligned}\frac{1}{2\pi}\int_0^\infty (\frac{\partial^2 A}{\partial z^2} + 2i\beta(\omega)\frac{\partial A}{\partial z} - \beta^2(\omega)A)e^{i(\beta(\omega)z-\omega t)}d\omega + c.c. \\ = -\frac{\mu_0}{2\pi}\int_0^\infty \omega^2 P_{\mathrm{NL}}(z,\omega)e^{-i\omega t}d\omega + c.c\end{aligned} \tag{2.22}$$

The equality of the above equation is satisfied when the condition is met for positive frequencies.

$$(\frac{\partial^2 A(z,\omega)}{\partial z^2} + 2i\beta(\omega)\frac{\partial A(z,\omega)}{\partial z})e^{i\beta(\omega)z} = -\mu_0\omega^2 P_{\mathrm{NL}}(z,\omega) \tag{2.23}$$

For slow varying approximation $|\partial_z A(z,\omega)| \ll |\beta(\omega)A(z,\omega)|$ and $\partial_z^2 A \ll \partial_z \beta(\omega)A$. The first term in the above equation can be removed and Eq. (2.23) reduces to

$$\frac{\partial A(z,\omega)}{\partial z} = \frac{i}{2\beta(\omega)}\mu_0\omega^2 P_{\mathrm{NL}}(z,\omega)e^{-i\beta(\omega)z} \tag{2.24}$$

Using Eq. (2.22) and Eq. (2.24), the forward UPPE can be written as

$$\frac{\partial E(z,\omega)}{\partial z} = i\beta(\omega)E(z,\omega) + i\frac{\omega^2}{2c^2\epsilon_0\beta(\omega)}P_{\mathrm{NL}}(z,\omega). \tag{2.25}$$

The above UPPE is derived assuming no loss in the fiber. If we include loss, then the above equation can be expressed as

$$\begin{aligned}\frac{\partial E(z,\omega)}{\partial z} = i\beta(\omega)E(z,\omega) - \frac{\alpha(\omega)}{2}E(z,\omega) \\ + i\frac{\omega^2}{2c^2\epsilon_0\beta(\omega)}P_{\mathrm{NL}}(z,\omega),\end{aligned} \tag{2.26}$$

where $\alpha(\omega)$ is the attenuation in m^{-1}. The above equation is equivalent to [1], [8], [9]. The numerical simulations are performed in a co-

moving time frame traveling at the group velocity of the pump pulse so that the propagating pulse always remains in sight [10], [11]. The UPPE has been extensively used to investigate nonlinear effects in gas-filled fibers [10], [12]–[16].

2.2.2 Generalized nonlinear Schrödinger equation

Another well-known and accurate method which is based on the complex envelope is also extensively used to investigate nonlinear effects in fibers known as generalized nonlinear Schrödinger equation (GNLSE). In the retarded time frame $\tau = t - z/v_g$, GNLSE is expressed as [5], [17]–[19]

$$\begin{aligned}\frac{\partial A}{\partial z} - i\sum_{m\geq 2}\frac{i^m\beta_m}{m!}\frac{\partial^m A}{\partial \tau^m} + \frac{\alpha}{2}A \\ = i\gamma\left(1 + i\tau_{shock}\frac{\partial}{\partial \tau}\right) \\ \times\left(A(z,t)\int_{-\infty}^{\infty}R(\tau')|A(z,\tau-\tau')|^2 d\tau'\right).\end{aligned} \tag{2.27}$$

The linear propagation effects are shown in the left-hand side in which α is the attenuation and β_m is the dispersion coefficients related with the Taylor series expansion of the propagation constant $\beta(\omega)$ about the carrier frequency ω_0.

The right-hand side of Eq.(2.27) represents the nonlinear effects where γ is the nonlinear coefficient and $R(T)$ is the Raman response function. The strength of the nonlinearity is described by nonlinear coefficient γ, which is expressed as [5]

$$\gamma = \frac{\omega_0 n_2(\omega_0)}{cA_{\text{eff}}(\omega_0)}, \tag{2.28}$$

where $A_{\text{eff}}$is the effective mode area at the carrier frequency ω_0. However, frequency dependent nonlinear coefficient is defined as [20]

$$\gamma(\omega) = \frac{n_2 n_{\text{eff}}(\omega_0)\omega_0}{n_{\text{eff}}(\omega)c\sqrt{A_{\text{eff}}(\omega)A_{\text{eff}}(\omega_0)}}, \tag{2.29}$$

where n_{eff} is the effective mode index of the core-guided mode. The Raman function $R(T)$ is modeled as [5]

$$\begin{aligned} R(T) &= (1-f_R)\delta(t) + f_R h_R(t) \\ &= (1-f_R)\delta(t) \\ &\quad + f_R \frac{\tau_1^2+\tau_2^2}{\tau_1\tau_2^2} e^{-\left(\frac{t}{\tau_2}\right)} \sin\left(\frac{t}{\tau_1}\right)\Theta(t), \end{aligned} \tag{2.30}$$

where $\Theta(t)$ is the Heaviside step function and $\delta(t)$ is the Dirac delta function. The Raman function consists of two parts: (1) the electronic response, which is assumed instantaneous and hence described by the delta function $\delta(t)$ and (2) the delayed Raman response $h_R(t)$ originating from phonon interactions [19]. In our work, we will be using Raman inactive noble gas, therefore Raman contribution can be neglected from Eq. (2.27) which has been discussed in chapter 6. The derivative term on the right-hand side of Eq. (2.27) models the dispersion of the nonlinearity characterized by a time scale $\tau_{shock} = 1/\omega_0$, which leads to effect i.e., self-steepening [5].

If we only consider group-velocity dispersion (GVD) and instantaneous Kerr nonlinearity, the GNLSE reduces to the standard nonlinear Schrödinger equation (NLSE) expressed as

$$\frac{\partial A}{\partial z} = -i\frac{\beta_2}{2}\frac{\partial^2 A}{\partial \tau^2} + i\gamma A|A|^2. \tag{2.31}$$

The NLSE is the simplest nonlinear equation to study the Kerr effect.

2.3 Group-velocity dispersion

When a light wave interacts with bound electrons of a dielectric (fiber), the medium response in general depends on the optical frequency. This property, referred to as chromatic dispersion, manifests through the frequency dependent nature of the refractive index $n(\omega)$. The origin of

chromatic dispersion is related to the characteristic resonance frequencies at which the medium absorbs the electromagnetic radiation through oscillations of bound electrons. The refractive index is well approximated by the Sellmeier equation [5]

$$n^2(\omega) = 1 + \sum_{j=1}^{m} \left(\frac{B_j \omega_j^2}{\omega_j^2 - \omega^2} \right), \tag{2.32}$$

where ω_j is the resonance frequency and B_j is the strength of jth resonance. For optical fibers, the parameter ω_j and B_j are obtained experimentally by fitting the measured dispersion curves to Eq. (2.32) with $m = 3$ and depend on the core constituents. Mathematically, the effect of fiber dispersion are accounted for by expanding the mode-propagation constant in a Taylor series about the center frequency ω_0:

$$\beta(\omega) = n(\omega)\frac{\omega}{c} + \beta_1(\omega - \omega_0) + \frac{1}{2}\beta_2(\omega - \omega_0)^2 + \cdots \tag{2.33}$$

where $\beta_m = (d^m \beta / d\omega^m)_{\omega - \omega_0}$, the term β_1 is related to group velocity by $v_g = \beta_1^{-1}$, while β_2 is responsible for pulse broadening. Both are related to refractive index n and its derivatives through the relations

$$\beta_1 = \frac{1}{c}\left(n + \omega \frac{dn}{d\omega} \right) = \frac{n_g}{c} = \frac{1}{v_g}, \tag{2.34}$$

$$\beta_2 = \frac{1}{c}\left(2\frac{dn}{d\omega} + \omega \frac{d^2 n}{d\omega^2} \right) \approx \frac{\omega}{c}\left(\frac{d^2 n}{d\omega^2} \right), \tag{2.35}$$

where n_g is the group index. Chromatic dispersion is composed of material dispersion and waveguide dispersion. The dispersion can be expressed by the following first order approximation [8]

$$D(\lambda) = \frac{d\beta_1}{d\lambda} = -\frac{2\pi c \beta_2}{\lambda^2} \approx -\frac{\lambda}{c}\left(\frac{d^2 n_{eff}}{d\lambda^2} \right) \tag{2.36}$$

where n_{eff} is the effective refractive index of the fundamental mode, λ is the wavelength, and c is the velocity of light in vacuum. If $\beta_2 < 0$,

the GVD is said to be anomalous, GVD is said to be normal if $\beta_2 > 0$. The sign of β_2 plays important role on the pulse propagation in fiber.

2.4 Propagation regimes in fibers

Depending on the fiber parameters and pulse parameters, the pulse propagation in fiber can be either linear, nonlinear, or both. Therefore, it is necessary to define two characteristic length scales in order to get an idea which effect has dominant contribution in the pulse propagation.

The dispersion length L_D is the length over which the dispersive effects become important. The dispersion length can be defined as [5]

$$L_D = \frac{T_0^2}{|\beta_2|}, \tag{2.37}$$

where T_0 is the pulse duration. For a Gaussian pulse $T_0 = \frac{T_{FWHM}}{2ln\sqrt{2}}$.

The nonlinear length L_{NL} is defined as [5]

$$L_{NL} = \frac{1}{\gamma P_0}, \tag{2.38}$$

where P_0 is the peak power of the input pulse. The dispersion length L_D and nonlinear length L_{NL} defines different propagation regimes. For given length of fiber L, if $L_D \gg L$ and $L_{NL} \gg L$, the dispersion and nonlinear effects will not affect the propagating pulse. The pulse will propagate without changing its shape. If $L_D < L$ and $L_{NL} \gg L$, the pulse will be dominated by dispersive effects and nonlinearity will not affect during the propagation and vice-versa. If$L_D \ll L$ and $L_{NL} \ll L$, the pulse will be dominated by both dispersive and nonlinear effects. The soliton will only form in the anomalous dispersion regime, when dispersion effect is equal to the nonlinear effect.

2.4.1 Linear propagation regime

The linear propagation regime dominates when $L_D \ll L_{NL}$. In this case nonlinear effects can be neglected and Eq. (2.31) can be written as

$$\frac{\partial A}{\partial z} = -i\frac{\beta_2}{2}\frac{\partial^2 A}{\partial \tau^2}, \tag{2.39}$$

If $\tilde{A}(z,\omega)$ is the Fourier-transform of $A(z,\tau)$ such that

$$A(z,\tau) = \frac{1}{2\pi}\int_{-\infty}^{\infty}\tilde{A}(z,\omega)e^{-i\omega\tau}d\omega, \tag{2.40}$$

The solution of Eq. (2.39) in the frequency domain becomes

$$\tilde{A}(z,\omega) = \tilde{A}(0,\omega)e^{(\frac{i}{2}\beta_2\omega^2 z)}. \tag{2.41}$$

It can be seen from Eq. (2.41) that in the spectral domain GVD changes the phase of each spectral component of the pulse that depends on both the frequency and propagation distance.

In the time domain, the solution of Eq. (2.41) for Gaussian input pulse can be expressed as [5]

$$A(z,\tau) = \frac{T_0}{(T_0^2 - i\beta_2 z)^{\frac{1}{2}}}\mathrm{e}^{\left[-\frac{T^2}{2(T_0^2 - i\beta_2 z)}\right]}. \tag{2.42}$$

It can be seen from Eq. (2.42) that in the time domain, a Gaussian pulse maintains its shape during the propagation in fibers However, the pulse duration changes according to the following equation [5]

$$\tau(z) = T_0\sqrt{1 + \left(\frac{z}{L_D}\right)^2}. \tag{2.43}$$

2.4.2 Nonlinear propagation regime

When $L_{NL} \ll L_D$, the dispersion effect can be neglected so that Eq. (2.31) reduces to

$$\frac{\partial A}{\partial z} = i\gamma|A|^2 A, \tag{2.44}$$

The general solution of the above equation is

$$A(z,\tau) = A(0,\tau)e^{i\gamma|A(0,\tau)|^2 z};\ \phi_{NL}(z,\tau) = \gamma|A(0,\tau)|^2 z. \tag{2.45}$$

It is clear from Eq. (2.45) that temporal shape of the pulse remains same ($|A(z,\tau)|^2 = |A(0,\tau)|^2$). However, the pulse acquirers a phase shift $\phi_{NL}(z,\tau)$ during the propagation which depends on the initial pulse shape and chirp resulting in changes in the pulse spectrum. The phenomenon is called self-phase modulation (SPM). Due to the SPM effect new frequency components are generated which broaden the pulse spectrum. For an un-chirped Gaussian pulse, the leading edge of the pulse will be downshifted in frequency and the trailing edge up-shifted, respectively, which spectrally broadens the pulse [21].

Due to the intensity dependence of group-velocity self-steepening occurs because the pulse peak moves at a lower speed than the wings of the pulse. The shape of the pulse is altered in such a way that the trailing edge of the pulse becomes steeper and the leading edge flatter. The combined effect of SPM and self-steepening results in an asymmetric spectral broadening; for ultrashort pulses it shifts the pulse peak to the trailing edge with propagation, which ultimately creates an optical shock [5].

The Kerr effect also indicates that the refractive index can be modulated by the intensity of a co-propagating wave through cross-phase modulation (XPM). The nonlinear phase shift experienced by a field A_1 in the presence of a co-propagating field A_2 at a different frequency can be approximated by

$$\phi_{NL}(z,\tau) \approx \gamma(|A_1(0,\tau)|^2 + 2|A_2(0,\tau)|^2)z. \tag{2.46}$$

The first term in the right-hand side is due to SPM and the second term is from XPM, which is seen to be twice as effective as SPM effect.

2.5 Soliton

The soliton is a pulse that retains its shape during the propagation. The existence of soliton is perfect balance between GVD and SPM. In the anomalous dispersion regime, the chirp from the SPM can be exactly compensated by dispersion effect. The solitons are exact solutions to the NLSE of the form [5]

$$A(z,\tau) = \sqrt{P_0}\,\mathrm{sech}\left(\frac{\tau}{\tau_0}\right) e^{-i|\beta_2|z/2\tau^2}, \tag{2.47}$$

where P_0 is the peak power. The soliton number N is the contribution of dispersion length and nonlinearity length given by

$$N^2 = \frac{L_D}{L_{NL}} = \frac{\gamma P_0 T_0^2}{|\beta_2|}. \tag{2.48}$$

The soliton order $N = 1$ refers to fundamental soliton which propagates without any change in temporal and spectral shape. If $N > 1$, the soliton is referred to as a higher-order soliton. In case of a higher-order soliton, the soliton evolves periodically during the propagation which is shown in Fig. 2.1. Unlike the fundamental soliton, higher-order solitons do not propagate without changing their shape. However, under idealized conditions, solitons change shape in a periodic manner and recover their initial shape after one soliton period. The oscillation period is expressed as [5]

$$z_{sol} = \frac{\pi}{2} L_D. \tag{2.49}$$

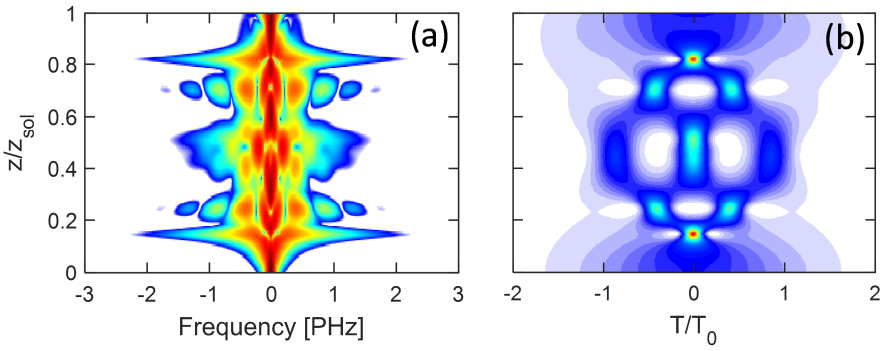

Figure 2.1. (a) Spectral and (b) temporal evolution of $N \approx 4$ soliton with $\beta_2 \approx -10$ fs^2/cm at 1 μm pump wavelength and $T_{FWHM} = 30$ fs Gaussian pulse.

2.6 Conclusion

In this chapter, a unidirectional pulse propagation equation (UPPE), optical carrier resolved model for pulse propagation in fibers is discussed. We derive the UPPE starting from scalar nonlinear wave equation with minimal approximation [9], with proper interpretations of the nonlinear induced polarizations.

We also discuss the basics of pulse propagation in fibers. The dispersion and nonlinearity plays important role on the pulse propagation. When dispersion is dominant over nonlinearity, dispersion only affects the temporal pulse profile while pulse spectrum remains same. When the nonlinearity is acting alone, new frequencies are generated due to the SPM effect. The combined action of dispersion, SPM, and other nonlinear effects on the pulse propagation is discussed in chapter 7.

References

[1] M. Kolesik, J. V. Moloney, and M. Mlejnek, "Unidirectional optical pulse propagation equation," *Phys. Rev. Lett.*, vol. 89, no. 28, pp. 283902, 2002.

[2] M. Kolesik and J. V. Moloney, "Nonlinear optical pulse propagation simulation: From Maxwell's to unidirectional equations," *Phys. Rev. E - Stat. Nonlinear, Soft Matter Phys.*, vol. 70, pp. 0336604, 2004.

[3] J. D. Jackson, "Classical Electrodynamics," *Wiley, 1998*.

[4] R. Boyd, "Nonlinear Optics," Elsevier Science, 2008.

[5] G. Agrawal, "Nonlinear Fiber Optics," Academic Press, 3rd edition, 2006.

[6] A. Yariv and P. Yeh, "Photonics: Optical Electronics in Modern Communications," Oxford University Press, 2007.

[7] M. Kolesik, P. Townsend, and J. V. Moloney, "Theory and simulation of ultrafast intense pulse propagation in extended media," *IEEE J. Sel. Top. Quantum Electron.*, vol. 18, no. 1, pp. 494, 2012.

[8] A. V Husakou and J. Herrmann, "Supercontinuum generation of higher-order solitons by fission in photonic crystal fibers," *Phys. Rev. Lett.*, vol. 87, no. 20, pp. 203901, 2001.

[9] P. Kinsler, "Optical pulse propagation with minimal approximations," *Phys. Rev. A - At. Mol. Opt. Phys.*, vol. 81, pp. 013819, 2010.

[10] P. Hölzer, "Nonlinear Fiber Optics in Gases and Dilute Plasmas," *PhD Thesis*, 2013.

[11] J. P. Mollenauer, L. F. & Gordon, "Solitons in Optical Fibers: Fundamentals and Applications," *1st edition, Academic Press. 2006,*

[12] W. Chang *et al.*, "Influence of ionization on ultrafast gas-based nonlinear fiber optics," *Opt. Express*, vol. 19, no. 21, pp. 21018, 2011.

[13] W. Chang, P. Hölzer, J. C. Travers, and P. S. J. Russell, "Combined soliton pulse compression and plasma-related frequency upconversion in gas-filled photonic crystal fiber," *Opt. Lett.*, vol. 38, no. 16, pp. 2984, 2013.

[14] D. Novoa, M. Cassataro, J. C. Travers, and P. S. J. Russell, "Photoionization-Induced Emission of Tunable Few-Cycle Midinfrared Dispersive Waves in Gas-Filled Hollow-Core Photonic Crystal Fibers,"

Phys. Rev. Lett., vol. 115, no. 3, pp. 33901, 2015.

[15] K. F. Mak, "Nonlinear optical effects in gas-filled hollow-core photonic-crystal fibers," *PhD Thesis*, 2014.

[16] M. F. Saleh and F. Biancalana, "Tunable frequency-up / down conversion in gas-filled hollow-core photonic crystal fibers," *Opt. Lett.*, vol. 40, no. 18, pp. 4218, 2015.

[17] J. M. Dudley, G. Genty, and S. Coen, "Supercontinuum generation in photonic crystal fiber," *Rev. Mod. Phys.*, vol. 78, no. 4, pp. 1135, 2006.

[18] S. T. Sørensen, "Deep-blue supersontinuum light sources based on tapered photonic crystal fibres," PhD Thesis, 2013.

[19] K. J. Blow and D. Wood, "Theoretical description of transient stimulated Raman scattering in optical fibers," *IEEE J. Quantum Electron.*, vol. 25, no. 12, pp. 2665, 1989.

[20] J. Laegsgaard, "Mode profile dispersion in the generalised nonlinear Schrödinger equation," *Opt. Express*, vol. 15, no. 24, pp. 16110, 2007.

[21] R. H. Stolen and C. Lin, "Self-phase-modulation in silica optical fibers," *Phys. Rev. A*, vol. 17, no. 4, pp. 1448, 1978.

Chapter 3

Hollow-core anti-resonant fibers

In this chapter, we will discuss the guiding mechanism and modal properties of several hollow-core anti-resonant (HC-AR) fibers. Our numerical analysis predicts that these HC-AR fibers show low transmission (propagation) loss, bending loss, broad transmission window, and also offer effectively single-mode operation both in the mid-IR and near-IR spectral regime.

3.1 Guiding mechanism of HC-AR fiber

The guiding mechanism of an HC-AR fiber is based on the combination of inhibited coupling to low density states of cladding modes and anti-resonance as recently proposed by Poletti [1]. As a simple tool, an anti-resonant optical waveguide (ARROW) model can be used to explain the guiding mechanism of HC-AR fiber. The ARROW model was first proposed in 1986 and it is widely used as a simple tool to explain hollow-core photonic band gap (HC-PBG) and other hollow-core fibers [2].

In an ARROW model, the cladding consists of high index layers around the core region, which can be considered as a Fabry-Perot resonator. It can be seen from Fig. 3.1(a) that light is reflected back from the high index layers and strongly confined in the core region at anti-resonant wavelength. Light is guided in the cladding when the wavelength of light in the core matches a resonant wavelength of the Fabry-

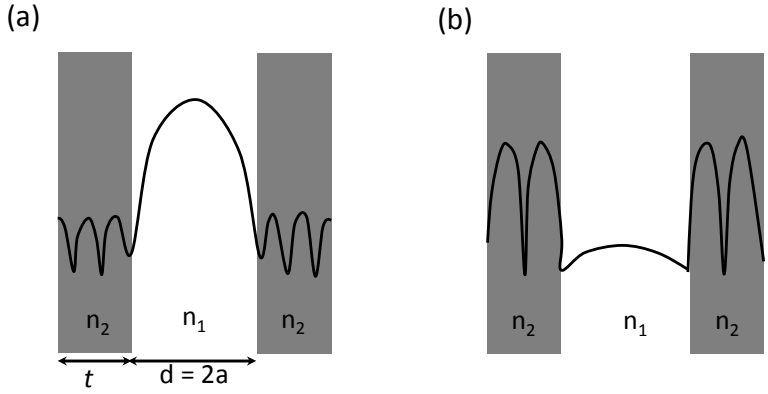

Figure 3.1 Intensity profile of an optical field in the core region and first high index regions. (a) Light is confined in the core at anti-resonant wavelength and (b) light is guided in the Fabry-Perot cavity at the resonant wavelength. Redrawn after [4].

Perot cavity as shown in Fig. 3.1(b). The position of the resonance wavelength assuming $\lambda/a \ll 1$ can be expressed as [3]

$$\lambda_m = \frac{2n_1 t}{m}\sqrt{\left(\frac{n_2}{n_1}\right)^2 - 1}, \qquad m = 1,2,... \tag{3.1}$$

where a is the core radius, t is the thickness the high index layer, n_1 is the refractive index of the core, n_2 is the refractive index of the high index layer (cladding), and m is the order of resonance. Assuming all high index layers are identical and they are in resonance with each other, then the light will leak perpendicular to the core [3].

The condition for anti-resonant reflection is given by [3]

$$\lambda_a = \frac{4n_1 t}{2l+1}\sqrt{\left(\frac{n_2}{n_1}\right)^2 - 1}, \qquad l = 0,1,2,... \tag{3.2}$$

The same principle can be used to explain the guidance in HC-AR fibers [1]. The guiding mechanism of HC-AR fiber is given by anti-resonant elements present in the core-wall or in the cladding structure.

If the light launched in the fiber is in anti-resonance with the glass structures/tubes which act as resonators, the light will be *trapped* in the core and cannot leak to the cladding. The overlap integral between the cladding modes and the core mode can be strongly reduced by carefully engineering the interaction between the cladding modes and the core mode [5]–[7]. The absolute amount of loss of the core modes will then depend on inhibited coupling between the core and cladding modes due to a low density of cladding modes[8]–[11], which is a property that can be controlled by suitable fiber design engineering which will discussed in this Chapter and Chapter 5 and Chapter 6.

When the light in the fiber is in-resonance with cladding elements, the light cannot be confined in the core and it can propagate inside the glass structure via cladding modes meaning that there is a strong coupling between the core modes and cladding modes showing high loss.

3.2 HC-AR fibers in the mid-IR

In this section, we thoroughly investigate the modal properties of 4 different types of HC-AR fibers. We will discuss and compare the transmission loss and bend loss performance and show effectively single-mode operation of these HC-AR fibers.

3.2.1 Geometry of mid-IR HC-AR fiber

The geometry of negative curvature HC-AR fibers considered in simulations is shown in Fig. 3.2. The term 'negative curvature' can be defined as the surface normal to the core boundary is oppositely directed with a radial unit vector in a cylindrical coordinate system [12]. We used a core diameter of $D_c = 94$ μm (defined as the maximum diameter of a circle that can be inscribed inside the core) in our all simulations, which is identical to the fiber structure reported experimentally

in [2] and simulated in [13]. We choose silica strut (wall) thickness of $t = 1.26$ μm so that an anti-resonant first-order transmission window in the high-frequency mid-IR range (specifically around $\lambda = 2.94$ μm, the emission wavelength of Er:YAG lasers). This is because we found a superior loss-performance by choosing operation in the first transmission window instead of the second. For the same reason we choose also throughout this chapter to use six anti-resonant tubes instead of eight in all designs. Figure 3.2 shows the four considered designs, all optimized to give minimal leakage loss at $\lambda = 2.94$ μm. Figure 3.2(a) shows the geometry of a "typical" HC-AR fiber [14] with six anti-resonant tubes in a node-free configuration. The modified HC-AR fibers, originally investigated in an 8-ring configuration by Belardi *et al.* [13] and later in a 6-ring configuration by Poletti [1], are shown in Figs. 3.2(b)-3.2(c), using the nested (b) and nested-in-nested (c) configurations. Our proposed alternative adjacent nested anti-resonant (ANAR) design is shown in Fig. 3.2(d), using node-free outer cladding tubes and multiple adjacent nested elements. In our ANAR design the six outer capillary tubes have diameter d_0 and a perimeter distance between them of 4 μm, i.e. as in design (a). The nested elements are chosen as three adjacent tubes with inner air-hole diameter of d_i. The first nested tube is placed in the radial direction at the internal edge of the outer tube, while the two other nested tubes are placed along the direction of a line passing through the outer tube center and orthogonally to the radial direction. In this configuration optimized to give lowest leakage losses the angle between the center and the adjacent nested tubes is therefore 90°, but we will also investigate configurations where this angle is changed. The inner air-hole diameter d_i and cladding air-hole diameter d_o in the optimized design is 32 μm and 86 μm, respectively. The perimeter separation between the inner air-holes is 2.35 μm. The inner and outer air-hole tubes are arranged in a node-free design, as the presence of nodes generates large oscillations with spectral periods of a

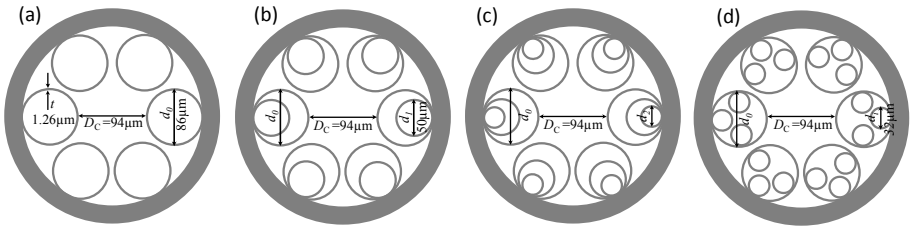

Figure 3.2. Geometries considered in the mid-IR simulations. (a) Typical optimized HC-AR fiber design with six circular tubes; (b)-(c) the nested ("1AE", i.e. one anti-resonant element) and nested-in-nested ("2AE", i.e. two anti-resonant elements) designs proposed in [1] in which $d_1 = 25$ μm and $d_2 = d_1/2$; (d) our proposed adjacent nested anti-resonant (ANAR) structure with three adjacent nested anti-resonant tubes. All fibers have the same core diameter $D_c = 94$ μm and uniform silica strut thickness $t = 1.26$ μm.

few nanometers [1]. Moreover, the node-free design is known to reduce the leakage loss [1].

We used the finite-element method based commercial software COMSOL for our numerical simulations. Perfectly-matched layer boundary conditions were used to accurately calculate the leakage loss. In order to model HC-AR fibers accurately, great care must be taken to optimize both mesh size and perfectly- matched layer parameters [1]. To ensure convergence of the numerical results, the code was tested by reproducing the results of [1], [13], [15], and therefore we are able to here present our own calculations of the designs proposed in the literature and shown in Figs. 3.2(a)-3.2(c).

3.2.2 Transmission loss in the mid-IR

Figure 3.3 shows the loss spectrum of the four considered structures. In our calculations, the fraction of power in silica was calculated to estimate the effective material loss and then added to the leakage loss to obtain the total transmission loss. The material loss of silica was taken from [9]. The broken black line shows the calculated leakage loss of a

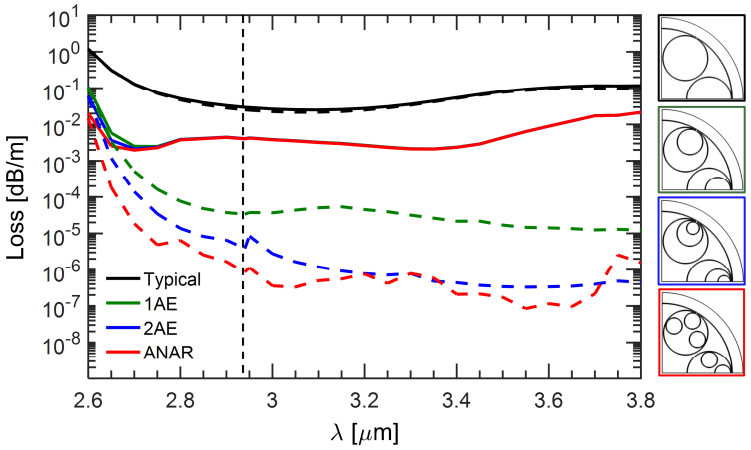

Figure 3.3. Calculated loss spectra. The broken lines indicate leakage loss while solid lines show the transmission loss where the material loss of silica is included. All structures have the same core diameter $D_c = 94$ μm and uniform silica strut thickness t=1.26 μm. The color of the frame corresponds to the color of the line in the plot. The thin dotted line indicates the wavelength for which the losses are optimized.

"typical" optimized HC-AR fiber in which the min mum leakage loss is ~21 dB/km, which is limited by coupling to the voids in the cladding [13]. The broken green and blue lines show the leakage loss of the modified forms proposed in [13] and shown in Figs. 3.2(b)-3.2(c), in which nested anti-resonant elements were used to reduce the leakage loss. The minimum leakage losses are ~0.03dB/km and ~0.0039dB/km at 2.94 μm for 1AE and 2AE, respetively. Finally, the broken red line shows the loss spectrum of our proposed ANAR fiber, in which the minimum leakage loss is about 0.0009 dB/km. Thus, the nested designs have losses several orders of magnitude lower than the "typical" HC-AR fiber and with the ANAR design giving the best performance having the lowest loss in the range 2.75-3.2 μm.

That being said, the loss is clearly dominated by material loss, despite the low power fraction in silica, making the transmission loss practically identical for the 3 different nested designs.

3.2.3 Bending losses in the mid-IR

In order to calculate the bending loss, the bent structure is transformed into its equivalent straight structure with equivalent refractive index profile, n_{eq} defined by [16]

$$n_{eq} = n(x, y)\exp(x/R_b) \tag{3.3}$$

where R_b is the bending radius, x is the transverse distance from the center of the fiber, $n(x, y)$ is the refractive index profile of the straight fiber. The bending losses were calculated at 2.94 μm and the bending direction was chosen along the x-axis giving the bend-loss curve shown in Fig. 3.4. A significant improvement of the bending loss was found for the proposed ANAR fiber (dashed red curve), for which the bending leakage loss is several orders of magnitude lower than the typical HC-AR fiber and even one order of magnitude lower than the 1AE and 2AE fibers for bend radii between 5 and 15 cm and the leakage loss is only weakly changing for bend radii above ~15 cm. Again, as with the transmission loss above, the performance is dominated by material loss, making the bending loss curves of all three nested designs identical for larger bend radii when the material loss is included (solid lines). However, for low bending radius the “typical”, 1AE, and 2AE structures have high loss peaks, whereas no loss peaks are observed for the ANAR structure, which results in very limited increase in transmission loss when the fiber is bent.

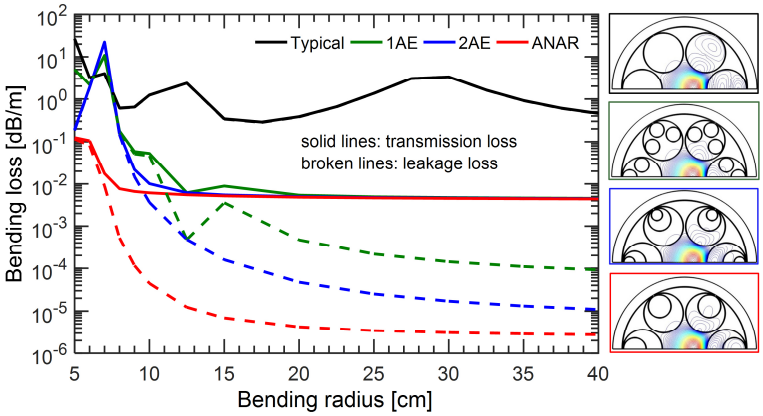

Figure 3.4. Calculated bending loss at 2.94 μm versus bending radius. Note that black solid and broken lines are coincident. The contour plots of the fundamental air-core mode distribution are shown in the right hand side for a 10 cm bending radius. The color of the frame corresponds to the color of the line in the plot.

3.2.4 Effectively single-modeness in the mid-IR

HC-AR fibers are typically not single-moded due to the large core, but may be designed to have higher losses of the higher-order modes (HOMs) so that the fiber is effectively single-moded. Figure 3.5 shows how free design parameters of the ANAR fiber can be controlled to optimize the so-called higher-order-mode extinction ratio (HOMER), which is defined as the ratio between the transmission loss of the HOM having the lowest transmission loss and the transmission loss of the fundamental mode (FM). The optimization of HOMER is performed by symmetrically changing the angle Φ between the adjacent nested tubes and the central nested tube, which is kept fixed, and the inner air-hole diameter d_i. As Fig. 3.5 shows the optimum HOMER is found to be around 100 at Φ=109 degrees and $d_i = 18.4$ μm.

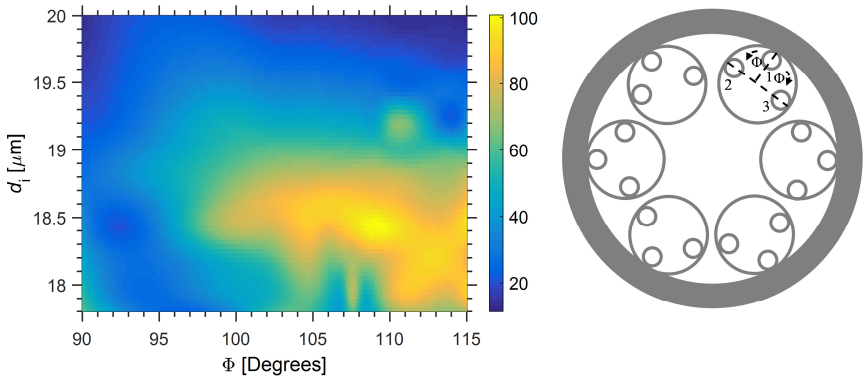

Figure 3.5. Calculated HOMER of the proposed ANAR with different values of d_i as a function of Φ, which is the angle between adjacent inner tubes 2 and 3 and tube 1, while keeping the position of tube 1 fixed as before. The simulations are performed at $\lambda = 2.94$ μm.

In order to better understand how the fiber design affects the HOMER, Fig. 3.6 shows the refractive index, leakage loss, and transmission loss of the first five core-guided modes (LP_{01}, LP_{11}, LP_{21}, LP_{02}, and LP_{31}) as a function of the inner air-hole diameter d_i from 16 to 24 µm with a fixed $D_c = 94$ μm, $t = 1.26$ μm, $d_0 = 86$ μm, and $\Phi = \pi/2$. It can be seen that the effective refractive indices of the core modes do not change much as a function of the inner air-hole diameter. This is obvious, as they depend mainly on the fiber core radius, which is kept constant. Instead, the leakage loss of the LP_{01} mode can clearly be reduced significantly by increasing the inner air-hole diameter. Comparing the figures with the leakage and transmission loss we see that the HOMs have so high leakage loss that it dominates the transmission loss, while for the FM is it the other way around. What is interesting is that while a large inner air-hole diameter d_i gives the lowest leakage loss, it does not give the largest HOMER value. For the ANAR structure a HOMER just above 5 is found for large air-hole diameters above 22 µm.

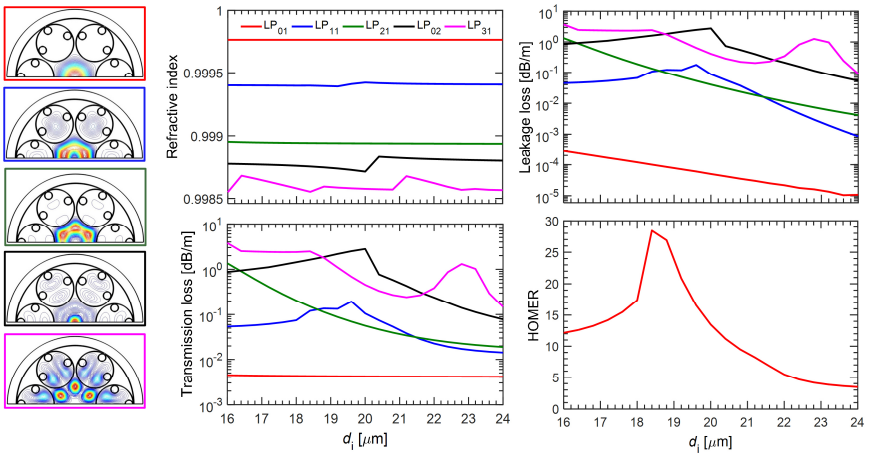

Figure 3.6. Effect of changing the inner air-hole diameter d_i with a fixed $D_c = 47\ \mu$m, $t = 1.26\ \mu$m, $d_0 = 86\ \mu$m, $\Phi = \pi/2$ and wavelength $2.94\ \mu$m . Contour plots of the first five core modes are shown on the left hand side for $18.4\ \mu$m inner air-hole diameter (where the maximum HOMER value is found). The color of the frame corresponds to the color of the line in the plot.

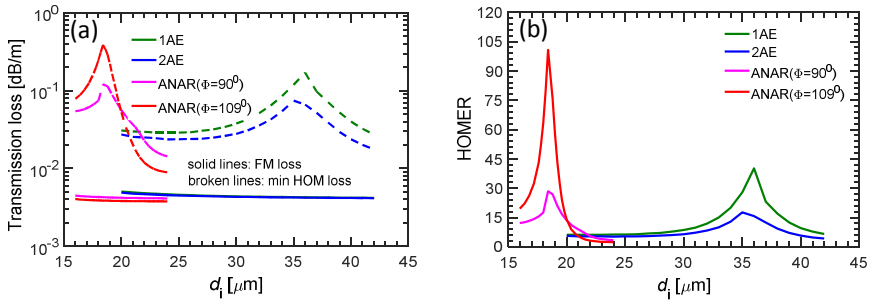

Figure 3.7. Calculated (a) transmission loss and (b) HOMER as a function of d_i for 1AE, 2AE and ANAR structures. The simulations are performed at $\lambda = 2.94\ \mu$m.

However, when decreasing the inner air-hole diameter away from the optimal point of lowest leakage loss the HOMER value increases many-fold. This is because the leakage losses of the HOMs increase faster

than that of the FM. In other words, by sacrificing a low leakage loss one can get a higher HOMER.

Figure 3.7 shows the transmission loss and HOMER as a function of inner air-hole diameter d_i at 2.94 μm for 1AE, 2AE and ANAR structures. In this case the $d_i = d_1$ in the 1AE and 2AE structures, and for the 2AE structure the ratio d_2=d_1/2 was kept fixed. It can be seen from Fig. 3.7(a) that for all considered structures the FM loss is roughly constant whereas the HOM loss changes significantly with d_i. Therefore, HOMER strongly depends on d_i which is shown in Fig. 3.7(b), and the added degree of freedom in the ANAR design in varying the angle turns out to be decisive for obtaining a HOMER level higher than the 1AE and 2AE designs. We note that a similar possibility is offered for the 2AE design, however, we checked that by allowing the diameters of the nested tubes to vary independently, one could not increase HOMER much beyond the level shown in Fig. 3.7, for which $d_2 = d_1/2$ was kept fixed.

Figure 3.8 shows the wavelength dependence of the refractive index, leakage loss, transmission loss and HOMER for the ANAR design optimized for maximum HOMER at 2.94 μm. It shows that HOMER can be made in excess of 50 in the entire spectral regime 2.7-3.1 μm. The highest HOMER of about 330 is obtained at 2.7 μm, close to the resonant regime where the transmission losses are very high. Therefore having such a high HOMER implies an increased transmission loss, so again there is a compromise between loss and HOMER.

Figure 3.9 shows the wavelength dependence of the transmission loss of the FM and the HOMER for all considered structures; each of them has been optimized to give the highest HOMER value at 2.94 μm. It can be seen from Fig. 3.9(b) that the ANAR design has higher HOMER compared to the typical, 1AE and 2AE structures in the spectral range 2.7-3.1 μm.

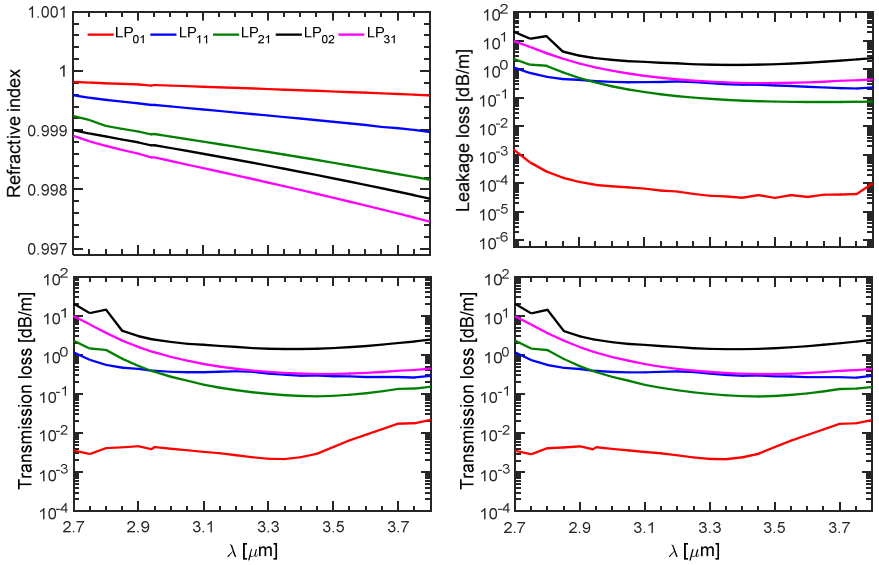

Figure 3.8. Wavelength dependence of refractive index, leakage loss, transmission loss and HOMER with a fixed $D_c = 94\ \mu\text{m}, t = 1.26\ \mu\text{m}, d_0 = 86\ \mu\text{m}$, and Φ=109 degrees for a 18.4 μm inner air-hole diameter. HOMER was calculated with losses in silica taken into account, i.e. using the transmission loss curves.

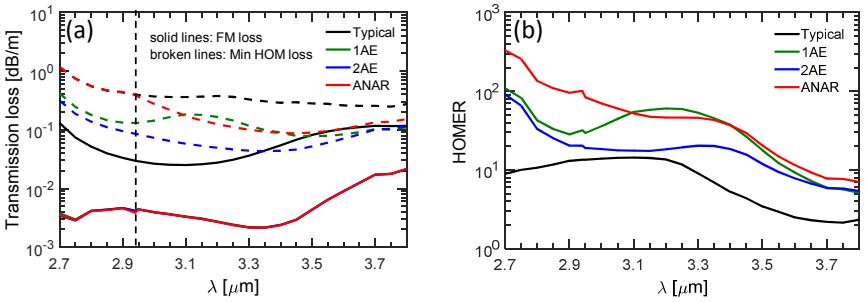

Figure 3.9. Comparing the wavelength dependence of (a) transmission loss of the FM and (b) HOMER for all the considered structures. The ANAR parameters are the same as Fig. 3.8.

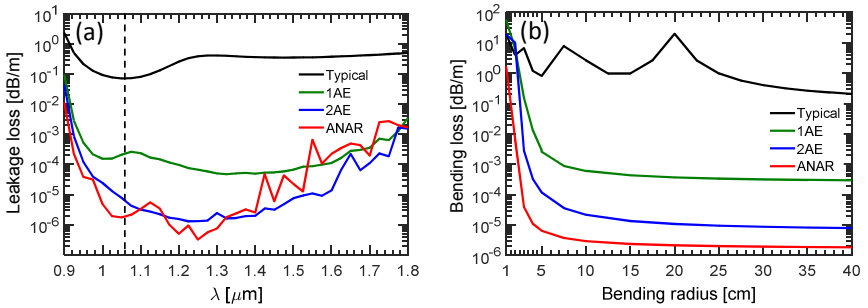

Figure 3.10. Calculated leakage loss spectra (a) and bending loss (b) as a function of bending radius at $\lambda = 1.06$ μm. The fiber parameters have been scaled down by a factor of 3 ($t' = t/3, R_c' = R_c/3, d_0' = d_0/3, and\ d_i' = d_i/3$) and in the ANAR design $\Phi = \pi/2$ was used.

3.3 Performance analysis in the near-IR

In the mid-IR the transmission loss performance was dominated by material loss. We now turn our attention to the near-IR, where material loss can be neglected. As a representative example, we choose to explore the ANAR performance at $\lambda = 1.06$ μm, and to do so we start out by simply scaling down the fiber structural parameters by a factor of 3 in all four designs presented in Fig. 3.2. These scaled-down fibers turn out to give the lowest leakage loss at 1.06 μm, and can therefore not be optimized further. The measured loss of dry F300 silica is of the order of 10^{-3} dB/m [17] or less in the wavelength range between 0.95 and 1.40 μm. The calculated power fraction in silica of the optimum ANAR structure with the lowest leakage loss is less than 10^{-4} in this spectral regime, and similar values are found for the 1AE and 2AE structures. Therefore, the transmission loss will practically be equivalent to the leakage loss.

From the leakage loss spectrum shown in Fig. 3.10(a) we see that the ANAR fiber has a leakage loss of 0.0015 dB/km at 1.06 μm, which is significantly lower than 1AE and roughly a factor of 2 lower than 2AE. It is remarkable to see that the lowest leakage loss is not found at

$\lambda = 1.06$ μm, where the design is optimized for, but at a longer wavelength for all nested designs. This shows that the predicted minimum only holds for the simple "typical" design and that for the nested designs perhaps a smaller strut thickness could be considered as to move this minimum towards the chosen target wavelength.

The bending loss for the scaled fiber structures at 1.06 µm is presented in Fig. 3.10(b), which shows that the bending losses of the three fibers with nested elements are almost constant for reasonable bend radii. Figure 3.10(b) also confirms that the ANAR design has a bend loss below 0.006 dB/km at 5 cm bending radius, which is about one and two orders of magnitude lower than that of the 1AE and 2AE fibers, respectively. Most importantly, the ANAR design shows low bending loss even at a very small bending radius of 1 cm compared to the 1AE and 2AE fibers, at a level which is even comparable to an HC-PBG fiber.

We have also optimized HOMER in the near-IR in the 2D design parameter space of the ANAR fiber, and Fig. 3.11(a) shows again that both Φ and d_i have a strong effect on HOMER. The optimum HOMER is found to be in excess of 2500 at Φ=109 degrees and $d_i = 6.0$ μm. Interestingly, we note that the *optimum angle Φ is the same in both near and mid-IR*. The effect of the inner air-hole diameter d_i on HOMER at 1.06 μm for the considered structures is shown in Fig. 3.11(b). All three structures show that an optimized design can lead to well over 30 dB extinction ratio, and the largest HOMER is found in the ANAR design with Φ=109 degrees. It is important to remember that this optimization comes at the price of an increased leakage loss, as illustrated in Fig. 3.11(c), where we compare the ANAR design with

maximum HOMER (Φ=109^0, $d_i = 6.0$ μm) with the Φ=90^0 design with lowest leakage loss ($d_i = 10.67$ μm) and a third design for which HOMER=100 (Φ=90^0, $d_i = 7.4$ μm). It can be seen from Fig. 3.11(c) that the optimum HOMER design has the highest leakage loss. The

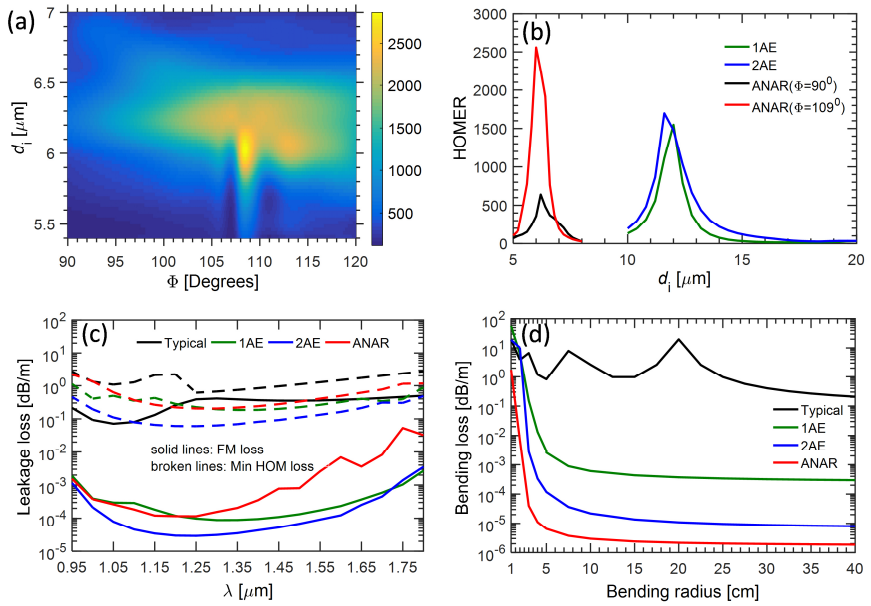

Figure 3.11. Calculated HOMER of the proposed ANAR structure versus diameter d_i and angle Φ (a). HOMER versus d_i, for the 1AE and 2AE structures and the ANAR design with $\Phi = 90^o$ and optimum $\Phi = 109^o$. Leakage loss (c) and bending loss (d) for the ANAR design optimized for maximum HOMER, a design chosen to give an intermediate HOMER, and a design optimized to give the lowest leakage loss. The simulations of (a), (b), and (d) are performed at $\lambda = 1.06$ μm.

bending loss as a function of bending radius is shown in Fig. 3.11(d). Figure 3.11(d) shows that optimum HOMER corresponds to higher bending loss.

Figure 3.12 shows the spectral dependence of the leakage loss of the FM, the minimum HOM loss, and the HOMER in the near-IR. Notably, HOMER is higher than 1000 in the range of $0.96 - 1.2$ μm and more than 1550 in the range 1.0-1.1 μm for an inner air-hole diameter of 6 μm, which makes the fiber effectively single-moded in the near-IR spectral regime. Also the 1AE and 2AE designs have excellent HOMER performances, and especially the 2AE has the highest HOMER and

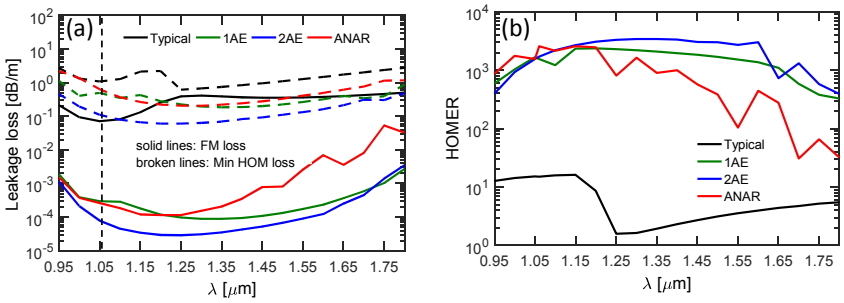

Figure 3.12. Wavelength dependence of (a) leakage loss and (b) HOMER for the optimized parameters. The optimum design parameters are: $t' = t/3, R_c' = R_c/3, d_0' = d_0/3$, and $d_i =$ 6 μm, 12 μm, and 11.6 μm for ANAR, 1AE, and 2AE respectively, and in the ANAR design Φ=109 degrees was used.

keeps a very high level over a broad wavelength range, and at the same time it has a lower leakage loss than 1AE and ANAR.

3.4 Fabrication tolerances

In designing HC-AR fibers it is important to demonstrate a good degree of robustness towards imperfections in the fabrication. As was recently done by Belardi et al. [18], we here consider robustness towards a uniform shift of the positions of the three nested tubes as a whole. From the SEM images in [18] and Fig. 1.1(f) such shifts in the position of the nested tube are apparent. Realistically, the shifts would be random from tube to tube, but nevertheless an investigation with a uniform shift will give an indication of the fabrication tolerances that can be allowed during the preform stacking preparation of this fiber type. The uniform shift of the nested tubes is denoted by the angle θ, as sketched in Fig. 3.13, and as seen there the leakage loss vs. θ at $\lambda = 2.94$ μm shows little variation when the angle varies quite significantly from 0° to 45°. When the angle is beyond 45°, the leakage loss increases significantly, indicating that a shift of 45° can be tolerated. In

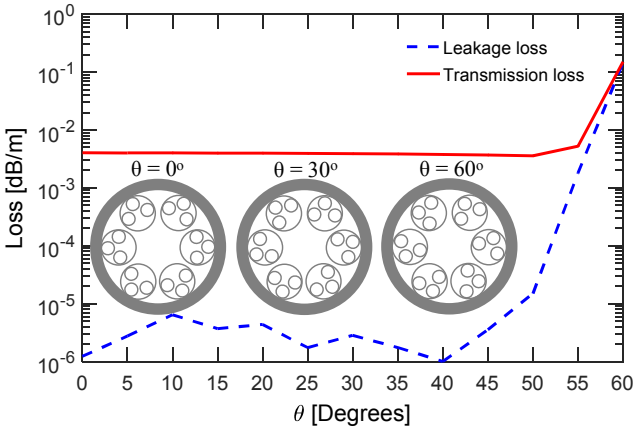

Figure 3.13. Predicted fabrication tolerances of the proposed ANAR fiber. The leakage loss is almost stable between 0° to 45°. The simulations were performed at $\lambda = 2.94$ μm.

the similar numerical work of Belardi the same qualitative behavior was observed and this maximum tolerance angle was found to be 30° [18].

3.5 Conclusion

In conclusion, we have numerically investigated a novel hollow-core fiber based on the anti-resonant reflecting guiding mechanism. In our proposed design the larger cladding tubes have three smaller adjacent nested anti-resonant (ANAR) tubes inside them, in contrast to earlier studies, where additional nested tubes were nested inside the larger nested tube. We considered two scaled versions of the same fiber design, one where the strut thickness was optimized for transmission in the mid-IR around $\lambda = 2.94$ μm, and one where the strut thickness was reduced by a factor of 3 to allow near-IR transmission around $\lambda = 1.06$ μm. These cases represent the behavior in the high-loss regime and the low-loss regime of the cladding material, respectively.

Each case has its challenges and solutions, but our results and discussions remain quite general and can therefore easily be used for other wavelengths and/or materials for the glass cladding.

We have studied the effects of the ANAR tubes on the fiber losses and modal properties. More specifically on the single-modeness of the ANAR fiber, we found that the higher-order-mode extinction ratio (HOMER) can be over 1500 in the near-IR in the range $\lambda = 1.0 - 1.1$ μm, and around 100 in the mid-IR at $\lambda = 2.94$ μm. In comparison, the structures with nested tubes from the literature had lower HOMER values. We found that the high-HOMER design has leakage losses that are increased significantly compared to the lowest level, but still it should be stressed that the leakage losses can be kept at a tolerable level. This can be attributed to the very low leakage loss of the optimal fiber design in the first place. Interestingly, the best overall near-IR performance was found in an optimized nested-in-nested design (2AE), which combined a high HOMER over a broad bandwidth with low leakage losses.

In our simulations we carefully optimized the size and placement of the ANAR elements. In particular for achieving a high HOMER level it was important to find the optimal angular position of the adjacent nested elements with respect to the center nested element and to adjust the diameter of the nested tubes; this optimization came at the expense of a higher leakage loss. The leakage losses were typically optimized by fine-tuning of the diameter of the nested tubes. Instead a rotation of the entire ANAR structure did not seem to influence the results much, which indicates that the design is quite robust towards fabrication variations.

The ANAR fiber when optimized to give the lowest leakage loss offers extremely low bending losses in near-IR even for a bend radius as low as 1 cm. The bend-loss levels are comparable to the HC-PBG fiber and would therefore be suitable for applications.

When comparing the performance of the ANAR design with the earlier proposed designs [19], we generally found that at a given target wavelength the ANAR design could outperform the design with a single nested anti-resonant element (1AE) and the design with a nested-in-nested element (2AE). In optimizing the designs the additional degree of freedom offered by the ANAR and 2AE designs was important to fine-tune the performance. It seems clear that the additional nested element(s) of the ANAR and 2AE designs allow for a stronger inhibited coupling of the core mode to the cladding modes than the 1AE design, which explains the lower losses obtained. From a production point-of-view, the 1AE design has already been realized [25], and in some sense the ANAR design is a generalization of this structure. Thus, we believe the ANAR fiber should be easier to make than the 2AE design.

We believe that the proposed ANAR design offers significant advantages and improvements over current designs, promising excellent performance for various applications in near and mid-IR wavelength regimes. We here used the well-known silica platform due to the many advantages it can offer in terms of production, cost etc., but we found that the record-low level of leakage loss was not fully exploited in the mid-IR due to the extremely high material loss of silica. It is therefore an obvious next step to consider the ANAR design based on a mid-IR transparent glass whereby the material losses are reduced to a level comparable to the low leakage losses promised by this design. This in turn would give record low bending losses and much higher HOMER levels. Considering the structural dimensions of the proposed fiber in the mid-IR (100 µm core diameter and outer tube diameter, 30 μm nested tube diameter and >1 μm strut thickness) this should not be a challenge for soft glass fiber technology.

References

[1] F. Poletti, "Nested antiresonant nodeless hollow core fiber," *Opt. Express*, vol. 22, no. 20, pp. 23807, 2014.

[2] F. Yu, W. J. Wadsworth, and J. C. Knight, "Low loss silica hollow core fibers for 3-4 μm spectral region," *Opt. Express*, vol. 20, no. 10, pp. 11153, 2012.

[3] N. M. Litchinitser, a K. Abeeluck, C. Headley, and B. J. Eggleton, "Antiresonant reflecting photonic crystal optical waveguides," *Opt. Lett.*, vol. 27, no. 18, pp. 1592, 2002.

[4] Y. Fei, "Hollow core negative curvature optical fibers," *Phd Thesis*, 2013.

[5] M. S. Habib, O. Bang, and M. Bache, "Low-loss hollow-core silica fibers with adjacent nested anti-resonant tubes," *Opt. Express*, vol. 23, no. 13, pp. 17394, 2015.

[6] M. S. Habib, O. Bang, and M. Bache, "Low-loss single-mode hollow-core fiber with anisotropic anti-resonant elements," *Opt. Express*, vol. 24, no. 8, pp. 8429, 2016.

[7] M. S. Habib, O. Bang, and M. Bache, "Low-loss Hollow-core Anti-Resonant Fibers with Semi-Circular Nested Tubes," *IEEE J. Sel. Top. Quantum Electron.*, vol. 22, no. 2, pp. 4402106, 2016.

[8] F. Couny, F. Benabid, P. J. Roberts, P. S. Light, and M. G. Raymer, "Generation and photonic guidance of multi-octave optical-frequency combs," *Science*, vol. 318, no. 5853, pp. 1118, 2007.

[9] S. Février, B. Beaudou, and P. Viale, "Understanding origin of loss in large pitch hollow-core photonic crystal fibers and their design simplification," *Opt. Express*, vol. 18, no. 5, pp. 5142, 2010.

[10] A. Argyros and J. Pla, "Hollow-core polymer fibres with a kagome lattice: potential for transmission in the infrared," *Opt. Express*, vol. 15, no. 12, pp. 7713, 2007.

[11] B. Debord *et al.*, "Hypocycloid-shaped hollow-core photonic crystal fiber Part I: Arc curvature effect on confinement loss," *Opt. Express*, vol. 21, no. 23, pp. 28597, 2013.

[12] A. F. Kosolapov *et al.*, "Demonstration of CO_2-laser power delivery through chalcogenide-glass fiber with negative-curvature hollow core,"

Opt. Express, vol. 19, no. 25, pp. 25723, 2011.

[13] W. Belardi and J. C. Knight, "Hollow antiresonant fibers with reduced attenuation," *Opt. Lett.*, vol. 39, no. 7, pp. 1853, 2014.

[14] A. D. Pryamikov, A. S. Biriukov, A. F. Kosolapov, V. G. Plotnichenko, S. L. Semjonov, and E. M. Dianov, "Demonstration of a waveguide regime for a silica hollow-core microstructured optical fiber with a negative curvature of the core boundary in the spectral region > 3.5 μm," *Opt. Express*, vol. 19, no. 2, pp. 1441, 2011.

[15] W. Belardi and J. C. Knight, "Hollow antiresonant fibers with low bending loss," *Opt. Express*, vol. 22, no. 8, pp. 9514, 2014.

[16] M. Heiblum and J. Harris, "Analysis of curved optical waveguides by conformal transformation," *IEEE J. Quantum Electron.*, vol. 11, no. 2, pp. 75, 1975.

[17] O. Humbach, H. Fabian, U. Grzesik, U. Haken, and W. Heitmann, "Analysis of OH absorption bands in synthetic silica," *J. Non. Cryst. Solids*, vol. 203, pp. 19, 1996.

[18] W. Belardi, "Design and properties of hollow antiresonant fibers for the visible and near infrared spectral range," vol. 33, no. 21, pp. 4497, 2015.

Chapter 4

Semi-circular nested tube hollow-core anti-resonant fiber

In chapter 3, we show that if the anti-resonant tubes have nested tubes inside them, the loss performance significantly improves and shows effectively single-mode operation. In this chapter, we investigate the role of the shape and position of these nested tubes of hollow-core anti-resonant fibers in terms of loss performance and single mode operation.

4.1 Why HC-AR fibers with semi-circular nested tubes?

Until now, though, only a full circular nested element has been considered, but the question is how the core mode is influenced if the nested element interior boundary position is kept fixed while its curvature is changed, or when the nested element interior boundary curvature is fixed and its position is changed. Such "semi-circular" scenarios could come up in a production stage [1] (see Fig. 4.1), and even if they seem less ideal than a nested element consisting of a perfect full circle, we here show that often the penalty is quite small and in some cases the semi-circle design might even improve the loss performance of the fiber. That notwithstanding, the main goal of the work is to get an intuition about whether it is the curvature or the position of the nested element that is critical for the optimal low-loss performance, and our results point towards the position as the most critical parameter.

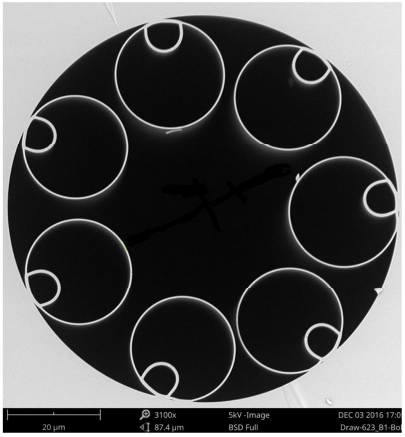

Figure 4.1. SEM image of nested HC-AR fiber. The inner capillaries are semi-circular in shape. Image courtesy: Microstructured Fibers and Devices Group, CREOL, University of Central Florida, USA).

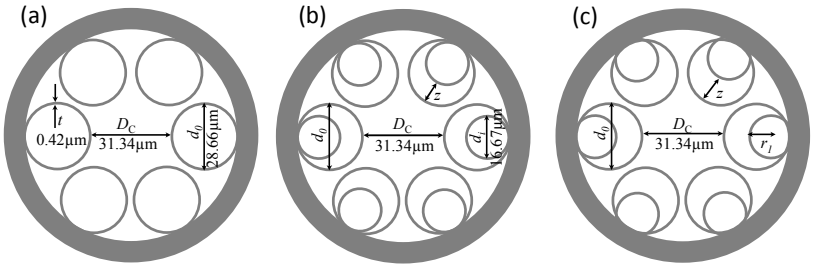

Figure 4.2. Geometries considered in the near-IR simulations. (a) Typical optimized HC-AR fiber design with six circular tubes; (b) the nested ("1AE", i.e. one anti-resonant element) design proposed in [2] in which $d_i = 16.67$ μm; (c) our proposed structure with one semi-circular anti-resonant element (1SAE). All fibers have the same core diameter $D_c = 31.34$ μm, $d_0 = 28.66$ μm and uniform silica strut thickness $t = 0.42$ μm.

4.2 Geometry of the proposed design

As the structure described in chapter 3 for near-IR calculations, we consider an HC-AR fiber with 6 circular anti-resonant tubes, fixing the core diameter to $D_c = 31.34$ μm (defined as the maximum diameter

of a circle that can be inscribed inside the core). The silica wall (strut) thickness of $t = 0.42$ μm was chosen so that an anti-resonant first-order transmission window has a loss minimum in the near-IR range (specifically around $\lambda = 1.06$ μm, the suitably chosen target wavelength of our designs). Figure 4.2 shows the three considered designs, all shown in the configuration optimized to give minimal leakage loss (α_c) at $\lambda = 1.06$ μm. Figure 4.2(a) shows the geometry of a "typical" HC-AR fiber [3] with six anti-resonant tubes in which tubes are separated each other forming so-called node-free configuration. The modified HC-AR fiber proposed by Poletti [2], is shown in Fig. 4.2(b) in which smaller tubes having diameter of d_i are nested with the original tubes of diameter d_0. It is here shown in the configuration giving the lowest leakage loss at 1.06 μm [4]. The structure under investigation is shown in Fig. 4.2(c), using semi-circular anti-resonant tubes. The perimeter distance between the outer tubes is 1.33 μm for all designs. The separation between the inner and outer tubes along the radial direction is indicated by z which is 11.17 μm for the minimal leakage loss shown in Fig. 4.2(b-c). The leakage (confinement) loss was modeled using the same approach as mentioned in chapter 3.

4.3 Leakage loss and single-mode operation

4.3.1 Effect of changing air-hole radius, r_1

First, we investigated the effect of changing the inner air-hole radius r_1 while keeping the distance between the core boundary and the interior boundary of the nested element, z, fixed to 11.17 μm (this is the value that comes out when optimizing the 1AE structure to give the lowest leakage loss). We specifically monitor the leakage loss and higher-order-mode extinction ratio (HOMER). The change in the inner air-hole radius allows us to investigate several fiber structures with the same core

diameter D_c, silica strut thickness t, and the separation between the inner and outer tubes z; the only thing that changes is that as the nested element becomes semi-circular, its curvature becomes more and more flat. The geometrical configurations for different inner air-hole radii are shown in the right hand side of Fig. 4.3. The inner air-hole radius $r_1 = 8.33$ μm corresponds to the original 1AE structure proposed in [2], so when $r_1 < 8.33$ μm the inner tube will be "floating" in the outer tube (an unphysical scenario, but nevertheless possible to model), and when $r_1 > 8.33$ μm the inner air-hole tube will no longer be a full circle and instead becomes semi-circular. It can be seen from Fig. 4.3 that a dramatic change in the leakage loss is observed when the inner and outer tubes start floating at around $r_1 = 7$ μm while it is only weakly changing in between $r_1 = 8.33 - 30$ μm. The minimum leakage loss (that is for physical values of the radius) is actually obtained at $r_1 = 9$ μm when the inner air-hole tubes start being semi-circularly shaped. Thus, we conclude that the curvature plays a minor role as there is only around a factor of 2 variations from the full circle to an almost flat line. In other words, the penalty for having an imperfect nested element or even just a "crossbar" in the outer circle is insignificant. Important to note, the small ripples (fluctuations) of FM and minimum HOM loss is due to the anti-crossings with ring guided modes of high azimuthal number [2], [5]. The HOMER can be made higher by reshaping the size of the inner anti-resonant tubes and we found HOMER to reach a value of more than 100 when r_1 is higher than 13 μm. That being said, also HOMER is quite constant as the nested element curvature flattens.

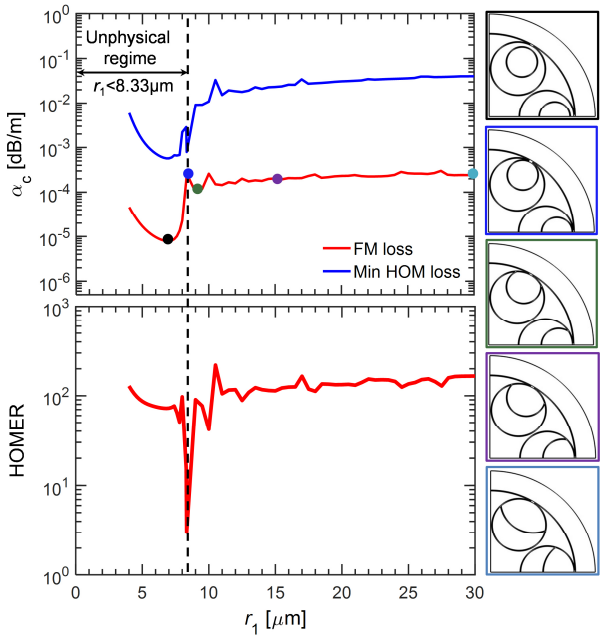

Figure 4.3. Calculated leakage loss and HOMER as a function of the inner air-hole radius r_1 keeping z fixed to 11.17 μm. All structures have the same core diameter $D_c = 31.34$ μm and uniform silica strut thickness $t = 0.42$ μm. The color of the frame corresponds to the color of the dot points in the plot.

4.3.2 Effect of changing tube separation z

The effect of changing the tube separation z while keeping r_1 fixed (to the value from the loss-optimized 1AE design) is investigated which is shown in Fig. 4.4. A dramatic drop in leakage loss is also observed for the unphysical case. The maximum HOMER is found to be ~2000 (z~16.20 μm) which is far higher than the original 1AE design (z = 11.17 μm). We observe that the HOMER value increases as the nested tube is removed away from the core boundary; while the FM leakage loss is almost constant from the starting value and the HOM loss increases quickly. The leakage loss starts increasing when z>16.20 μm

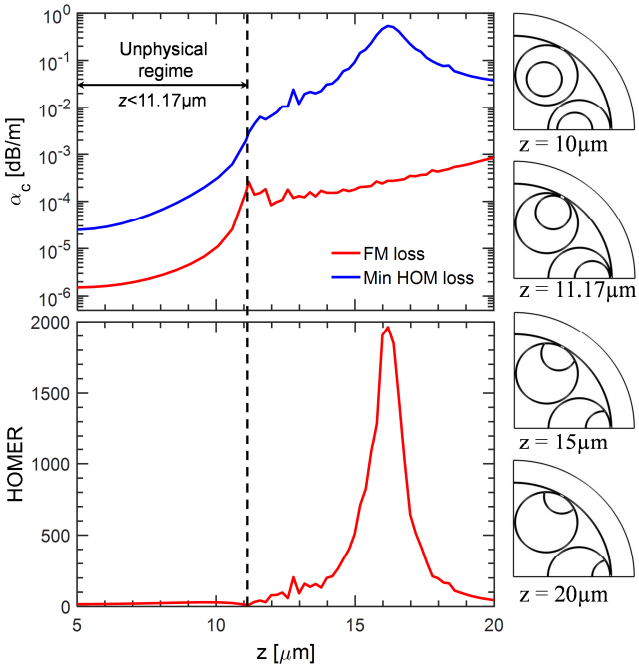

Figure 4.4. Calculated leakage loss and HOMER as a function of the tube separation z keeping r_1 fixed to 8.33 μm. All structures have the same core diameter $D_c = 31.34$ μm and uniform silica strut thickness $t = 0.42$ μm.

and the change in the leakage loss is much more pronounced by the variation of tube separation compared to the variation of r_1 (see Fig. 4.3). We conclude that the FM leakage loss increases somewhat when the distance is increased, but since the HOM losses increase much faster the HOMER quickly becomes extremely large. Therefore the distance has a much more pronounced effect than the curvature on the loss performance.

To understand the coupling effect between the core-guided modes and cladding modes we have plotted the effective mode index (n_{eff}) and leakage loss as a function of z from 12 to 20 μm which is shown in Fig. 4.5. It can be seen from the effective index profile that the effec-

tive index of the FM core- mode (LP_{01}) has higher refractive index than the cladding modes which results in weak coupling between the core and cladding modes and remains almost independent of z. The core-guided HOM experiences a strong phase matching with the cladding modes at z~16.20 μm which results in high HOM loss. A weak interaction between the core-guided HOMs and cladding modes take place away from the phase matching (see modal spectrum for $z = 12$ μm and for $z = 20$ μm) [6].

4.3.3 Optimizing 1AE design for Maximum HOMER

In this section, we investigate the 1AE design in the case where it is optimized to give the maximum HOMER value; as mentioned in [4] the design needs to sacrifice the lowest loss in order to maximize HOMER. First we change the inner air-hole radius r_1 while keeping the separation z fixed to the value 15.83 μm found in the 1AE optimized design.

It can be seen from Fig. 4.6 that leakage loss is almost constant by the variation of inner air-hole radius; this is similar trend to what we found for the optimized loss case (see Fig. 4.3). However, in this case the HOM losses decrease when the nested curvature flattens, so the HOMER decreases with the increase of the inner air-hole radius.

Lastly, the effect of tube separation z on the leakage loss and HOMER is also investigated. It can be seen from Fig. 4.7 that the leakage loss increases with the increase of the distance between the core and the interior boundary of the nested tube z, while keeping the curvature fixed. The leakage loss dramatically decreases for the unphysical case when < 15.83 μm. Therefore, we can say that the tube separation z plays a more important role on the leakage loss compared to the curvature of the nested tubes (when compared to Fig. 4.3 and 4.6).

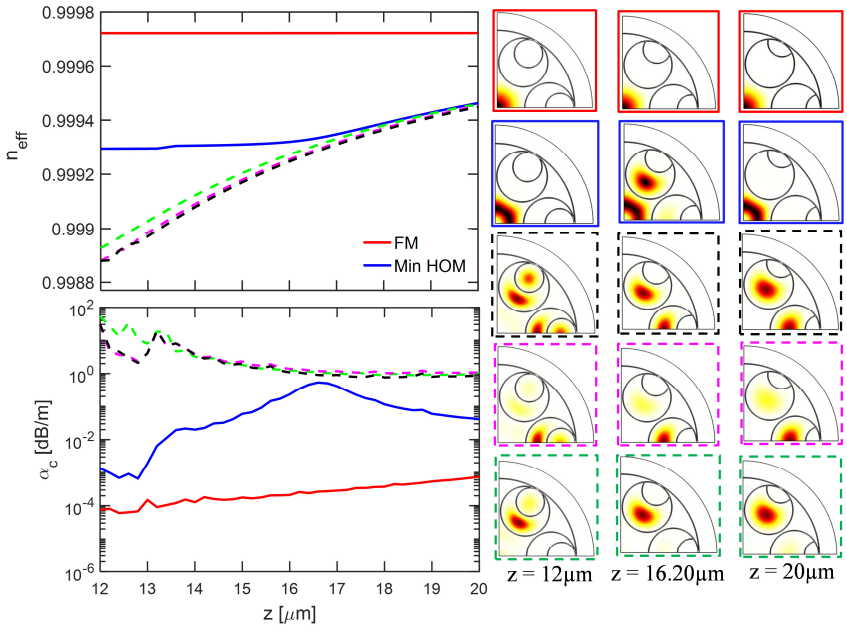

Figure 4.5. Effect of changing tube separation z on effective mode index and leakage loss. All structures have the same core diameter D_c = 31.34 μm , r_1= 8.33 μm , and uniform silica strut thickness t = 0.42 μm . The color of the frame corresponds to the color of the line in the plot.

Notably, maximum HOMER is obtained for the original 1AE design i.e., z~16 μm and r_1 = 6 μm.

The effect of changing r_1 and z on the leakage loss is shown in Fig. 4.8. It can be seen from Fig. 4.8 that the leakage loss is almost constant in between z = 11.17 to 18 μm and r_1=9 to 17 μm. The loss is quite constant along r_1 for a given z, while generally the loss increases as z is increased for a fixed r_1. This supports the conclusion found above that the curvature plays a minor role, while the distance from the core to the interior boundary position of the nested element is more critical.

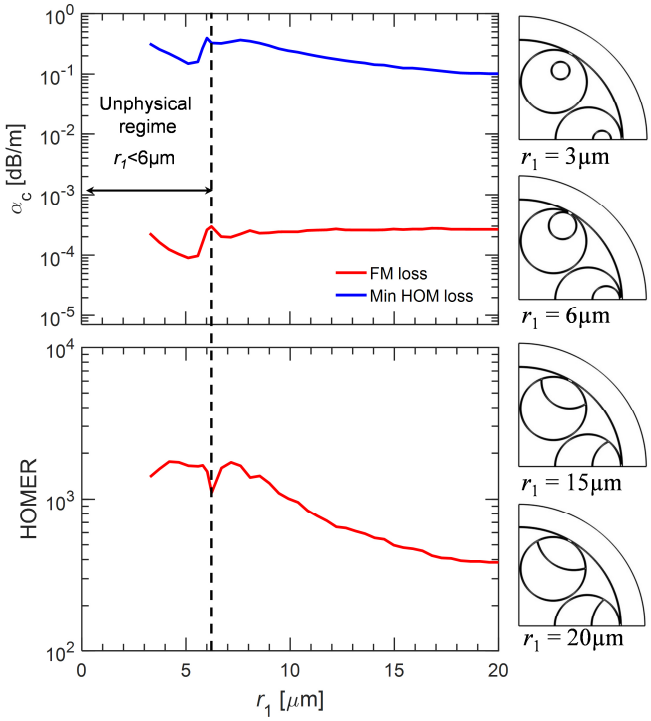

Figure 4.6. Effect of changing r_1 on leakage loss and HOMER with a fixed $D_c = 31.34\ \mu\text{m}$, $t = 0.42\ \ \mu\text{m}$, $z = 15.83\ \mu\text{m}$, $d_0 = 28.66\ \mu\text{m}$ and $\lambda = 1.06\ \mu\text{m}$.

4.4 Leakage loss spectra and bending loss

The leakage loss for the optimized parameters as a function of wavelength in the near-IR spectral regime is shown in Fig 4.9. We have neglected the material loss of silica to calculate the total loss because the measured loss of dry F300 silica is of the order of 10^{-3} dB/m [7] or less in the wavelength range between 0.95 and 1.40 μm. The calculated power fraction in silica of the optimum 1SAE structure with the lowest leakage loss is less than 10^{-4} in this spectral regime, and similar values are found for the 1AE structure.

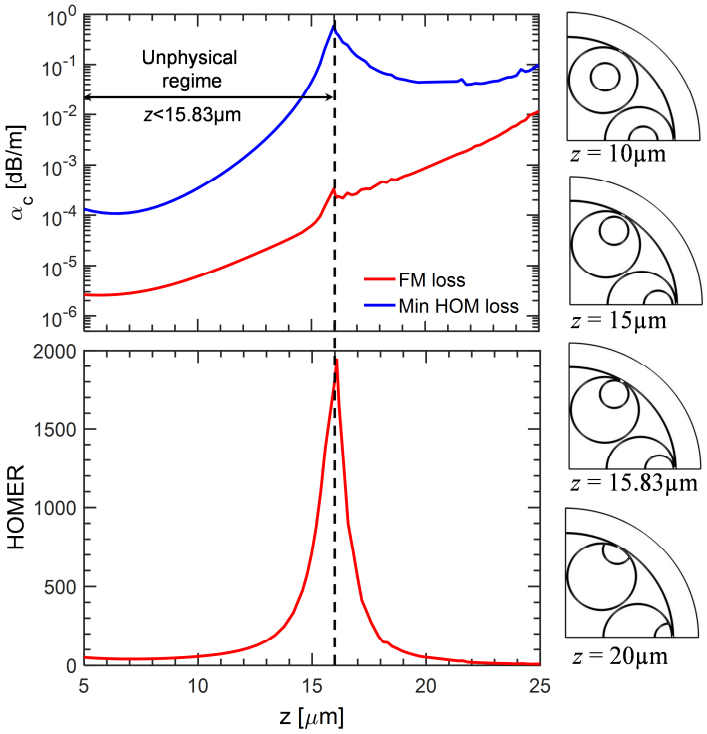

Figure 4.7. Effect of changing z on leakage loss and HOMER with a fixed $D_c = 31.34$ μm, $t = 0.42$ μm, $r_1 = 6$ μm, $d_0 = 28.66$ μm and $\lambda = 1.06$ μm.

Therefore, the transmission loss will practically be equivalent to the leakage loss. It can be seen from the leakage loss spectra of Fig. 8 that the 1SAE fiber has a leakage loss of 0.1dB/km at 1.06 μm, which is roughly a factor of 2 lower than 1AE. This shows that at the target wavelength, the semi-circular design 1SAE actually outperforms the ideal full-circle design 1AE, although over the whole spectrum the 1AE design performs slightly better. It is remarkable to see that the lowest leakage loss for the 1AE design is found at a longer wavelength than the $\lambda = 1.06$ μm wavelength it is optimized for, unlike the "typical" and 1SAE designs. This can happen because the optimization is done only locally.

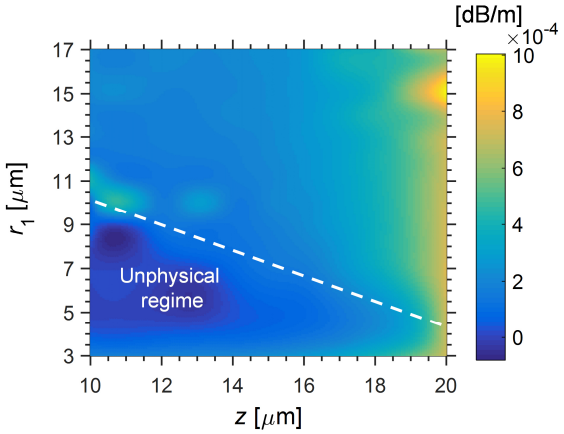

Figure 4.8. Calculated leakage loss with different values of r_1 as a function of z. The simulations are performed at $\lambda = 1.06$ μm.

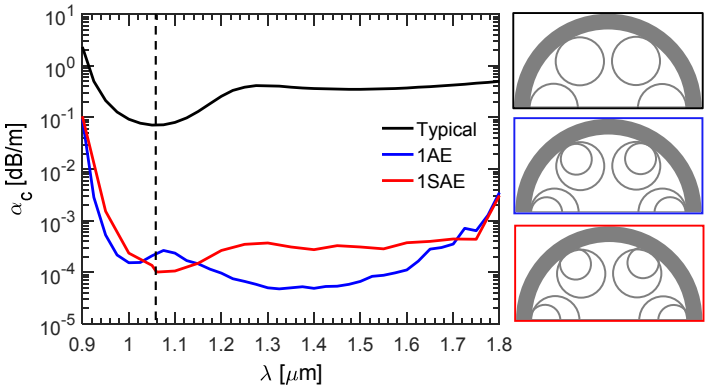

Figure 4.9. Calculated loss spectra. Calculated loss spectra. All fibers have the same core diameter Dc = 31.34 μm, d_0 = 28.66 μm and uniform silica strut thickness t=0.42 μm. The optimum parameters for 1AE and 1SAE structures are z = 11.17 μm, r_1 = 8.33 μm and z = 11.17 μm, r_1=9 μm respectively. The color of the frame corresponds to the color of the line in the plot. The thin dotted line indicates the wavelength for which the losses are optimized.

Let us now consider the bending loss, which is calculated by transforming the bent structure into its equivalent straight structure with equivalent refractive index profile, n_{eq} [8] which is calculated using Eq. (3.3).

The bending loss was calculated at 1.06 μm and the bending direction was chosen along the x-axis giving the bend-loss curve shown in Fig. 4.10. Evidently the 1SAE design has a lower bending loss than the 1AE design for bend radii between 7 and 40 cm which is due to the weak coupling between the core-guided mode and the cladding modes [9] and the leakage loss is only weakly changing for bend radii above ~20 cm, but for low bending radius the 1AE design shows lower bending loss than 1SAE design. It can also be seen from Fig. 4.10 that a few loss peaks were observed for the "typical" design as the bend radius is decreased, while no loss peaks were observed for the 1AE and 1SAE designs.

The bending loss as a function of the tube separation z ($r_1 = 8.33$ μm) and inner air-hole radius r_1 ($z = 11.17$ μm) is shown in Fig. 4.11. The bending loss increases sharply for a tube separation larger than 15 μm whereas the bending loss is weakly changing by the variation of the inner air-hole radius r_1. Again we may conclude that changing the nested element curvature gives an insignificant penalty in the performance, while the distance is much more critical.

4.5 HOMER as a function of z and r_1

The semi-circular nested element design offers an extra degree of design freedom compared to the full-circle nested element design. We therefore need to perform a 2D optimization of HOMER, which is shown in Fig. 4.12. It is performed by systematically changing the separation between the inner and outer air-hole tubes z and air-hole radius r_1. The optimum HOMER is found to be over 2000 at $z = 16.5$ μm and $r_1 = 8.2$ μm. The corresponding leakage loss of the FM is shown in Fig. 4.13 in which we see that the leakage loss is weakly changing by the variation of both z and r_1, but clearly the design with the lowest leakage loss is not the same as the design with the highest HOMER.

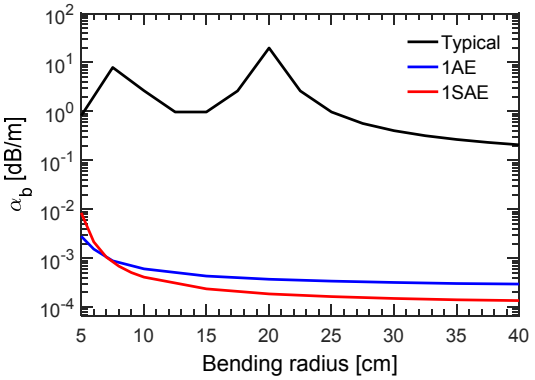

Figure 4.10. Calculated bending loss at 1.06 μm versus bending radius; all chosen designs are optimized to give the lowest leakage loss. The contour plots of the fundamental air-core mode distribution are shown in the right hand side for a 10 cm bending radius. The color of the frame corresponds to the color of the line in the plot.

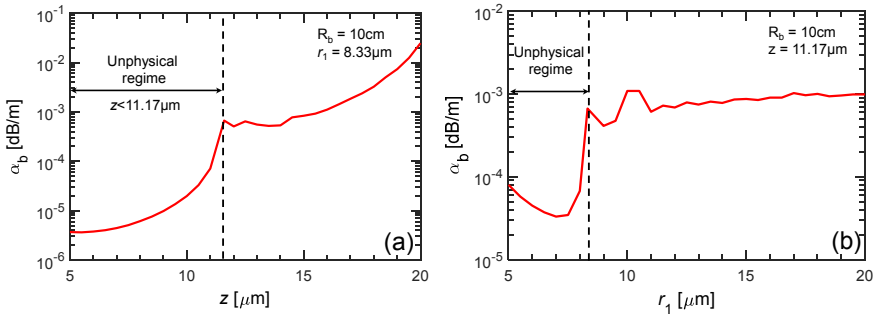

Figure 4.11. Calculated bending loss as a function of (a) tube separation z (b) inner air-hole radius r_1 for 10 cm bending radius at 1.06 μm.

For completeness Fig. 4.14 shows the wavelength dependence of the leakage loss of the FM, the minimum HOM loss, and the HOMER in the near-IR spectral regime; for each design the structure is optimized to give the maximal HOMER. HOMER can be made in excess of 1,000 in the range of 1.1-1.15 μm and over 2000 at 1.06 μm for r_1=8.2 μm, and $z = 16.5$ μm, which makes the fiber effectively single-moded in the near-IR spectral regime. Also the 1AE design has excellent HOMER

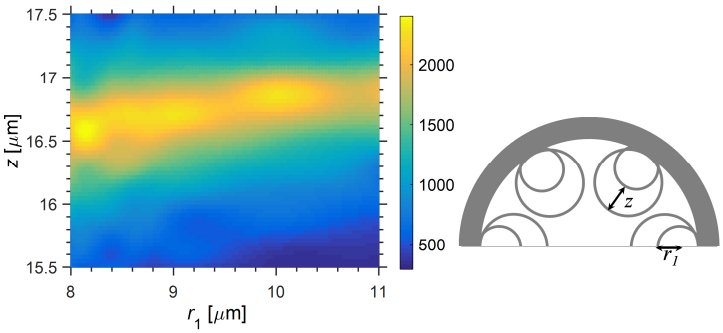

Figure 4.12. Calculated HOMER with different values of z as a function of r_1. The simulations are performed at $\lambda = 1.06$ μm.

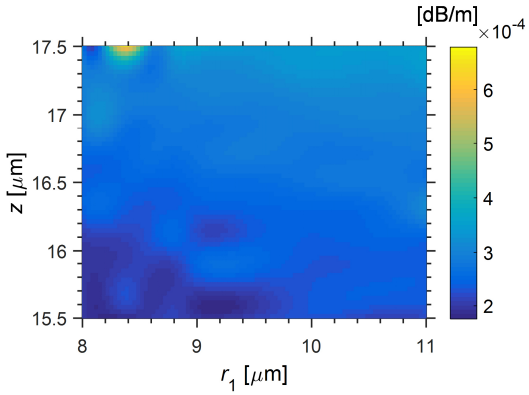

Figure 4.13. Calculated leakage loss with different values of z as a function of r_1. The simulations are performed at $\lambda = 1.06$ μm.

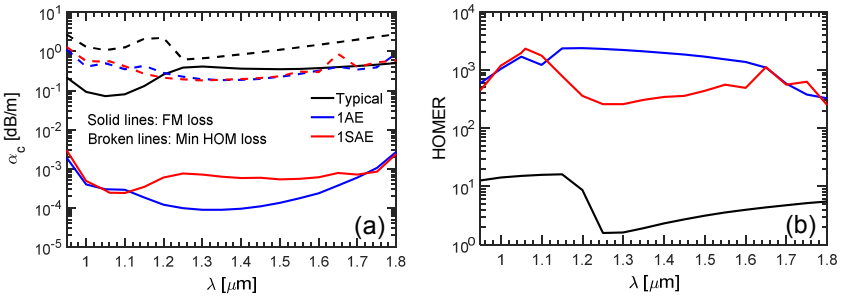

Figure 4.14. Wavelength dependence of (a) leakage loss and (b) HOMER for the optimized parameters. The optimum design parameters are:$D_c = 31.34$ μm, $t = 0.42$ μm, $d_0 = 28.66$ μm, and inner air-hole radius $r_1 = 6\mu$m, and 8.2μm for 1AE, and 1SAE respectively.

performance, and at the same time it has a lower leakage loss than 1SAE design.

4.6 Conclusion

Concluding, we have thoroughly investigated the effect of the shape and position of a single nested anti-resonant element on the overall loss performance of a hollow-core anti-resonant fiber. We allowed the circular nested element to become semi-circular, and thus we could independently investigate the effects of curvature and position of the nested element. We found through numerical simulations that changing the distance between the core boundary and the nested anti-resonant element boundary significantly affects the loss performance; in some cases it deteriorates the performance while in other cases is vastly improves the performance. We even found that the semi-circular case could outperform the optimized full-circle nested element design. Instead the curvature of the nested element had a very little impact on the loss performance. This means that it is not crucial to have a nested element with a negative curvature, but its position is much more crucial. These results should give a better intuition when designing anti-resonant fibers with nested elements, and we expect that this will lead to novel designs with improved performance.

References

[1] W. Belardi, "Design and properties of hollow antiresonant fibers for the visible and near infrared spectral range," *IEEE* J. Light. Technol., vol. 33, no. 21, pp. 4497, 2015.

[2] F. Poletti, "Nested antiresonant nodeless hollow core fiber," *Opt. Express*, vol. 22, no. 20, pp. 23807, 2014.

[3] A. D. Pryamikov, A. S. Biriukov, A. F. Kosolapov, V. G. Plotnichenko, S. L. Semjonov, and E. M. Dianov, "Demonstration of a waveguide regime for a silica hollow--core microstructured optical fiber with a negative curvature of the core boundary in the spectral region > 3.5 μm," *Opt. Express*, vol. 19, no. 2, pp. 1441, 2011.

[4] M. S. Habib, O. Bang, and M. Bache, "Low-loss hollow-core silica fibers with adjacent nested anti-resonant tubes," *Opt. Express*, vol. 23, no. 13, pp. 17394, 2015.

[5] L. Vincetti and V. Setti, "Waveguiding mechanism in tube lattice fibers," *Opt. Express*, vol. 18, no. 22, pp. 23133, 2010.

[6] P. Uebel *et al.*, "Broadband robustly single-mode hollow-core PCF by resonant filtering of higher-order modes," *Opt. Lett.*, vol. 41, no. 9, pp. 1961, 2016.

[7] W. Belardi and J. C. Knight, "Hollow antiresonant fibers with reduced attenuation," *Opt. Lett.*, vol. 39, no. 7, pp. 1853, 2014.

[8] M. Heiblum and J. Harris, "Analysis of curved optical waveguides by conformal transformation," *IEEE J. Quantum Electron.*, vol. 11, no. 2, pp. 75, 1975.

[9] W. Belardi and J. C. Knight, "Hollow antiresonant fibers with low bending loss," *Opt. Express*, vol. 22, no. 8, pp. 9514, 2014.

Chapter 5

Anisotropic tube hollow-core anti-resonant fiber

This chapter discusses the effect of curvature of novel hollow-core anti-resonant (HC-AR) fiber on overall loss performance and effectively single-mode guidance. We show that the loss performance and higher-order mode suppression is significantly improved by using symmetrically distributed anisotropic anti-resonant tubes in the cladding, elongated in the radial direction, when compared to using isotropic, i.e. circular, anti-resonant tubes. The effective single-mode guidance of the proposed fiber is achieved by enhancing the coupling between the cladding modes and higher-order-core modes by suitably engineering the anisotropic anti-resonant elements. Finally, we discuss the transmission and loss measurements of some novel HC-AR fibers.

5.1 Geometry of the proposed design

Figure 5.1(a)-(c) shows the considered HC-AR fiber geometries, using a thick outer capillary with AR tubes on the inner wall. Design (a) is the usual case with touching isotropic (circular) AR cladding tubes. Starting from (a), the design is optimized for minimal losses, resulting in the circular design (b) and elliptical design (c). The latter is the proposed anisotropic AR tube design, here an ellipse squeezed in the azimuthal direction. Other anisotropic shapes are possible. Here we propose a simpler solution using anisotropic AR tubes, elongated along the fiber radial direction, which allows simultaneously achieving (a) an increased negative curvature in the core, (b) a node-free design, and (c) a larger distance from the core to the outer capillary. All these properties could

not be achieved simultaneously in the previous cases[1]–[8]. We focus on a silica fiber designed for $\lambda = 1.06$ μm (i.e. for high-power Yb lasers), which has 6 AR tubes (a larger number is also feasible, and below we will specifically compare 6 vs. 8 AR tubes), a fixed core diameter $D_c = 30$ μm (large enough to enable high-power transmission) and silica strut thickness $t = 0.42$ μm (making the first high-loss resonance occur at around $\lambda = 0.88$ μm [5]). This choice of strut thickness implies that light at 1.06 μm is guided in the fundamental AR transmission band, which compared to the next higher-order AR transmission bands is favorable since it performs better in terms of loss and transmission bandwidth. The ellipticity is defined as $\eta = d_y/d_x$, where d_y is the diameter in the azimuthal direction and d_x is the radius in the radial direction; in the following we keep $d_x = 30$ μm fixed, and $\eta < 1$ will reduce the loss. We used a quarter of the geometry for the numerical calculations because of mode symmetry [9], except for the bend loss calculations where a half geometry was used due to a reduced symmetry in the elliptical case. We used the same numerical method as described in chapter 3, which briefly explained relies on finite-element simulations to calculate the fiber modes and their propagation constants.

5.2 Optimizing leakage loss of HC-ARFs

First the HC-AR fibers were optimized to get the lowest loss at 1.06 μm by adjusting the size of the AR elements with the core size fixed (see [4] for details on the calculations). Figure 5.2(a) shows the leakage loss (or confinement loss, α_c) as a function of AR air-hole radius ($r = d/2$) for the circular case. When the AR tube radius decreases from $r = 15$ *to* 10.2 μm, the leakage loss decreases to a minimum value of 30 dB/km, i.e. improved with around one order of magnitude. Interestingly, the AR tubes are here much smaller than the “non-touching”

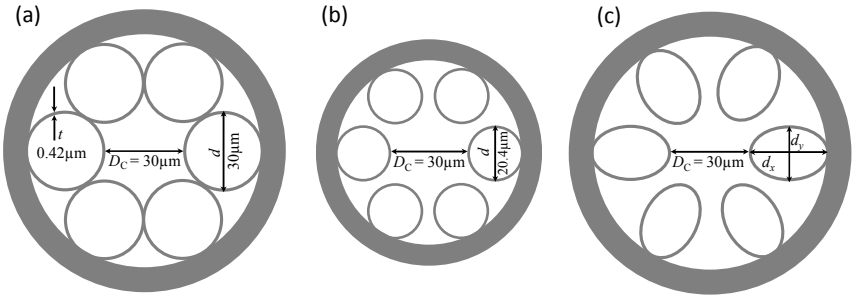

Figure 5.1. Geometry of the considered HC-AR fibers, keeping fixed the core diameter $D_c = 30\ \mu$m and silica strut thickness $t = 0.42\ \mu$m. The structural parameters shown in the figure are those that optimized the leakage loss at 1.06 μm. The figures are scaled to indicate their relative size.

node-free design (i.e. where the AR tubes are reduced just enough to prevent them from touching each other), which otherwise has been considered optimal [5], [7]: the reasoning has been that the core FM no longer has coupling loss to the cladding modes that in the touching-case reside in the glass intersections in these nodes. However, this would imply a sharp drop in loss as r is taken below 15 μm to the non-touching value. Instead it is continuous, indicating that the coupling loss to the cladding modes in the glass nodes is not dominating for the chosen fiber design (however, this does not mean that for other designs it is not important), and the loss instead drops smoothly because the FM phase-mismatch to the cladding modes increases gradually. This is eventually balanced with the increased loss of the FM as its evanescent tail overlaps more with the outer capillary wall as the circles shrink. This is because we here fix the core size, so the shrinking circles imply that the outer capillary becomes closer to the core.

Figure 5.2(b) shows the leakage loss for the elliptical case. As we fix the core size and decrease η, the major axis (in radial direction) is fixed at $d_x = 30\ \mu m$, and the minor axis (in the azimuthal direction) changes from $d_y = 30\ to\ 18\ \mu m$.

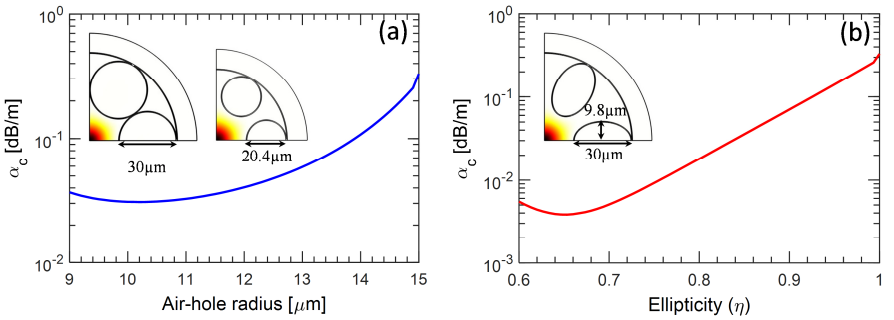

Figure 5.2. Calculated leakage loss at 1.06 μm as a function of (a) air-hole radius for circular AR tubes and (b) ellipticity of the AR tubes keeping $d_x = 30\ \mu m$. Inset: FM field profiles at 1.06 μm. All structures have the same core diameter $D_c = 30\ \mu m$ and uniform silica strut thickness $t = 0.42\ \mu m$.

The lowest leakage loss of 4 dB/km was obtained for $\eta = 0.65$, i.e., $d_x = 30\ \mu m$ and $d_y = 19.60\ \mu m$. Thus, orders of magnitude improvement is realized by squeezing the azimuthal axis of the AR tubes. The minimum has a different explanation than the circular case, because we are here able to fix the distance from the core to the outer capillary. Instead the loss improvement obtained for $\eta < 1$ is due to an increased phase mismatch between the FM and cladding modes is eventually balanced by an increased leakage loss as the FM starts leaking into the voids between the ever slimmer AR ellipses.

Figure 5.3 depicts the spectral loss distribution for different HC-AR fibers. Curves 1-3 show the circular cases: case 1 (green) where the tube walls are touching each other, thus forming glass nodes in the cladding, and case 2 when the air- hole radius is reduced to 14 μm so the AR tubes no longer touch each other (black). Case 3 (blue) shows the additional reduction of leakage loss until the minimum is reached, achieved as mentioned above by shrinking the circular tubes further (thus separating them further). Finally, case 4 (red) shows the elliptical design, displaying significantly improved loss performance; the leakage

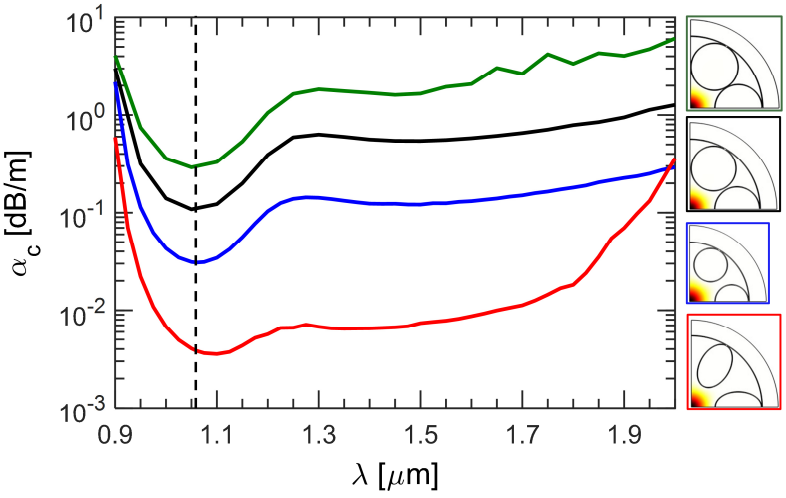

Figure 5.3. Calculated leakage as a function of wavelength for different HC-AR fibers (dashed line: $\lambda = 1.06$ μm). All structures have the same core diameter $D_c = 30$ μm and uniform silica strut thickness $t = 0.42$ μm. The color of the frame corresponds to the color of the line in the plot.

loss is over one order of magnitude lower than for the best circular design. Moreover, the low-loss range spans nearly the entire near-IR, which is promising for broadband ultrafast applications.

5.3 Scaling strut thickness of AR tubes

One of the limiting factors in high-power beam delivery is the so-called fraction of power in silica (FOPS), i.e., the optical power overlap with the silica cladding, which should be kept small. Figure 5.5(a) shows that FOPS can be reduced by reducing the strut thickness of silica ($\sim 2 \times 10^{-5}$ at 1.06 μm for $t = 0.35$ μm), which is several orders of magnitude lower than the HC-PBG [10]. This makes HC-AR fibers an ideal medium to explore propagation of high power beam delivery. When comparing FOPS for circles and ellipses the performance is similar, but the advantage in using ellipses comes in terms of leakage loss,

see Fig. 5.4(a), which has a local minimum at a wavelength controlled by the strut thickness. As the strut thickness is reduced, this minimum shifts towards lower wavelengths, but at the wavelength of 1.06 μm that the design is intended for the leakage loss becomes quite high as the strut thickness is reduced. In the elliptical case the wavelength loss-variation is instead much more flat, so the leakage loss at 1.06 μm varies only little when the strut thickness is reduced. Figures 5.4(b) and 5.5(b) summarizes these trends by showing the leakage loss and FOPS vs. strut thickness at 1.06 μm for both cases: elliptical tubes have one order of magnitude lower losses compared to circular tubes when the strut thickness varies from 0.30 to 0.42 μm (note the y-axis is linear); in turn the FOPS is almost the same for both cases. The elliptical design will therefore allow for more design degrees of freedom. Note that $t = 0.30$ μm is generally considered a practical limit for proper fiber cleaving, rather than a fabrication limit. This limit is less severe for silica HC-AR fibers at longer wavelengths as this demands larger strut thicknesses, in which case the potential of the elliptical design can be exploited fully.

5.4 Effectively single-mode operation

HC-AR fibers with large cores are not single-moded, but they can be made effectively single-moded by engineering the shape and size of the AR tubes so the HOMs experience more loss than the FM [4]. Figure 5.6 shows the relative effective indices ($\Delta n_{\text{eff}} = n_{\text{eff}} - 1$) of the first three core modes (here denoted LP_{01}, LP_{11}, and LP_{21}) and the first three cladding modes. The core FM (LP_{01}) has the highest Δn_{eff}, which remains constant as a function of ellipticity. The first three cladding modes have only slightly larger Δn_{eff} than the first core HOM (LP_{11}) because the core area is only a few times larger than the area of a single cladding tube.

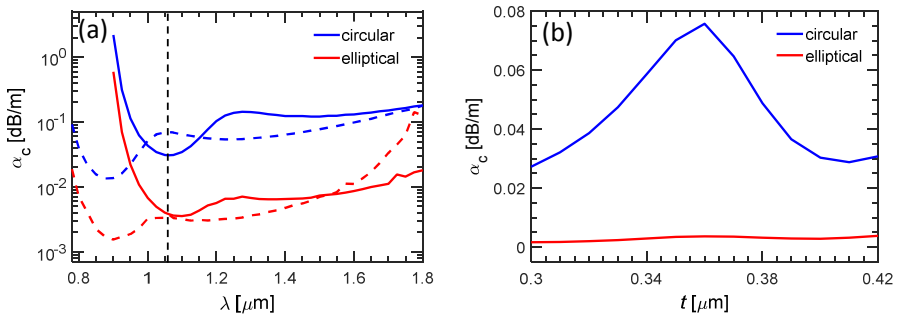

Figure 5.4. Calculated leakage loss as a function of wavelength (a) and silica strut thickness (b). Solid lines and dashed lines are calculated for $t = 0.42$ μm and $t = 0.35$ μm respectively. Leakage loss vs. strut thickness in (b) is calculated at $\lambda = 1.06$ μm.

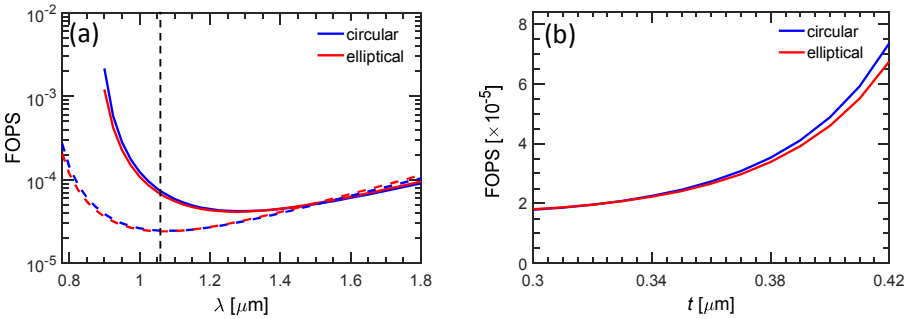

Figure 5.5. Calculated fraction of power in silica (FOPS) as a function of wavelength (a) and silica strut thickness (b). Solid lines and dashed lines are calculated for $t = 0.42$ μm and $t = 0.35$ μm respectively. FOPS vs. strut thickness in (b) is calculated at $\lambda = 1.06$ μm.

Thus, the first HOM is located within the domain of the cladding modes, which increases phase matching to cladding modes [11], [12]. This effect is more evident for the strongly elliptical AR tubes (η~$0.60 - 0.70$), where the cladding modes are better phase-matched to the HOMs than to the FM, which effectively suppresses the guidance of the HOMs due to higher losses The FM loss decreases much more than the HOM loss when the ellipticity is decreased, and in the $\eta = 0.60 -$ 0.70 range the HOM losses even start increasing while the FM loss

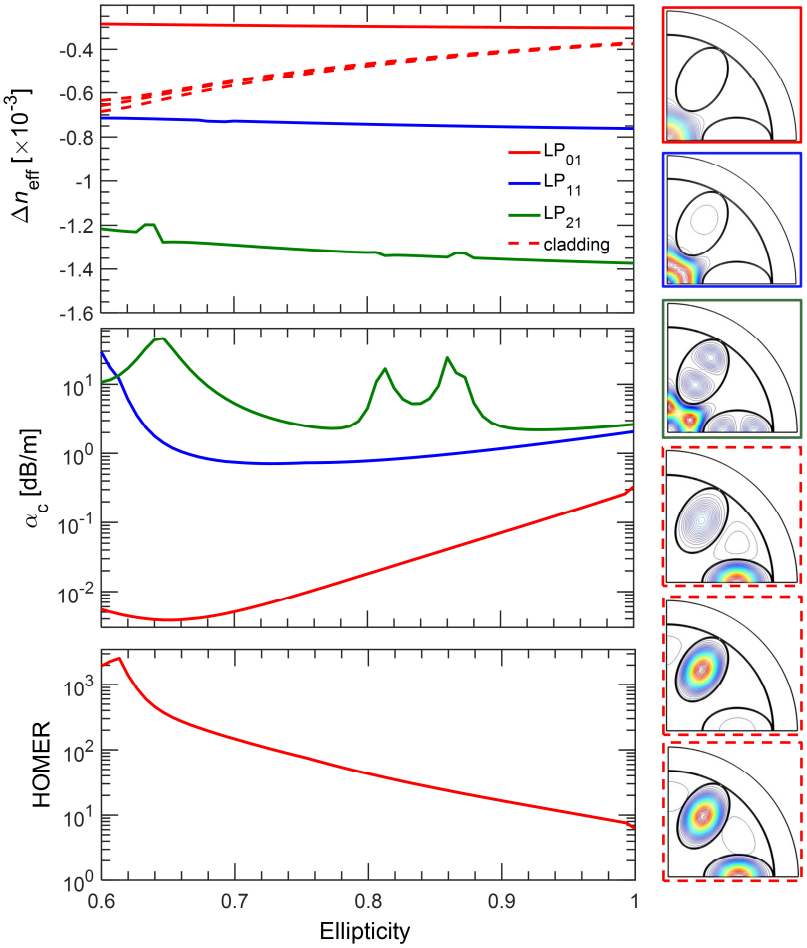

Figure 5.6. Relative effective index, loss and higher-order-mode extinction ratio (HOMER) vs. ellipticity for $\lambda = 1.06$ μm. All structures have the same core diameter $D_c = 30$ μm and uniform silica strut thickness $t = 0.42$ μm. The color of the frame corresponds to the color of the line in the plot.

remains at 4 dB/km. This shows how the HOM losses can be made higher by suitably choosing the ellipticity. The aim is maximizing the so-called HOM extinction ratio (HOMER), defined as the ratio between the loss of the HOM with the lowest loss and the FM loss [5]. The maximum HOMER was found to be ~2500 at η~0.61, while at $\eta =$ 0.65, where the lowest FM loss was found at 1.06 μm, a HOMER of ~200 is found; both high enough to make the fibers effectively single-

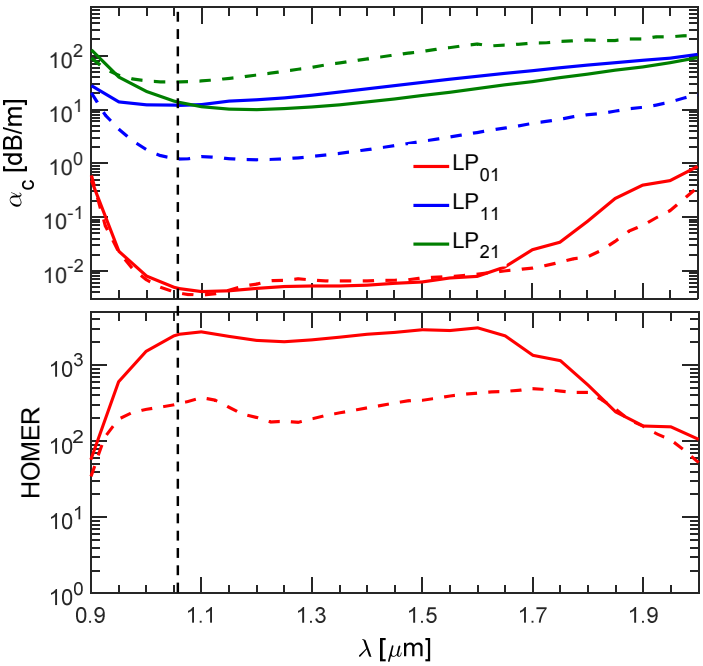

Figure 5.7. Spectral loss and HOMER curves (full lines: $\eta = 0.61$, dashed lines: $\eta = 0.65$). All structures have the same core diameter $D_c = 30$ μm and uniform silica strut thickness $t = 0.42$ μm.

moded. Remarkably, the $\eta = 0.61$ case is only slightly more losssy (5 dB/km) than the $\eta = 0.65$ case, so the loss penalty of maximizing HOMER is small. This again shows the design freedom of the anisotropic AR elements. The spectral loss and HOMER is shown in Fig. 5.7. The HOMER for the design with the lowest loss at 1.06 μm ($\eta = 0.65$) can be made in excess of 150 between $\lambda = 0.95 - 1.8$ μm, while keeping $\alpha_c < 15$ dB/km. Thus, this fiber has low-loss and is effectively single-moded over an octave of bandwidth. Interestingly, when the loss is increased slightly to maximize HOMER ($\eta = 0.61$), HOMER>1000 between $\lambda = 1.0 - 1.75$ μm with $\alpha_c < 15$ dB/km from $\lambda = 1.0 - 1.65$ μm. Figure 5.8(a) shows HOMER vs. wavelength, and confirms that the elliptical case outperforms the circular case in the entire wavelength regime $0.9 - 2$ μm.

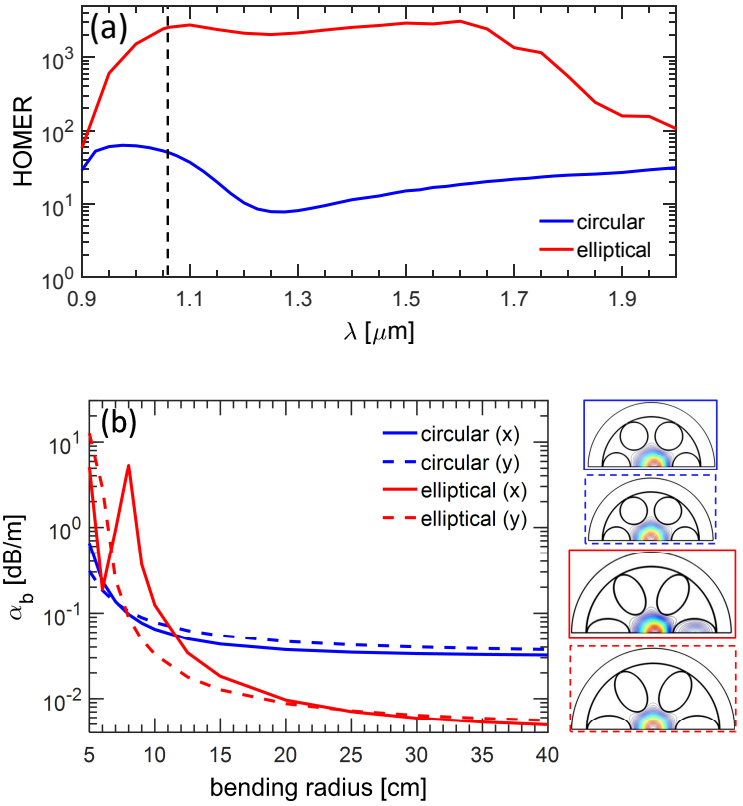

Figure 5.8. (a) Wavelength dependence of HOMER for circular ($r = 10.2$ μm) and elliptical ($\eta = 0.61$) AR tubes (b) bend loss vs. bend radius for 6 circular ($r = 10.2$ μm) and 6 elliptical ($\eta = 0.65$) AR tubes with $t = 0.42$ μm. The FM profiles are shown in the right hand side for a 10 cm bending radius. The color of the frame corresponds to the color of the line in the plot.

Figure 5.8(b) shows the bend loss (α_b) of the considered structures, calculated in both the x and y directions. The elliptical case shows an azimuthal variation of the bend loss, evidenced by a loss peak seen only in the x-direction for low bending radii due to increased core-cladding mode coupling. Therefore the circular case shows better bend loss performance for low bend radii for the 6-tube structure studied here.

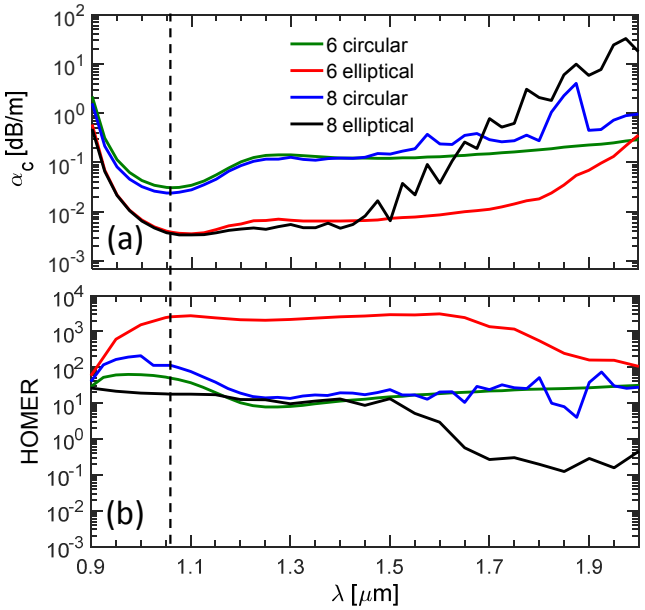

Figure 5.9. Leakage loss (a) and HOMER (b) as a function of wavelength for HC-AR fiber. All structures have the same core diameter $D_c = 30$ μm and uniform silica strut thickness $t = 0.42$ μm. All fiber designs are optimized at 1.06 μm to give minimum leakage loss.

5.5 Comparison with other design cases

In Fig. 5.9 we compare the loss performance and HOMER of 6 and 8 AR tubes. The calculated loss spectra in Fig. 5.9(a) shows that 6 and 8 AR tubes have similar loss performance in the 0.9-1.45 μm spectral regime; the 8 tube cases have slightly lower losses, but using 6 tubes gives much broader low-loss transmission window for both circular and elliptical cases. We also note that the 6 tube cases (both circular and elliptical) are very smooth while the 8 tube cases show spectral fluctuations vs. wavelength at the end of the transmission window. Similar fluctuations have previously been attributed to presence of nodes in the cladding[5], but clearly the origin here is different as there are no nodes.

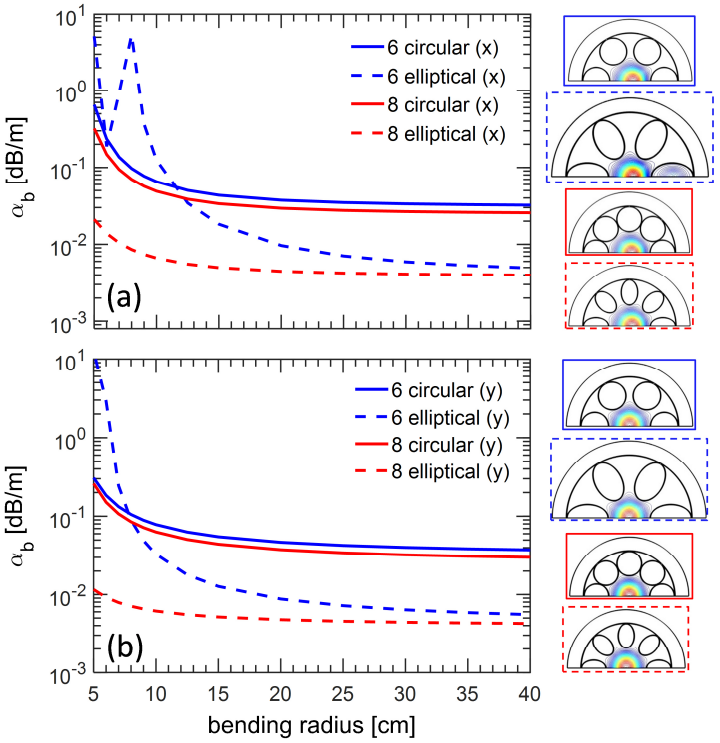

Figure 5.10. Bending loss vs. bending radius for different HC-AR fibers. All structures have the same core diameter $D_c = 30$ μm and uniform silica strut thickness $t = 0.42$ μm. The contour plots of the fundamental air-core mode distribution are shown in the right hand side for a 10 cm bending radius. The color of the frame corresponds to the color of the line in the plot.

The reason is instead found in the fact that for 8 tubes the core mode for longer wavelengths expands its mode field diameter so that it starts interacting weakly with cladding modes found at the outer capillary wall[13]; this leads to the observed fluctuations.Figure 5.9(b) shows the HOMER from which we see that 6 elliptical AR tubes have much higher HOMER compared to 8 AR tubes in the whole spectral regime.

Finally, Figs. 5.10 (a-b) show the bend loss performance in the *x*- and *y*- directions, respectively. For 8 AR tubes the elliptical case has better bend loss performance than the circular case. We believe this is because for the 8 tubes case, the AR tubes are smaller compared to the

6 tubes case. Therefore for small bend radius, 6 AR tubes have coupling between the core modes and tube modes due to the larger AR tubes whereas the coupling is reduced in 8 AR tubes because of the smaller AR tubes. Figure 5.10 also shows contour plots of the fundamental modes for 10 cm bending radius in which for 6 AR tubes there is a coupling between the core modes and tube modes whereas for 8 AR tubes there is no coupling between the core modes and tube modes. Therefore, choosing 6 or 8 tubes would have to be a compromise in terms of whether loss bandwidth, HOMER or bend loss is the most important feature.

We also considered introducing the ellipticity from the optimized circular design (10.2 μm AR tube radius), but instead of squeezing the ellipse azimuthally, it was elongated radially (i.e. extending the major axis) while keeping the core size fixed. This implies that the outer capillary expands its size as the ellipticity drops, which results in an improved loss performance compared to shrinking the minor axis (the case we have discussed so far). However, our calculations showed that the HOMER could not reach the same high values as found in Fig. 5.8(a). This implies that it is harder to reduce the phase-mismatch between the core HOMs and the cladding modes when extending the major axis.

5.6 Elliptical vs. circular tubes in the mid-IR regime

Due to the excellent loss and modal properties of the anisotropic hollow-core fiber in the near-IR regime, we have also investigated the loss property of anisotropic hollow-core fiber in the mid-IR regime and compared with the regular isotropic hollow-core fiber. We find that HC-AR fibers with node-free elliptical tubes offer lower leakage loss compared to HC-AR fibers with circular AR tubes.

Figure 5.11(a)-(b) shows the considered HC-AR fiber geometries in

which both designs are optimized at 2.94 μm. Design (a) is a typical isotropic HC-AR fiber in which AR tubes are non-touching each other. Design (b) is the proposed structure based on anisotropic AR tubes; here an ellipse is considered which is squeezed in the azimuthal direction. We choose a core diameter $D_c = 94$ μm as reported in [3], [4] and silica strut thickness $t = 1.26$ μm, which gives an anti-resonant first-order transmission window in the high-frequency mid-IR range (specifically around $\lambda = 2.94$ μm, the emission wavelength of Er:YAG lasers).

Figure 5.11(c) shows the loss spectrum of the two considered structures. In our calculations, the fraction of power in silica (FOPS) was calculated to estimate the effective material loss and then added to the leakage loss to obtain the total transmission loss. The material loss of silica was taken from [14]. To estimate the total transmission loss, surface scattering loss was not included due to the large core size and low power overlap in silica parts [3].

The broken blue line shows the calculated leakage loss of a "typical" optimized HC-AR fiber in which the leakage loss and transmission loss are ~35 dB/km and ~40 dB/km respectively at 2.94 μm, which is limited by coupling to the voids in the cladding [3]. The broken red lines show the leakage loss of the proposed HC-AR fiber in which anisotropic AR tubes were used to reduce the loss. The leakage loss and transmission loss are ~5dB/km and ~8dB/km respectively at 2.94 μm for the proposed structure. Thus, the anisotropic design has loss 5 times lower than the "typical" HC-AR fiber at 2.94 μm.

5.7 Predicted transmission band of HC-AR fiber

As mentioned in chapter 3, the guidance mechanism of our proposed design is based on the anti-resonant effect. Light is guided in silica struts at resonant wavelengths, whereas it is reflected back in the core

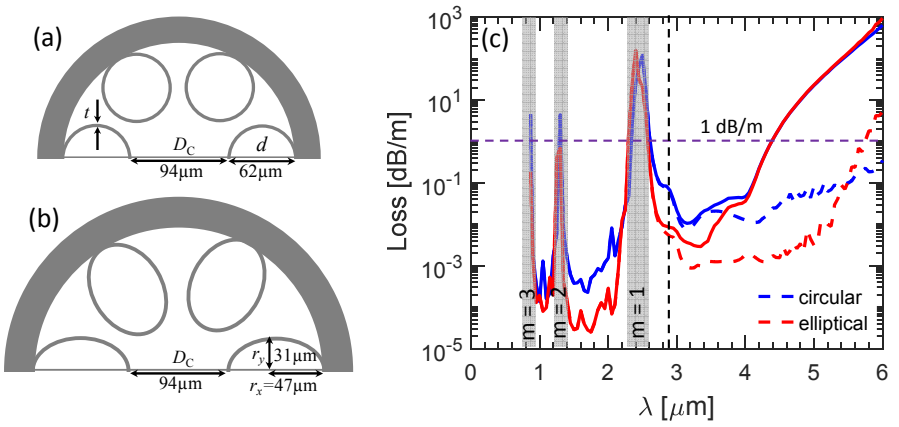

Figure 5.11. (a-b) Geometry of the considered HC-AR fibers. The structural parameters shown in the figure are those that optimized the leakage loss at 2.94 μm. The figures are scaled to indicate their relative size. (c) Calculated transmission bands in the near-IR to mid-IR. The broken lines indicate leakage loss while solid lines show the transmission loss where the material loss of silica is included. All structures have the same core diameter $D_c = 94$ μm and uniform silica strut thickness $t = 1.26$ μm.

at anti-resonant wavelengths. The transmission bands can be shifted by scaling the strut thickness of silica, since the cut-off wavelengths depend on the silica strut thickness [15].

We now consider the performance of our anisotropic fiber in the whole near-IR to mid-IR region of 0.9-6 μm for a fixed strut thickness of $t = 1.26$ μm. Our modelling results, which are given in Fig. 5.11(c), show that there are three low-loss transmission windows in this near to mid-IR wavelength regime. Remarkably it is possible to have below 1 dB/m total transmission loss over near to mid-IR regime. The proposed design shows better loss performance in the spectral regime 0.9-4.0 μm. Identical transmission loss performances were observed beyond 4 μm for the 2 designs because the loss is dominated by material loss, despite the low power fraction in silica. The positions of the transmission

bands are accurately predicted by Eq. (3.1).For example, for a modal order of $m = 2$ and strut thickness $t = 1.26$ µm, Eq. (3.1) predicts a cut-off wavelength around 1.32 μm, which is in excellent agreement with the 1.32 μm observed in Fig. 5.11(c).

The power overlap in silica parts play vital role for the performance of the HC- AR fiber in the mid-IR applications as the material attenuation of silica is very high in the mid-IR [3]. Figure 5.12 shows the FOPS as a function of wavelength in the near-IR to mid-IR spectral regime. In the mid-IR, we find the minimum power overlap in silica parts as low as 4×10^{-5}. We also find that ~99.99% of light is guided in the central hollow-core region. Due to the low power overlap in silica parts the proposed fiber design could be used to handle high optical power in the mid-IR.

5.8 Transmission and loss measurement of HC-AR fibers

In this section, we will discuss the loss measurement of various HC-AR fibers and compare the measured loss with ideal structures. The HC-AR fibers are fabricated at the Microstructured Fibers and Devices Group, CREOL, University of Central Florida, USA. The transmission and loss measurements were also performed at CREOL.

5.8.1 Node-free 7 rings HC-AR fibers

Figure 5.13(a) shows the scanning electron microscope (SEM) image of the fabricated HC-AR fiber and its ideal structure is shown in Fig. 5.13(b). Seven node-free inner tubes were chosen as this configuration

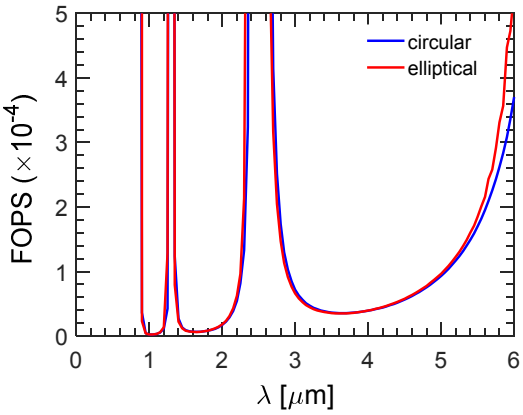

Figure 5.12. Calculated fraction of power in silica (FOPS) in the near-IR to mid-IR. The blue lines indicate FOPS for circular design while red lines show the FOPS for elliptical. All structures have the same core diameter D_c = 94 μm and uniform silica strut thickness t = 1.26 μm.

because it was found to be optimal for low loss and higher-order mode suppression [3]. The fiber core diameter was 33 μm and the average inner capillary diameter 16.7 μm. The average core wall thickness was 270 nm, aiming at distinct transmission bands in the UV and near-IR through the relation shown in Eq. (3.1). Figure 5.13(c) shows the measured transmission spectrum for a 5 m long HC-AR fiber. The transmission spectrum was measured by using a broadband source (NKT Photonics SuperK) via butt coupling with a single mode fiber at the input end of the HC-AR fiber. The transmission spectrum shows a resonance at around 560 nm and comes in good agreement with the relation reported above.

The propagation loss were measured using cut-back method. The measurements were permofmed using a supercontinuum source and an optical spectrum analyzer (OSA). The HC-AR fiber was butt-coupled through a single-mode fiber (SMF) and excited with the light source. The coupling loss between the fibers were relatively loss. In order to optimize the alignment, the output of the HCF was imaged on a charge-coupled device (CCD). The output light from the fiber was then

butt-coupled to the collection fiber (105/125) and connected to the OSA.

Figure 5.13(d) shows the mesured propagation loss of the fabricated HC-AR fiber (black line) and ideal fiber (red line, simuated using a finite-element method). The measured low-loss transmission window was from 300-550 nm and 580-1700 nm (more than one octave). The differences between the fabricated and simulated fiber can be attributed to the structural imperfections, where the capillary tubes do not have the optimal sizes and positions, combined with the fact that the numerical model does not take into account the significant scattering loss pronounced in the UV.

Finally, we numerically investigate the single-mode operation of the fiber. Fig. 5.13(e) shows that the loss of the higher-order-modes (HOMs) is higher compared to the fundamental modes (FM) due to the strong coupling between the core-guided HOMs and cladding modes. Figure 5.13(f) shows that the higher-order mode extinction ratio (HOMER) [4] is ~100 in the entire wavelength range, which indicates and confirms the single-mode operation of the fiber. The mode filed profiles of first 3 core guided modes are shown in Fig 5.14. Thus, the fabricated HC-AR fiber should have a high HOM suppression and we aim to confirm this experimentally in future.

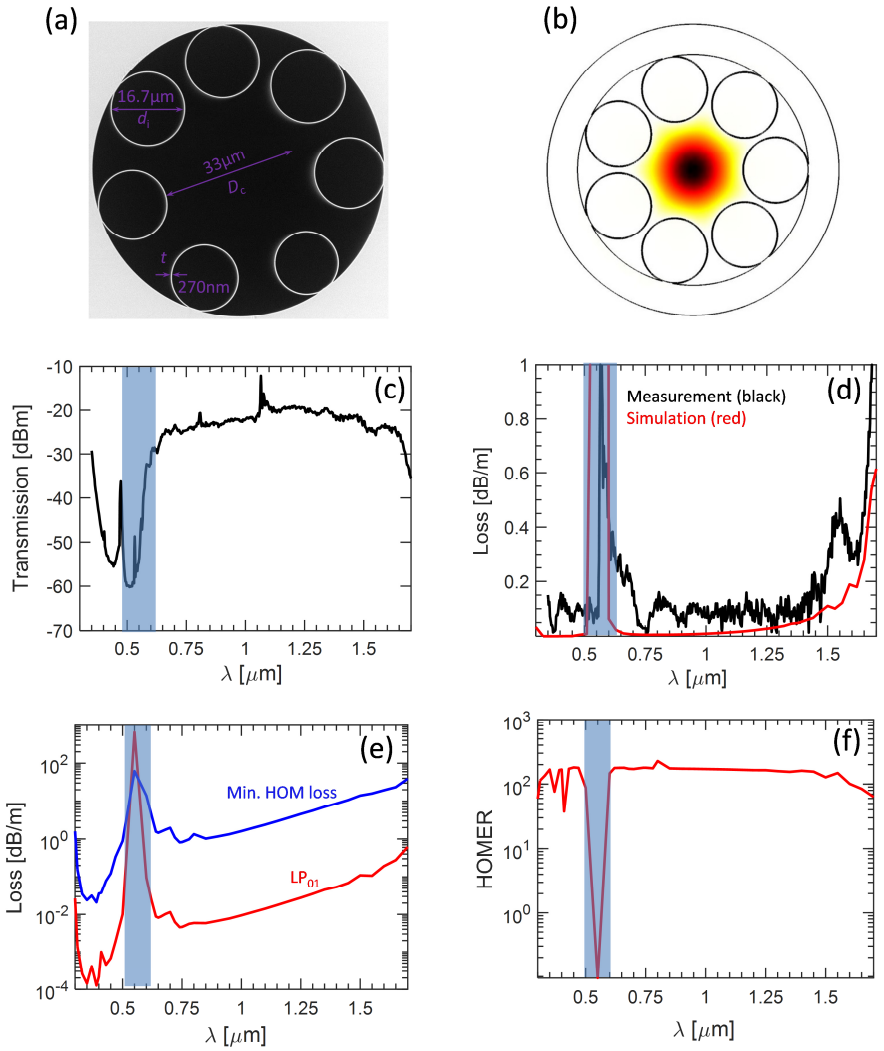

Figure 5.13. (a) SEM of the fabricated HC-AR fiber having core diameter $D_c = 33\ \mu$m , capillary diameter $D_i = 16.7\ \mu$m , and wall thickness $t = 270\ n$m (b) Cross-section of the simulated ideal HC-AR fiber along with the calculated fundamental mode intensity profile at 400 nm, (c) transmission spectrum of the fabricated HC-AR fiber, (c) loss comparison between the simulation and experiment, (e) loss comparison between the fundamental mode (FM) and higher-order-modes (HOMs) of the simulated fiber, and (f) wavelength dependence of HOMER. *SEM courtesy: Dr. J. E. Antonio-Lopez.*

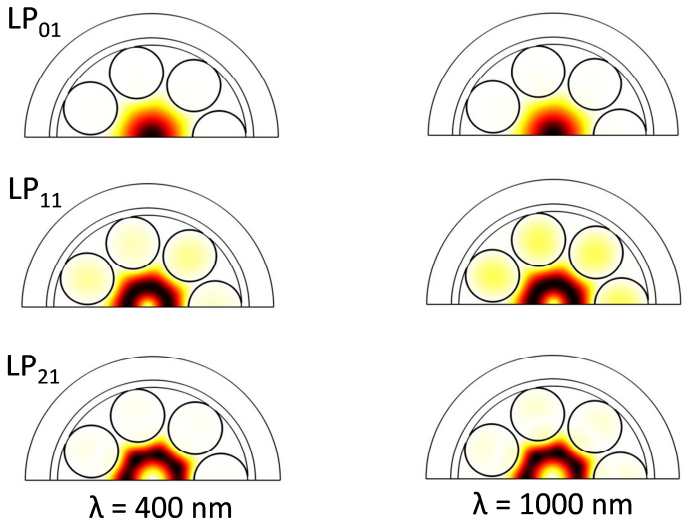

Figure 5.14. The mode profiles of the first 3 core guided modes (LP_{01}, LP_{11}, and LP_{21}) at wavelength of 400 nm (left) and 1000 nm (right).

5.8.2 Node-free nested 7 rings HC-AR fibers

Figure 5.15(a) shows a SEM image of a nested HC-AR fiber whereas Fig. 5.15(b) shows the cross-section of the simulated fiber. The fiber has an outer diameter of 124 μm, a core diameter of 33 μm and an average core wall thickness of ~780 nm ±50 nm. The average wall thickness of the inner capillaries is ~749 nm ±50 nm. The average diameter of the larger cladding capillaries is ~13.3 μm, while the average diameter of the inner tubes is ~3.3 μm. Figure 5.16(a) shows the measured transmission spectrum for a 2 m long nested AR-HCF along with the near field mode profile obtained at 1064 nm.

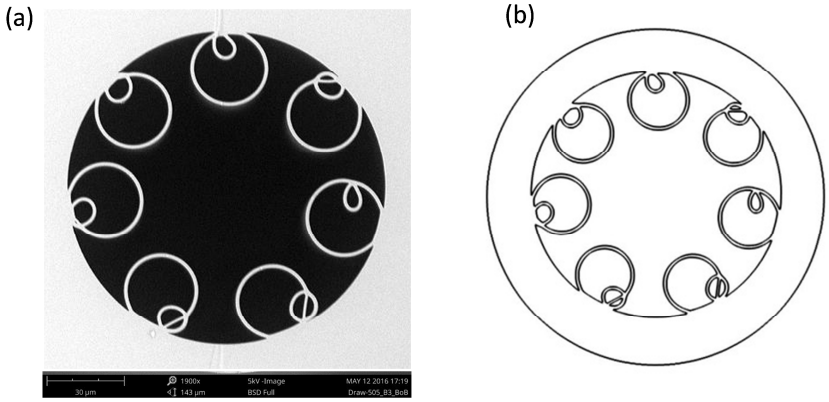

Figure 5.15. (a) SEM image of the fabricated HC-AR fiber having core diameter 33 μm , larger capillary diameter 13.3 μm , inner capillary diameter 13.3 μm, and average wall thickness of the inner tubes and original tubes is 749 ± 50 nm and 780 ± 50 nm respectively, (b) cross-section of the simulated fiber. *SEM courtesy: Dr. J. E. Antonio-Lopez.*

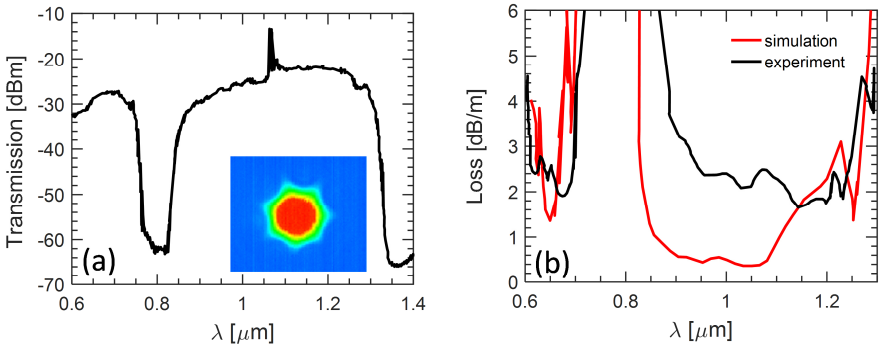

Figure 5.16. (a) Transmission and (b) loss spectra of nested HC-AR fiber. Inset of (a) shows the near-filed profile obtained at 1064 nm.

The transmission spectrum shows two resonant wavelengths ~780 nm and ~1380 nm, which is in good agreement with the fiber's geometry. A propagation loss of ~2 dB/m was measured at 1100 nm. The mode profile image presented in Fig. 5.16(a) clearly shows that even for very short fiber lengths and a not optimized excitation, this fiber supports robust single-mode operation.

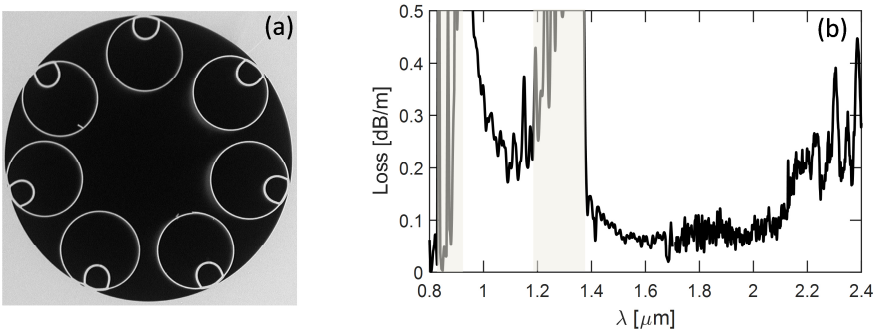

Figure 5.17. (a) SEM of the fabricated HC-AR fiber having core diameter 37.6 μm, larger capillary diameter 22.4 μm, inner capillary diameter 5.85 μm, and average wall thickness of the inner tubes and original tubes is 630 ± 50 nm and 363 ± 50 nm respectively, (b) measured loss spectra. The gray bars indicate high loss regions. *SEM courtesy: Dr. J. E. Antonio-Lopez.*

In order to better understand the experimental results, an accurate model of the actual fiber was obtained from the SEM image presented in Fig. 5.15(b) using image processing tools. Figure 5.16(b) shows remarkable agreement between themeasured loss (black line) and the calculated confinement loss (red line) of the nested AR-HCF.

An improved nested HC-AR fiber is shown in Fig. 5.17(a) which has a core diameter 37.6 μm, larger capillary diameter 22.4 μm, inner capillary diameter 5.85 μm, and average wall thickness of the inner tubes and original tubes is 630 ± 50 nm and 363 ± 50 nm respectively. The measured propagation loss is shown in Fig. 5.17(b). The fiber has broad transmission window from 900-2400 nm with resonance window at ~1320 nm which agrees well with Eq. (3.1). The minimum loss ~25 dB/km was measured at ~1700 nm.

5.9 Conclusion

In conclusion, a novel hollow-core anti-resonant fiber design has been proposed, in which the anti-resonant elements in the cladding are ani-

sotropic in shape, in contrast to the conventional isotropic circular shape. The anisotropic shape has improved performance because it simultaneously offers: (a) strong negative curvature in the core, (b) node-free (non-touching) anti-resonant elements, and (c) larger distance from the core to the outer capillary for a given core curvature. This gives a design degree-of-freedom essential for enhancing the performance, e.g. by fixing the size of the core and outer capillary while tuning the ellipticity to minimize loss. The transmission and measured loss of HC-AR fibers show that the fibers have broad transmission window and low loss. These properties of HC-AR fibers make an ideal medium to study ultrafast nonlinear optics.

References

[1] F. Yu, W. J. Wadsworth, and J. C. Knight, "Low loss silica hollow core fibers for 3-4 μm spectral region," *Opt. Express*, vol. 20, no. 10, pp. 11153, 2012.

[2] W. Belardi and J. C. Knight, "Hollow antiresonant fibers with low bending loss," *Opt. Express*, vol. 22, no. 8, pp. 9514, 2014.

[3] W. Belardi and J. C. Knight, "Hollow antiresonant fibers with reduced attenuation," *Opt. Lett.*, vol. 39, no. 7, pp. 1853, 2014.

[4] M. S. Habib, O. Bang, and M. Bache, "Low-loss hollow-core silica fibers with adjacent nested anti-resonant tubes," *Opt. Express*, vol. 23, no. 13, pp. 17394, 2015.

[5] F. Poletti, "Nested antiresonant nodeless hollow core fiber," *Opt. Express*, vol. 22, no. 20, pp. 23807, 2014.

[6] A. F. Kosolapov *et al.*, "Demonstration of CO_2-laser power delivery through chalcogenide-glass fiber with negative-curvature hollow core," *Opt. Express*, vol. 19, no. 25, pp. 25723, 2011.

[7] A. N. Kolyadin, A. F. Kosolapov, A. D. Pryamikov, A. S. Biriukov, V. G. Plotnichenko, and E. M. Dianov, "Light transmission in negative curvature hollow core fiber in extremely high material loss region," *Opt. Express*, vol. 21, no. 8, pp. 9514, 2013.

[8] W. Belardi and J. C. Knight, "Effect of core boundary curvature on the confinement losses of hollow antiresonant fibers," *Opt. Express*, vol. 21, no. 19, pp. 21912, 2013.

[9] R. Guobin, W. Zhi, L. Shuqin, and J. Shuisheng, "Mode classification and degeneracy in photonic crystal fibers," *Opt. Express*, vol. 11, no. 11, pp. 1310, 2003.

[10] G. Humbert *et al.*, "Hollow core photonic crystal fibers for beam delivery," *Opt. Express*, vol. 12, no. 8, pp. 1477, 2004.

[11] P. Uebel *et al.*, "Broadband robustly single-mode hollow-core PCF by resonant filtering of higher-order modes," *Opt. Lett.*, vol. 41, no. 9, p. 1961, 2016.

[12] A. Hartung *et al.*, "Low-loss single-mode guidance in large-core antiresonant hollow-core fibers," *Opt. Lett.*, vol. 40, no. 14, pp. 3432,

2015.

[13] M. Michieletto, J. K. Lyngsø, C. Jakobsen, O. Bang, and T. T. Alkeskjold, "Hollow-core fibres for high power pulse delivery," *Opt. Express*, vol. 24, no. 7, pp. 7103, 2016.

[14] O. Humbach, H. Fabian, U. Grzesik, U. Haken, and W. Heitmann, "Analysis of OH absorption bands in synthetic silica," *J. Non. Cryst. Solids*, vol. 203, pp. 19, 1996.

[15] F. Couny, F. Benabid, P. J. Roberts, P. S. Light, and M. G. Raymer, "Generation and photonic guidance of multi-octave optical-frequency combs," *Science*, vol. 318, no. 5853, pp. 1118, 2007.

Chapter 6

Gas-filled hollow-core anti-resonant fibers

Hollow-core anti-resonant (HC-AR) fibers have numerous advantages such as wide transmission spectrum (VUV to mid-IR), low loss, high optical damage threshold, and low anomalous dispersion [1]–[3]. These unique features of HC-AR fibers allow us to study ultrafast nonlinear optics when the fiber is filled with noble gas. The dispersion and nonlinearity of the system can be changed by simply changing the pressure of the gas [4]–[7] and offers various interesting phenomena such as UV light generation [8], temporal soliton pulse compression [9], supercontinuum generation, soliton self-frequency blue-shifting [6], [10], and mid-IR dispersive wave generation [7].

In this chapter the group velocity dispersion (GVD) of HC-AR fiber for different noble gases has been discussed. It discusses various models to calculate GVD. Finally, soliton dynamics and UV light generation is also discussed.

6.1 GVD of gas-filled HC-AR fiber

The group velocity dispersion (GVD) of HC-AR fiber has two contributions when filled with noble gas, one arises from the anomalous dispersion of the empty waveguide and the other arises from the normal dispersion of the filling gas [11]. The GVD of HC-AR fiber can be modeled using well-known capillary based Marcatili and Schmeltzer model (MSM). The dispersion of HC-AR fiber closely follows the MSM from UV to beyond near-IR [7]. The effective mode index of HC-AR fiber using MSM can be expressed as [4], [5], [11], [12]

$$n_{mn}(\lambda, P, T) = \sqrt{n_{gas}^2(\lambda, P, T) - u_{mn}^2/k_0^2 R_c^2}, \tag{6.1}$$

where n_{gas} is effective refractive index of the filling gas which depends on pressure and temperature, k_0 is the wave vector in vacuum, R_c is the core radius, and $u_{mn}$is the n^{th} zero of the m^{th}-order Bessel function of the first kind, where $m = n = 1$ corresponds to the HE_{11} mode of the fiber [9].

The refractive index of the filling gas can be calculated using the Sellmeier equation[13]

$$n_{gas}^2(\lambda, P, T) = 1 + \frac{P}{P_0}.\frac{T_0}{T}\left[\frac{B_1\lambda^2}{\lambda^2 - C_1} + \frac{B_2\lambda^2}{\lambda^2 - C_2}\right]_{P_0, T_0}, \tag{6.2}$$

where λ is the wavelength in μm, P is the gas pressure, P_0 is the atmospheric pressure, T is the temperature, $T_0 = 273$ K, B_1, B_2, C_1, and C_2 are the Sellmeier coefficients. The value of Sellmeier coefficients for different noble gas at $P_0 = 1$ bar and $T_0 = 0^o$c is shown in Table 6.1 [13].

Table 6.1. Sellmeier coefficients at $\boldsymbol{P_0} = 1$ bar and $\boldsymbol{T_0} = \boldsymbol{0^o c}$

Gas	$B_1 \times 10^{-8}$	$C_1 \times 10^{-6}$	$B_2 \times 10^{-8}$	$C_2 \times 10^{-3}$
He	4977.77	28.54	1856.94	7.760
Ne	9154.48	656.97	4018.63	5.728
Ar	20332.29	206.12	34458.31	8.066
Kr	26102.88	2.01	56946.82	10.043
Xe	103701.61	12750	31228.61	0.561

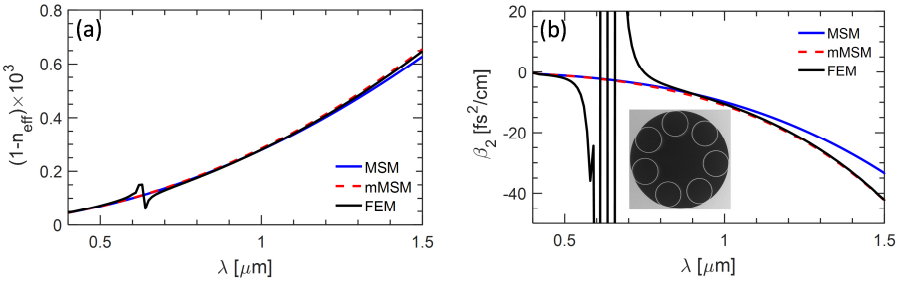

Figure 6.1. Comparison of (a) effective refractive index and (b) group velocity dispersion (β_2) calculated using MSM (blue), mMSM (broken red), and FEM (black) for an HC-AR evacuated fiber having core radius of 30 μm and silica wall thickness of 300 nm. The FEM calculations are in good agreement with MSM and mMSM except in the resonance region ($\sim$ 630 nm). The MSM shows discrepancy in the longer wavelength regime whereas mMSM is well agreed with the FEM simulations. Inset of (b) shows the SEM of the fiber used in this simulation.

Figure 6.1(a) and 6.1(b) shows the wavelength dependence of (1-n_{eff}) and GVD of an evacuated HC-AR fiber. The fiber has a core dimeter of 30 μm and silica wall thickness of 300 nm. It can be seen from Fig. 6.1(a) and 6.1(b) that MSM closely follows the FEM calculation of HC-AR fiber. However, the MSM starts deviates from the FEM simulations at longer wavelength regime. A modified version of MSM (mMSM) has been proposed by Finger *et al.* [11] where wavelength dependence of core radius is introduced. Figure 6.1(a) and 6.1(b) shows that the mMSM is well agreed with the FEM simulations in the longer wavelength regimes. The wavelength dependence core radius is given by [7], [11]

$$R(\lambda) = \frac{R_c}{1 + s\lambda^2/R_c t} \tag{6.3}$$

where s = 0.047 is a dimensionless empirical parameter.

When the HC-AR fiber is filled with noble gas, the anomalous dispersion of HC-AR fiber and normal dispersion of the filling gas counterbalance each other. Therefore, the GVD can be tuned over the entire

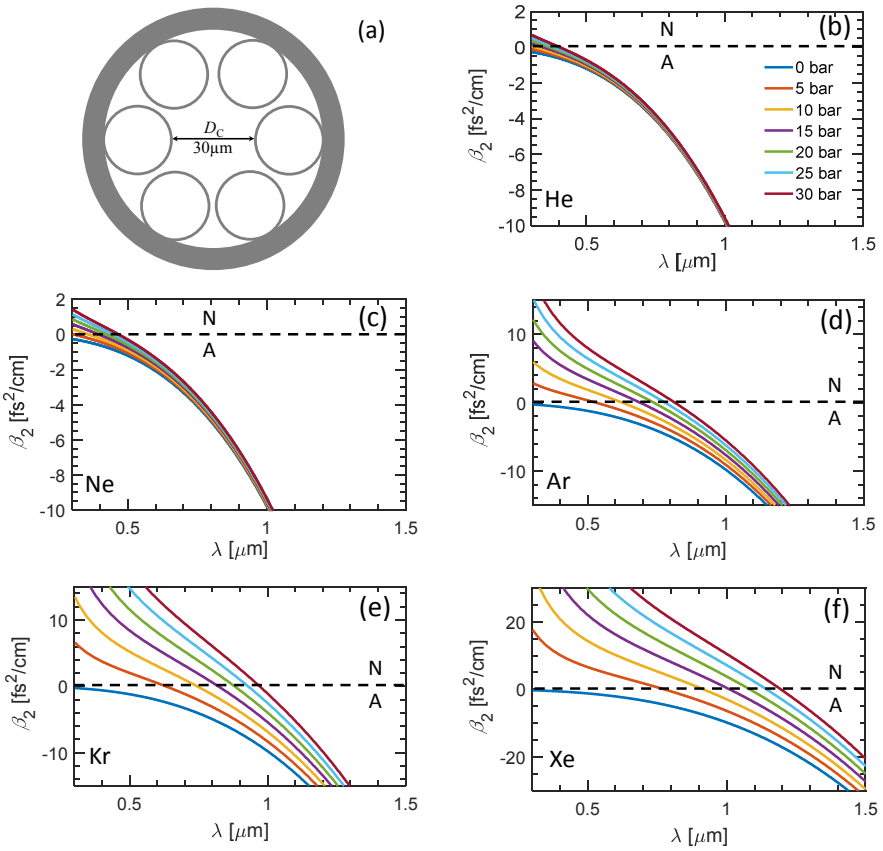

Figure 6.2. Pressure dependence GVD of various noble gases with an idealized HC-AR fiber having core diameter of 30 μm. The calculations are performed using mMSM. N: Normal dispersion regime, A: Anomalous dispersion regime.

wavelength range by simply changing the pressure of the filling gas. Figure 6.2 shows the pressure dependence GVD of various noble gases with an idealized HC-AR fiber having core diameter of 30 μm. It can be seen from Fig. 6.2 that when the fiber is evacuated it has anomalous dispersion in the entire wavelength regime. By changing the pressure of the gas, the GVD can be changed over a wide range. The zero-dispersion wavelength (ZDW) can also be tuned over a wide wavelength range. As an example for Ar gas, the ZDW can be tuned from

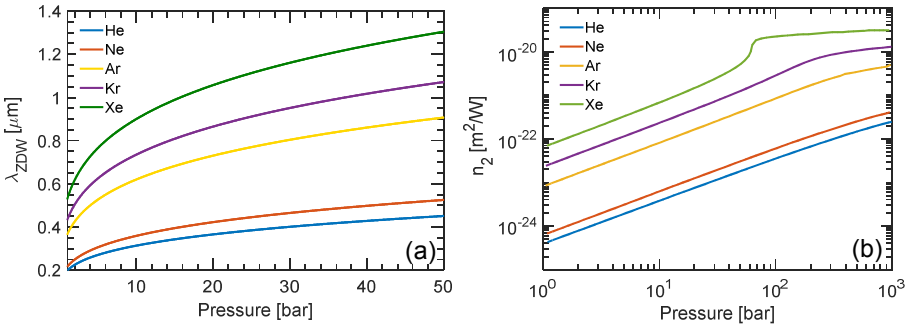

Figure 6.3. Pressure dependence of (a) ZDW and (b) nonlinear refractive index n_2 for different noble gases with an idealized HC-AR fiber having core diameter of 30 μm.

UV to near-IR by changing the pressure from 5 bar to 30 bar which is shown in Fig. 6.2(d). Importantly, the GVD is low and weakly anomalous over a wide range which allows to study soliton dynamics. Figure 6.3 shows the pressure dependence of ZDW and nonlinear refractive index for different noble gases. The ZDW can be tuned over a wide wavelength range and can be made far away from the pump wave (i.e. pump wavelength 1060 nm) for low pressure case. Helium (He) has lower ZDW whereas Xenon (Xe) has higher ZDW compared to other noble gases. The value of ZDW for a 30 μm core diameter HC-AR fiber for 10 bar He is ~250 nm, whereas ZDW for 10 bar Xe is ~950 nm.

6.2 Nonlinearity and energy handling of gas-filled HC-AR fiber

The nonlinearity can also be changed by changing the pressure of the gas. Figure 6.3(b) shows the nonlinear refractive index as a function of pressure. The nonlinear refractive index is calculated as in [9], [14], [15]. For noble gases, gas nonlinearity scales linearly with gas density, or with pressure at constant temperature [9], [14].

The unique feature of the HC-AR fiber is that ~99.99% of light can be guided in the core region whereas only a fraction of light ~0.01% overlaps with the silica parts over the entire wavelength range (except around the resonance wavelength) [1], [9], [16]. The results are shown in Fig. 5.12. Therefore, the nonlinearity in the system is due to the gas inside the fiber. Raman scattering can be neglected in a noble gas-filled HC-AR fiber due to very low power overlap with the silica parts of the fiber [9]. However, Raman-soliton dynamic can be studied for molecular gases such as N_2 or SF_6 [9].

Owing to low power overlap to the silica parts the optical damage thresholds of HC-AR fibers are much higher than in silica-core fibers [9]. The power overlap in the silica parts increases at resonance wavelengths where coupling between the core modes and cladding modes occur [1]. Due to the increased power overlap at the resonance wavelengths, optical damage might occur. However, the resonance wavelength can be shifted far from the operating wavelength by suitably choosing the silica strut thickness [9].

6.3 FEM vs. capillary model

Figure 6.4 shows a comparison between FEM and capillary model based mMSM on the spectral and temporal evolution in a 20 cm HC-AR fiber filled with 5 bar Ar pumped in the anomalous dispersion regime at 800 nm with 30 fs, 1 μJ pulse. The pulse propagation was calculated using unidirectional pulse propagation equation (see Eq. 2.26). It can be seen from Fig. 6.4 that a very good agreement is found between FEM and mMSM. However, a minor dissimilarity is found ~380 nm in which fiber resonance occurs due to the coupling between the core modes and cladding modes. The fiber resonance ~380 nm corresponds to the silica wall thickness 180 nm which is far away from the pump wavelength.

6.4 Soliton dynamic and UV light generation in gas-filled HC-AR fiber

Figure 6.4 shows that initially the pulse propagation is dominated by the interplay between anomalous dispersion and self-focusing self-phase modulation (SPM), leading to strong soliton self-compression down to sub-single cycle duration of 2 fs after 12 cm. The simulation parameters give soliton number 4.3. At the maximum temporal compression point, maximum spectral broadening occurs (see Fig. 6.4(a-c)) resulting in a strong dispersive wave (DW) generation ~217 nm. This DW generation is due to the strong soliton self-pulse compression of the input pulse which produces a broad spectrum in the frequency domain that overlaps with resonant dispersive frequencies [9].

The frequency of the dispersive wave can be obtained by a simple phase-matching condition. The phase-matching condition requiring that the dispersive wave at frequency ω propagate with the same phase velocity as that of the soliton at the frequency ω_s. The frequency shift $\Omega = \omega - \omega_s$ can be determined by [17]

$$\beta_2 \Omega^2 + \frac{\beta_3}{3} \Omega^3 - \gamma P_s = 0, \tag{6.4}$$

where P_s is the soliton peak power and ω_s is the soliton central frequency. The only real solution of the above equation is [17]

$$\Omega \approx -\frac{3\beta_2}{\beta_3} + \frac{\gamma P_s \beta_3}{3\beta_2^2}. \tag{6.5}$$

The frequency shift Ω is positive, if the solitons propagate in the anomalous dispersion regime ($\beta_2 < 0$) and ($\beta_3 > 0$). Hence, DW is gen-

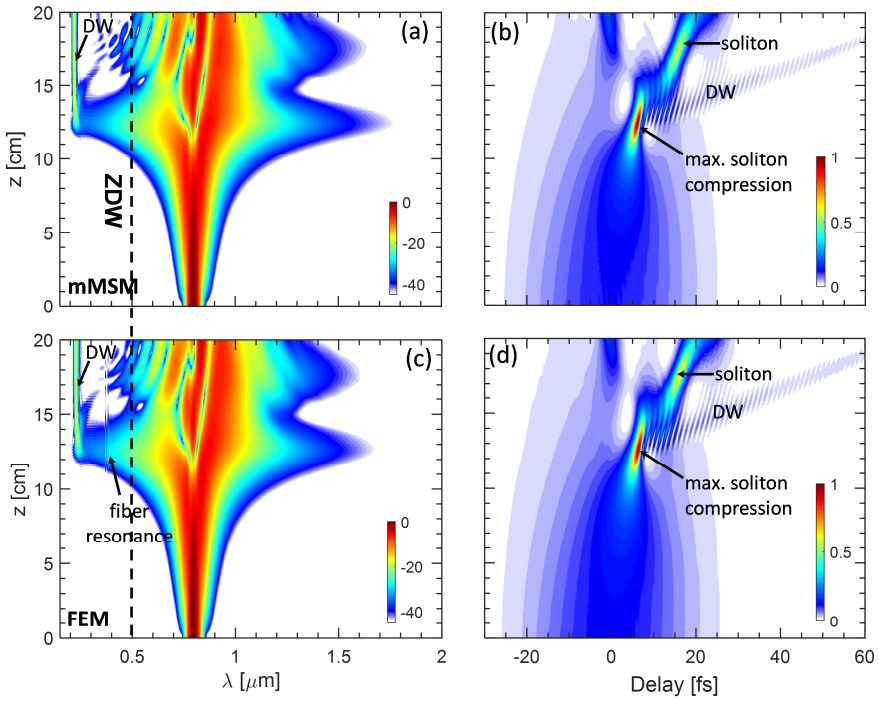

Figure 6.4. Spectral (a-c) and temporal evolution (b-c) of a 1 μJ, 30 fs long pulse in a 30 μm core diameter and silica wall thickness of 180nm Ar-filled HC-AR fiber under 5 bar using mMSM (top) and FEM (bottom). DW: dispersive wave.

erated at a higher frequency (a blue shift). The generation of DW can be tuned by simply changing the pressure of the gas [9].

Figure 6.5 shows the time-wavelength plots (cross-correlation frequency-resolved optical gating spectrograms) which allows us to better understand the pulse propagation phenomena at different propagation distances. The spectrograms are plotted using a 10 fs Gaussian gate pulse. At a distance z = 3 cm self-focusing SPM dominates giving a positive nonlinear chirp across the pulse (indicated by the dashed line through pulse center; in the wavelength vs. time spectrogram we remind that a negative slope corresponds to a positive chirp in this representation). In the time domain the pulse is compressed owing to the

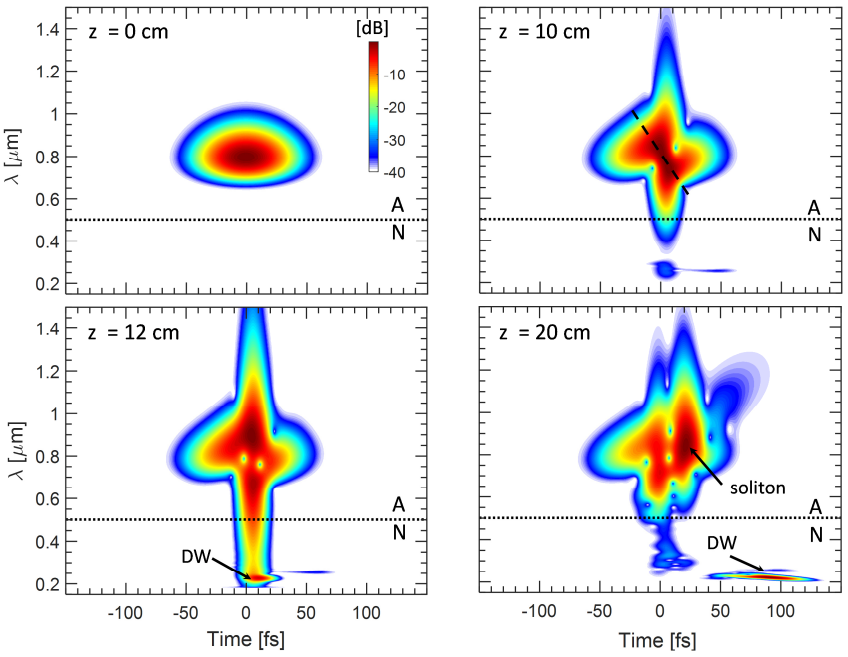

Figure 6.5. Cross-correlation frequency resolved optical gating spectrograms at selected distances for a 30 fs, 1μJ pulse injected in a 30 μm core HC-AR fiber filled with 5 bar Ar. In the spectrograms the horizontal dotted black lines indicates the ZDW. The spectrograms were calculated using a 10 fs Gaussian gate pulse. DW: dispersive wave. The spectrogram is represented by a dB scale from 0 dB to -40 dB. A: Anomalous dispersion, N: Normal dispersion.

soliton effect self-compression and the pulse experiences asymmetric in shape due to the self-steepening effect [5]. At the maximum temporal compression point (z = 12 cm), the pulse is compressed down to 2 fs resulting in a maximum spectral broadening in the frequency domain. The DW wave is emitted in the normal dispersion regime at ~217 nm. The emitted DW expands linearly in the time domain as it propagates inside the fiber which is shown at z = 20 cm.

6.5 Conclusion

In this chapter the properties of gas-filled hollow-core anti-resonant fiber is demonstrated. The unique features of HC-AR fiber and pressure tunable dispersion and nonlinearity of filling gas make it possible to explore different nonlinear effects such as soliton-effect pulse compression, UV light generation, and supercontinuum generation and so on.

References

[1] M. S. Habib, O. Bang, and M. Bache, "Low-loss hollow-core silica fibers with adjacent nested anti-resonant tubes," *Opt. Express*, vol. 23, no. 13, pp. 17394, 2015.

[2] F. Poletti, "Nested antiresonant nodeless hollow core fiber," *Opt. Express*, vol. 22, no. 20, pp. 23807, 2014.

[3] M. S. Habib, O. Bang, and M. Bache, "Low-loss Hollow-core Anti-Resonant Fibers with Semi-Circular Nested Tubes," *IEEE J. Sel. Top. Quantum Electron.*, vol. 22, no. 2, pp. 4402106, 2015.

[4] K. F. Mak, "Nonlinear optical effects in gas-filled hollow-core photonic-crystal fibers," *PhD Thesis*, 2014.

[5] P. Hölzer, "Nonlinear Fiber Optics in Gases and Dilute Plasmas," *PhD Thesis*, 2013.

[6] W. Chang *et al.*, "Influence of ionization on ultrafast gas-based nonlinear fiber optics," *Opt. Express*, vol. 19, no. 21, pp. 21018, 2011.

[7] D. Novoa, M. Cassataro, J. C. Travers, and P. S. J. Russell, "Photoionization-Induced Emission of Tunable Few-Cycle Midinfrared Dispersive Waves in Gas-Filled Hollow-Core Photonic Crystal Fibers," *Phys. Rev. Lett.*, vol. 115, no. 3, pp. 33901, 2015.

[8] N. Y. Joly *et al.*, "Bright spatially coherent wavelength-tunable deep-UV laser source using an Ar-filled photonic crystal fiber," *Phys. Rev. Lett.*, vol. 106, no. 20, pp. 203901, 2011.

[9] J. C. Travers, W. Chang, J. Nold, N. Y. Joly, and P. St. J. Russell, "Ultrafast nonlinear optics in gas-filled hollow-core photonic crystal fibers [Invited]," *J. Opt. Soc. Am. B*, vol. 28, no. 12, pp. A11, 2011.

[10] P. Hölzer *et al.*, "Femtosecond nonlinear fiber optics in the ionization regime," *Phys. Rev. Lett.*, vol. 107, no. 20, pp. 203901, 2011.

[11] M. A. Finger, N. Y. Joly, T. Weiss, and P. S. J. Russell, "Accuracy of the capillary approximation for gas-filled kagomé-style photonic crystal fibers," *Opt. Lett.*, vol. 39, no. 4, pp. 821, 2014.

[12] E. A. J. Marcatili and R. A. Schmeltzer, "Hollow Metallic and dielectric wave-guides for long distance optical transmission and lasers." Bell Syst. Tech. J., pp. 1783–1809, 1964.

[13] A. Börzsönyi, Z. Heiner, M. P. Kalashnikov, A. P. Kov'acs, and K. Osvay, "Dispersion measurement of inert gases and gas mixtures at 800 nm," *Appl. Opt.*, vol. 47, no. 27, pp. 4856, 2008.

[14] H. J. Lehmeier, W. Leupacher, and A. Penzkofer, "Nonresonant third order hyperpolarizability of rare gases and N2 determined by third harmonic generation," *Opt. Commun.*, vol. 56, no. 1, pp. 67, 1985.

[15] M. Azhar, "Tunable nonlinear fiber optics using dense noble gases,", *PhD Thesis* 2013.

[16] M. S. Habib, O. Bang, and M. Bache, "Low-loss single-mode hollow-core fiber with anisotropic anti-resonant elements," *Opt. Express*, vol. 24, no. 8, pp. 8429, 2016.

[17] G. Agrawal, "Nonlinear Fiber Optics, Academic Press (2006).

Chapter 7

Gas-filled hollow-core fiber in the ionization regime

The peak intensity of a laser pulse inside gas-filled hollow-core anti-resonant fiber can reach over 10^{14} W/cm^2. Such an intense laser pulse is enough to ionize noble gas and form a plasma without damaging the fiber [1]–[3] and creates free electron densities over N_e~10^{17} cm^{-3}. The generation of free electrons modifies the nonlinear pulse propagation equation. In this chapter, different ionization models and generation of free electron densities have been described. Finally, we will discuss combined action of Kerr and ionization on the nonlinear pulse propagation in the mid-IR.

7.1 Ionization models

To calculate the ionization rate of free electrons several ionization models have been established such as the Keldysh model [4], Perelomov, Popov and Terent'ev (PPT) model [5], and Ammosov, Delone, and Krainov (ADK) model [6]. The ionization rate model of a hydrogen-like ground state in a short-rate rate was first proposed by Keldysh. Perelomov, Popov and Terent'ev also proposed an ionization rate equation in which both multiphoton ionization and tunnel ionization was considered. The ionization rate can also be calculated by the Ammonsov-Delone-Krainov (ADK) model. This model is the simplest form of the PPT model resitricted in the tunneling regime.

7.1.1 Keldysh parameter

To classify different ionization regimes, Keldysh introduced a dimensionless parameter. In atomic units, the Keldysh parameter is expressed as [3], [7], [8]

$$\gamma = \frac{\omega}{F}\sqrt{2I_p} = \sqrt{\frac{I_p}{2U_p}}, \tag{7.1}$$

where ω is the angular frequency of laser field, F is the strength of the laser field, I_p is the ionization potential of an atom, and U_p is the ponderomotive potential. The ponderomotive potential is defined as the cycle average kinetic energy of an electron in the laser field which can be written as

$$U_p = \frac{F^2}{4w^2}. \tag{7.2}$$

The Keldysh parameter can also be defined as the ratio between the tunneling time (the time needed for an electron to cross the Coulomb barrier), and the during which the same barrier is lowered by the laser field which is expressed as

$$\gamma = \frac{2\pi\sqrt{2I_p}}{T_0 F} = \frac{t_{tun}}{T_0}. \tag{7.3}$$

Using Fig. 7.1 the barrier width can be written as

$$\Delta l = \frac{I_p}{F}. \tag{7.4}$$

To estimate the tunneling time, the electron velocity inside the barrier is assumed to be the same as that in the ground state. The tunneling time is expressed as

$$t_{tun} = \frac{\Delta l}{v_{gnd}} = \frac{I_p}{F v_{gnd}}, \tag{7.5}$$

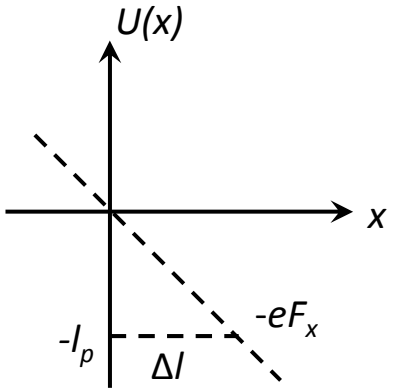

Figure 7.1. Potential barrier formed by the laser field. Redrawn after [9].

where Δl is the width of the barrier and v_{gnd} is the velocity of the electron in the ground state. The ionization potential, I_P is written as

$$I_p = \frac{1}{2} m_e v_{gr}^2. \tag{7.6}$$

The electron velocity in atomic unit is given by

$$v_{gr} = \sqrt{2I_p}. \tag{7.7}$$

From Eqs. (7.4), (7.5) and (7.6) the tunneling time can be expressed as

$$t_{tun} = \frac{\frac{1}{2}\sqrt{2I_p}}{F}. \tag{7.8}$$

The Keldysh parameter can also be expressed as

$$\gamma = \frac{t_{tun}}{T_0/2} = \frac{\sqrt{2I_p}}{T_0 F}. \tag{7.9}$$

The value of Keldysh parameter determines the state of ionizations regime of atoms in a laser field. When $\gamma \gg 1$, multiphoton ionization occurs, and tunnel ionization happens when $\gamma \ll 1$.

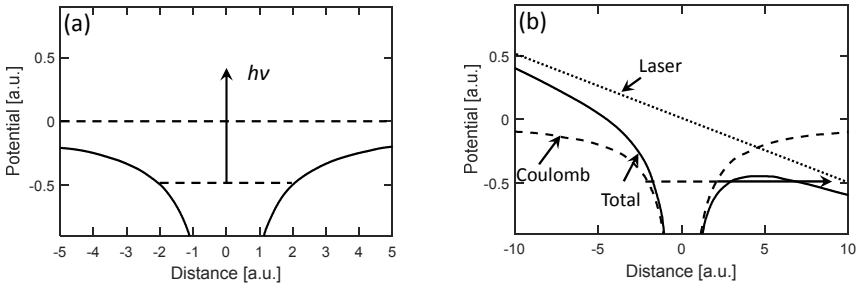

Figure 7.2. (a) Multi-photon ionization and (b) tunnel ionization. Redrawn after [9].

In the regime of multiphoton ionization, electrons are pulled out of the atom by absorptions of several photons, and in the tunneling regime, the electron leaves the atomic core by passing through the Coulomb barrier lowered by the laser field. The multiphoton and tunnel ionization process is shown in Fig. 7.2. In the following section we will discuss on the PPT model and ADK model.

7.1.2 Ionization rate equation of PPT model

The PPT model was derived for a short-range potential and includes the effect of the long-range Coulomb interaction through the first-order correction in the quasi-classical action, which does not consider any discrete binding states other than ground state. The ionization rate of PPT model can be written as [9]

$$W_{PPT} = \sum_{q \geq q_{thr}}^{\infty} w_q(F, w), \tag{7.10}$$

where $q_{thr} = (I_p + U_p)/\omega$ is the minimum number of photon required to ionize an electron through the multiphoton process or the ionization threshold. Assuming the electron is in the state, n, l, m, before the field arrives in which n is the principal quantum number, l is the orbital quantum number, and m is magnetic quantum number.

The rate to ionization by absorbing q photons of PPT model in atomic units can be expressed as [9]

$$w_q(F,w) = A_q(\omega,\gamma)|C_{n^*l^*}|^2 f(l,m) I_p \left(\frac{2F_0}{F}\right)^{2n*}, \tag{7.11}$$

where

$$A_q(\omega,\gamma) = e^{-(\alpha(q-v))} w_m\big(\sqrt{\beta(q-v)}\big),$$

$$v = \frac{I_p}{\omega}\left(1+\frac{1}{2\gamma^2}\right) = \frac{I_p+U_p}{\omega},$$

$$\alpha(\gamma) = 2\left(\sinh^{-1}\gamma - \frac{\gamma}{\sqrt{1+\gamma^2}}\right),$$

$$\beta(\gamma) = \frac{2\gamma}{\sqrt{1+\gamma^2}},$$

$$w_m(x) = \frac{x^{2|m|+1}}{2}\int_0^1 \frac{e^{-x^2 t|m|}}{\sqrt{1-t}}dt,$$

The ionization rate can be written as

$$\begin{aligned} w_{PPT}(F,\omega) = |C_{n^*l^*}|^2 f(l,m) I_p \left(\frac{2F_0}{F}\right)^{2n*-|m|-1} \left(\frac{1}{\sqrt{1+\gamma^2}}\right)^{-|m|-1} \\ \times \frac{4}{\sqrt{3\pi}}\frac{1}{|m|!}\frac{\gamma^2}{1+\gamma^2} e^{-\frac{2F_0}{3F}g(\gamma)} \sum\nolimits_{q\geq q_{thr}}^{\infty} A_q(\omega,\gamma), \end{aligned} \tag{7.12}$$

where $\left(\frac{2F_0}{F}\right)^{2n^*}$ is the correction of the long-rage Coulomb interaction given that the Coulomb field is expressed as $F_0 = (2I_p)^{\frac{3}{2}}$ and the Keldysh number is $\gamma = \omega(\frac{F_0^{\frac{1}{3}}}{F})$.

The effective principal quantum number $n^* = \frac{Z}{(2I_p)^{0.5}}$, and the effective orbital quantum number is $l^* = n^* – 1$. The three coefficients are

$$|C_{n^*l^*}|^2 = \frac{2^{2n^*}}{n^*\Gamma(n^*+l^*+1)\Gamma(n^*-l^*)},$$

$$f(l,m) = \frac{(2l+1)(l+|m|!)}{2^m|m|!\,(l-|m|!)},$$

$$g(\gamma) = \frac{3}{2\gamma}\left\{\left(1+\frac{1}{2\gamma^2}\sinh^{-1}(\gamma)-\frac{\sqrt{1+\gamma^2}}{2\gamma}\right)\right\},$$

The value of $\sum_{q\geq q_{thr}}^{\infty} A_q(\omega,\gamma)$ can be obtained approximated by setting the upper limit of the sum to $q_{max}-v = 10/\alpha(\gamma)$. For even larger values of q, the contribution to the sum can neglected because $e^{\alpha(q-v)}$is much smaller than that of the leading terms.

7.1.3 Ionization rate equation of ADK Model

Ammosov, Delone, and Kraivon (ADK) derived the expressions for the tunnel ionization of arbitrary complex atoms and atomic ions. The model is derived from the PPT model restricted to the tunnel ionization [3], [7]. The effective principal quantum number is $n^* = Z/\sqrt{2I_p}$ and the effective orbital quantum number is $l^* = n^* - 1$. In the tunneling regime, $\gamma \ll 1$, we have $\left(\frac{1}{\sqrt{1+\gamma^2}}\right)^{-|m|-1} \approx 1$, $\sum_{q\geq q_{thr}}^{\infty} A_q(\omega,\gamma) \approx 1$, and $g(\gamma) \approx 1$. The ionization rate can be written as[9]

$$w_{ADK}(F,\omega) = |C_{n^*l^*}|^2 f(l,m) I_p \left(\frac{2F_0}{F}\right)^{2n*-|m|-1} e^{-\frac{2F_0}{3F}}. \tag{7.13}$$

When $\gamma \gg 1$, the main difference between the PPT and ADK rate is caused by the $g(\gamma)$ because it is in the exponent of the PPT rate.

7.2 Free electron density calculation

The density of free electrons can be expressed as [3], [7], [10], [11]

$$\frac{\partial N_e}{\partial t} = W(E)(N_0 - N_e), \tag{7.14}$$

where $W(E)$ is the ionization rate, N_e is the free electron density and N_0 is the density is combined population of atoms and ions. In the calculation of free electron density the first ionization level is considered. The collisional excitation and electron recombination is also neglected [12]. Equation (7.14) can also be written as [13]

$$N_e(z,t) = N_0 \left[1 - exp\left(-\int_{-\infty}^{t} W\big(E(z,t')\big)dt'\right)\right]. \tag{7.15}$$

In can be seen from Eq. (7.15) that the free electron density and ionization rate are nonlinear function of the electric field [7]. The ionization fraction (N_e/N_0) as a function of time is shown in Fig. 7.3 in which most of the free electrons are generated across the intense portion of the pulse. The growth of the free electron density occurs across the pulse envelop as the pulse duration is much lower than the recombination time (the time needed to recombine the electrons to their parent ions)[3].

7.3 Nonlinear polarization due to ionization

In chapter 2 section (2.2.1), the pulse propagation equation is derived under the assumption that there is no free charge in the medium. However, this assumption is not valid when sufficient free electrons are generated inside hollow-core fiber filled with noble gas [3], [7]. Therefore, the effect of ionization needs to be included in the nonlinear pulse propagation equation.

Due to the movement of free electrons, a current will induce. The current density, J relates with the polarization which is expressed as

$$J(t) = \frac{\partial P}{\partial t}. \tag{7.16}$$

The polarization due to the free electrons can be written as

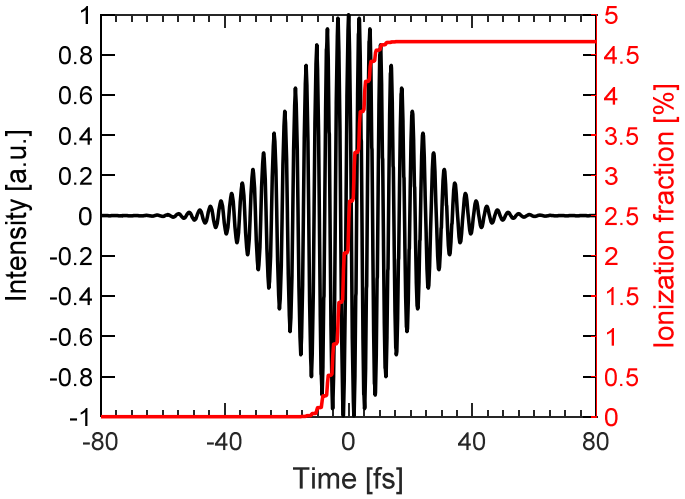

Figure 7.3. The intensity (left) and ionization fraction (right) as a function of time. The ionization fraction is calculated using a 30 fs Gaussian pulse with energy of 10 μJ, 30 μm hollow-core anti-resonant fiber filled with Kr having 10 bar pressure.

$$P_{elec} = ex(t)N_e, \tag{7.17}$$

where $x(t)$ is the distance from their parent nuclei [3].

From Eq. (7.16) current density J can be written as

$$J = \frac{\partial P_{elec}}{\partial t} = ex(t)\frac{\partial N_e}{\partial t} + eN_e\frac{\partial x(t)}{\partial t}. \tag{7.18}$$

In this picture, the electron is "born" on the outer side of the Coulomb barrier at a distance of $x_0(t) \approx Ip/eE(t)$ from the nucleus and with zero initial velocity $v_o = \partial x/\partial t \approx 0$ [7], [11].

As $\frac{\partial N_e}{\partial t} \neq 0$, $x(t)$ is substituted by $x_0(t)$ in the first term of the current [13], yielding

$$J = ex_0(t)\frac{\partial N_e}{\partial t} + eN_e\frac{\partial x(t)}{\partial t}. \tag{7.19}$$

The second time derivative of polarization can be written as

$$\frac{\partial^2 P_{elec}}{\partial t^2} = \frac{\partial J}{\partial t} = e\frac{\partial(x_0 \frac{\partial N_e}{\partial t})}{\partial t} + eN_e \frac{\partial^2 x(t)}{\partial t^2} + e\frac{\partial x(t)}{\partial t}\frac{\partial N_e}{\partial t}. \tag{7.20}$$

Assuming the initial velocity of an electron is $v_o = \partial x/\partial t \approx 0$, the expression for the second term is found as a solution to Newton's equation of motion

$$\frac{\partial^2 x(t)}{\partial t^2} = \frac{eE(t)}{m_e}. \tag{7.21}$$

The polarization can be expressed as [3], [7]

$$\begin{aligned} P_{elec}(z,t) = I_P \int_{-\infty}^{t} \frac{1}{E(z,t')} \frac{\partial N_e(t')}{\partial t'} dt' \\ + \frac{e^2}{m_e} \int_{-\infty}^{t'} \int_{-\infty}^{t''} N_e(z,t'') E(z,t'') dt'' dt'. \end{aligned} \tag{7.22}$$

The first term in Eq. (7.22) accounts for the loss of pulse energy due to the ionization process. The second term presents the temporal variation of the real and imaginary parts of the refractive index due to the presence of free electrons [14].

The refractive index of the plasma can be written as [3]

$$n_{plasma} = \sqrt{1 - \frac{N_e e^2}{\epsilon_0 m_e \omega^2}} = \sqrt{1 - \frac{\omega_p^2}{\omega^2}}, \tag{7.23}$$

Where ω_p is the plasma frequency which is expressed as [15]

$$\omega_p = \sqrt{\frac{N_e e^2}{m_e \epsilon_0}}. \tag{7.24}$$

Equation (7.23) shows that if the generation of free electrons increase, the refractive index of the plasma will be decreased which is opposite to the Kerr effect. It can be seen from Fig. 7.3 that the generation of free electrons increases across the most intense portion of the pulse envelope. Therefore, the variation of the refractive index will be in one direction across the pulse [3]. Due to these phenomena, we will see in the later section that the pulse broadening will occur towards the blue also

named as *soliton self-frequency blue shift* which is asymmetric in shape [1], [3], [7], [8], [14]. The phenomena can be considered as the opposite to the Raman self- frequency red shift.

7.4 Soliton-plasma dynamics in the mid-IR

In this section, the soliton-plasma nonlinear dynamics in a mid-IR pumped Xe-filled HC fiber based on the so-called anti-resonant (AR) effect has been investigated. We find a soliton dynamics scenario where multiple soliton self-compression stages are observed, which we explain as a direct consequence having distinct propagation stages with either the self-focusing or the self-defocusing nonlinearity dominates. This happens for certain system parameter ranges, mainly involving moderate gas pressure and input pulse intensities.

HC-AR fibers provide relatively low-loss transmission, low light-glass overlap, and broadband guidance [16]–[19]. However, one of the main striking features of HC-AR fibers is that ~99.99% light can be guided inside the central hollow-core region, which significantly enhances the damage threshold levels [1], [19]. Another advantage of using gas-filled HC fibers is that both the dispersion and nonlinearity can be tuned by simply changing the pressure of the gas [1], [20], [21] while at the same time providing extremely wide transparency ranges. Recently, silica HC-AR fibers suitable for the mid-IR were demonstrated with a propagation loss of <0.1 dB/m in the wavelength range 3-4 μm [16], [17].

7.4.1 GVD and loss calculations

The mid-IR properties of silica HC-AR fibers filled with the noble gass xenon (Xe) has been analysed. We pump in the anomalous dispersion regime at 3.0 μm and study the nonlocal soliton-plasma dynamics in a

recently fabricated HC-AR fiber (see Fig. 7.4 (c)). The fiber has a core 43.7 μm core diameter and 0.74 μm silica wall thickness. The wall thickess was chosen 0.74 μm so that it has first order resonance far away from the pump wavelength. This wall thickness introduces the first high loss band (resonance) at around 1.55 μm which is far away from the pump wavelength, and was chosen to give low loss at the 3.0 μm pump wavelength. The resonance bands are indicated as $m = 1,2,3$ in Fig. 7.4(b).

Inspired by recent works [1], [8], [20], the group-velocity dispersion (GVD) was calculated using the modified version of Marcatili and Schmeltzer's model (mMSM)[20]. The mMSM model is described in chapter 6 (see section 6.1). In this work, the fundamental mode (LP_{01}) is considered only and we ignore any polarization effects. The GVD and leakage loss were also calculated using the finite-element method (FEM). The mesh size and perfectly-matched layer (PML) parameters were carefully optimized to accurately model the leakage loss. A maximum mesh size of $\lambda/6$ and $\lambda/4$ was used in silica and air regions, respectively [18], [22]. The power overlap in the silica walls was used to estimate the effective material loss and then added to the leakage loss to obtain the final propagation loss [18] which is shown in Fig. 7.4 (b).

Figure 7.4(a) shows the GVD of 43.7 μm HC-AR fiber filled with 1.2 bar Xe, calculated using capillary based mMSM (red line) and FEM (blue line). The FEM calculated propagation loss is shown in Fig. 7.4(b). The FEM calculations are able to track the loss and the rapidly oscillating GVD in the high-loss resonance bands (gray shaded regions, with m being the resonance band index), which are introduced by the resonant coupling between the core and cladding modes.

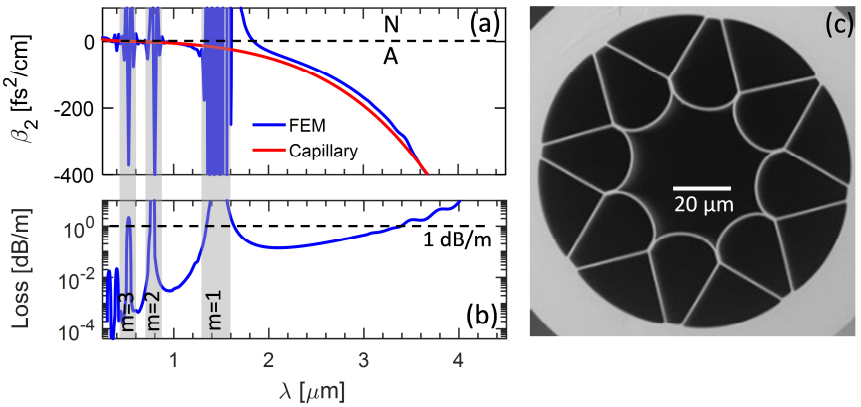

Figure 7.4. Numerically calculated (a) GVD vs. wavelength using capillary model (red curve) and FEM (blue curve) (b) propagation loss of an HC-AR fiber filled with 1.2 bar Xe, and (c) SEM image of the fabricated fiber used in this simulation. The gray bars indicate high loss regions. The fiber has 43.7 μm core diameter and 740 nm wall thickness. A: Anomalous dispersion, N: Normal dispersion.

In the resonance bands the GVD found by the mMSM stays smooth and continuous, while outside the bands it follows the GVD found by FEM quite well. However, we found discrepancy in the GVD calculations between mMSM and FEM in the longer wavelength regimes. The FEM results predict a propagation loss as low as ~0.45 dB/m at 3.0 μm.

7.4.2 Pulse propagation in ionization regime

The optical pulse propagation in the gas-filled HC-AR fiber was studied using the unidirectional pulse propagation equation [1], [2], [11], [14]

$$\frac{\partial E}{\partial z} = i\left(\beta(\omega) - \frac{\omega}{v_g}\right)E(z,\omega) - \frac{\alpha(\omega)}{2}E(z,\omega) + \frac{i\omega^2}{2c^2\epsilon_0\beta(\omega)}\mathcal{F}[P_{NL}(z,t)] \tag{7.25}$$

where z is the propagation direction, t is the time in the reference frame moving with the pump group velocity v_g, $E(z,\omega)$ is the electric field in the frequency domain, ω is the angular frequency, $\alpha(\omega)$ is the propagation loss, c is the speed of light in vacuum, $\beta(\omega)$ is the propagation constant, $\mathcal{F}$ denotes the Fourier transform, and $P_{NL}(z,t)$ is the nonlinear polarization. The nonlinear polarization $P_{NL}(z,t)$ has two terms through this relation [1], [2], [14]$P_{NL}(z,t) = \epsilon_0\chi^{(3)}E^3 + P_{ion}(z,t)$. The first term describes the Kerr effect, where ε_0 and $\chi^{(3)}$ are the vacuum permittivity and third-order nonlinear susceptibility, respectively, while the second term is the ionization effect shown in Eq. (7.22).

The nonlinear refractive index (n_2) of Xe at 1.2 bar was taken to be 8×10^{-23} m^2/W and considered wavelength independent as it does not vary significantly with wavelength [15]. This is also confirmed in a recent experiment [23]. We neglect the Raman contribution due to the low power overlap with the silica parts ($<<1\%$) and most of the light is guided in the core [21].

The main point is that the dynamics of $N_e(z,t)$ depends on whether multi-photon or tunnel ionization is occurring. In our case, the peak intensity inside the HC-AR fiber reaches around 70 TW/cm^2. This should be in the range where tunnel ionization dominates over the multi-photon ionization, in particular because in the mid-IR the photon energy is low and thus multi-photon ionization has a high intensity onset threshold. Therefore, to calculate the free electron density, it is enough to consider quasi-static tunneling ionization based on ADK model. We also used the PPT [1] model, which includes multi-photon ionization as well, and found essentially the same results. Finally, the Keldysh parameter (γ) was checked to be less than unity. We therefore conclude that tunnel ionization dominates.

The optical pulse propagation was modelled using either using no loss and the GVD from mMSM (see Fig. 7.5(a-b)) or using the full FEM loss and GVD profile or (see Fig. 7.5(c-d)). We mainly focus on the mMSM as it allows to better understanding the fundamental dynamics behind the observed multi-compression stages without the inter-

ference oscillations due to the resonances of the FEM. We emphasize that the two models qualitatively give similar results, as evidenced in the direct comparison between the two models in Fig. 7.5.

The spectral and temporal soliton-plasma dynamics in a 25 cm HC-AR fiber having core diameter 43.7 μm filled with 1.2 bar Xe pumped in the anomalous dispersion regime at 3.0 μm with 100 fs, 20 μJ Gaussian pulses is shown in Fig. 7.5. The spectral and temporal evolutions are shown in Fig. 7.5 for both mMSM (top panel) and FEM model (bottom panel). The low pressure of 1.2 bar was chosen to have a zero-dispersion wavelength (ZDW) at 630 nm deep into the visible, as the plasma dynamics tended to blue-shift the soliton dramatically well into the short-wavelength near-IR. Initially, the pulse propagation is dominated by the interplay between anomalous dispersion, self-focusing SPM, and self-steepening [14], leading to strong soliton self-compression down to sub-single cycle duration of 7 fs (less than single-cycle duration at its blue-shifted center wavelength of ~1.5 μm) after propagating 4.8 cm. It can be seen from Fig. 7.5(a) that at the maximum temporal compression point a blue-shifted spectrum is found, essentially forming a supercontinuum with a multiple octave-spanning bandwidth from 1.0-4.0 μm. The mechanism for blue-shifting is described in the later section. The spectrum broadens mainly towards the blue due to plasma formation in the self-compression stage; this is known to blue-shift the soliton [15]. The plasma forms as the leading pulse field strength rises during the self-compression stage. Similar results are found using FEM calculations which are shown in Fig. 7.5 (b-d). However, a little discrepancy are found between mMSM and FEM calculations as the GVD of mMSM starts deviates in the longer wavelength regime than the FEM which is shown in Fig 7.4(a).

7.4.3 Soliton-plasma nonlinear dynamics in mid-IR gas-filled fiber

At the maximum temporal compression, the peak intensity reaches ~70 TW/cm^2 which is enough to ionize the gas and form a plasma (see Fig. 7.5(b)) [1] and creates free electron density $\sim 10^{23} m^{-3}$. Figure 7.6 shows the numerically calculated intensity and nonlinear refractive index change between Kerr and plasma as a function of time for two compressed pulse, one compressed at 4.8 cm and other compressed at 16.8 cm. At the maximum compression point (z = 4.8 cm), the nonlinear refractive index change becomes negative and drops significantly across the compressed pulse which continues remaining trailing edge of the pulse. We observe that the pulse is not fully compressed rather it has pedestal in the trailing edge.

Note that the maximum nonlinear refractive index change Δn is $\sim -5 \times 10^{-4}$ and the maximum nonlinear plasma index is 4 times higher than nonlinear Kerr refractive. Such a significant change in the nonlinear refractive index indicates that the plasma contribution is dominant over the Kerr effect which creates the blue edge part of the spectrum [7]. The nonlinear refractive index change between Kerr and plasma was calculated using [15]

$$\Delta n = n_2 I - \frac{\omega_p^2}{2 n_0 \omega_0^2}, \tag{7.26}$$

The first term in Eq. (7.26) accounts the presence of Kerr, where n_2 is the nonlinear refractive index and I is the intensity of the optical pulse. The second term is due to the plasma formation, where n_0 is the linear refractive index of the filling gas, ω_0 is the central angular frequency in rad.s^{-1}.

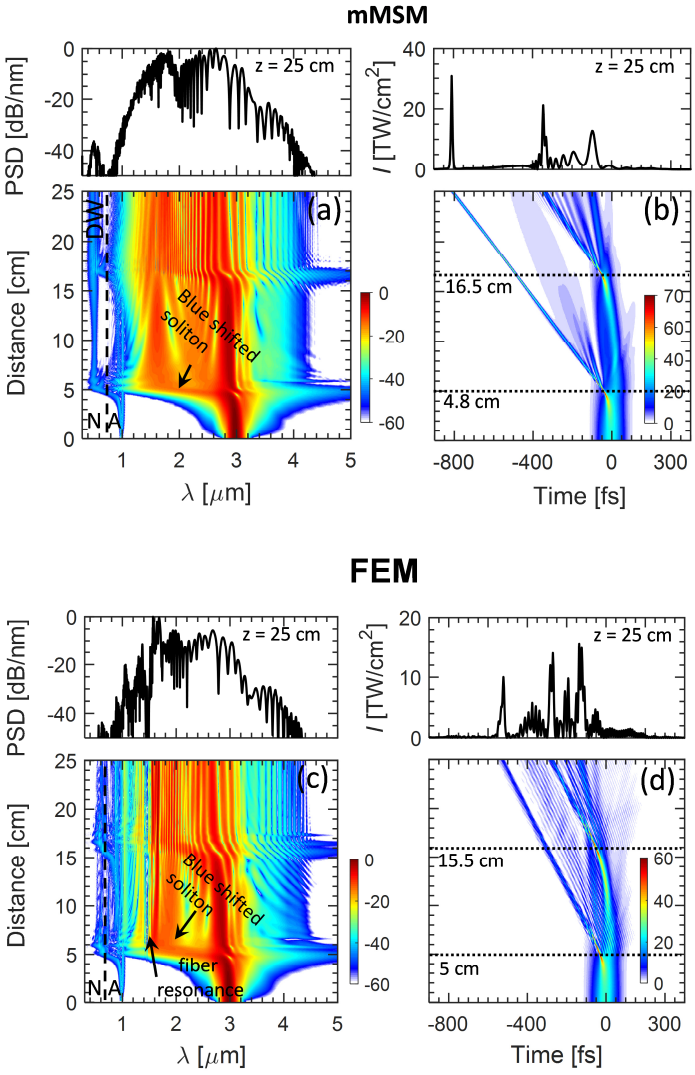

Figure 7.5. Simulation showing (a-c) normalized power spectral density (PSD) [dB] and (b-d) temporal intensity profile [TW/cm^2] of a 20 μJ, 100 fs long pulse in a 43.7 μm core Xe-filled HC-AR fiber under 1.2 bar based on the mMSM (top panel) and FEM (bottom panel). The vertical dashed line in (a) indicates the location of ZDW = 630 nm) N: normal dispersion regime; A: anomalous dispersion regime.

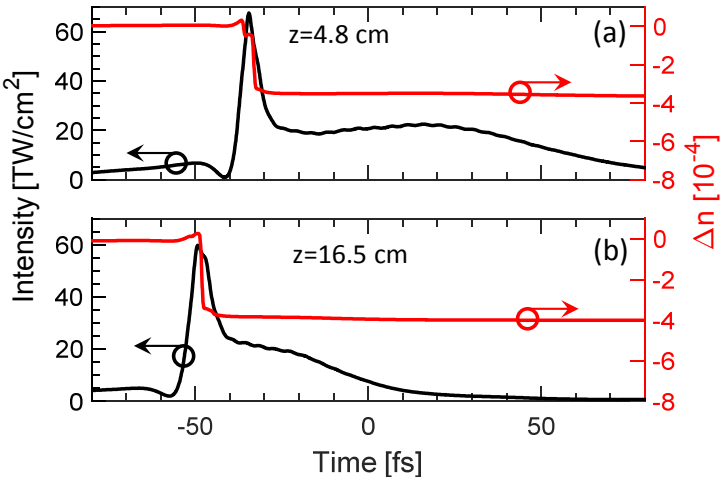

Figure 7.6. Calculated intensity (left) and refractive index change (Δn) (right) at maximum compression (z = 4.8 cm) (a) and comprsion at z = 16.5 cm (b) for a 20 μJ, 100 fs long pulse filled with 1.2 bar Xe in an HC-AR fiber The peak intensity at maximum compression is ~2.9 times higher than the peak intensity of the input pulse.

After the first compression, the peak intensity and free electron density drops which is not sufficient to maintain further ionization over few cm of the fiber. However, the pulse is again compressed down to ~10 fs (which is almost single cycle pulse; a single cycle pulse at 3 μm corresponds to ~10 fs) at 16.8 cm reaching the peak intensity ~60 TW/cm^2 which is shown in Fig. 7.6(b). The compressed pulse has low pedestal at the trailing edge compared to the first compression. At this compression point, the free electron density reaches a value ~0.5×10^{23} which is sufficient to ionize the gas again. The nonlinear refractive index change Δn is ~-2.3×10^{-4} and the maximum nonlinear plasma refractive index increase by a factor of ~2.7. The free electron density and the nonlinear refractive index change as a function of propagation distance are shown in Fig. 7.7. It can be clearly seen in Fig. 7.7 that the ionization process starts at ~4 cm. The maximum ionization occurs at 4.8 cm in which the nonlinear refractive index change drops to its

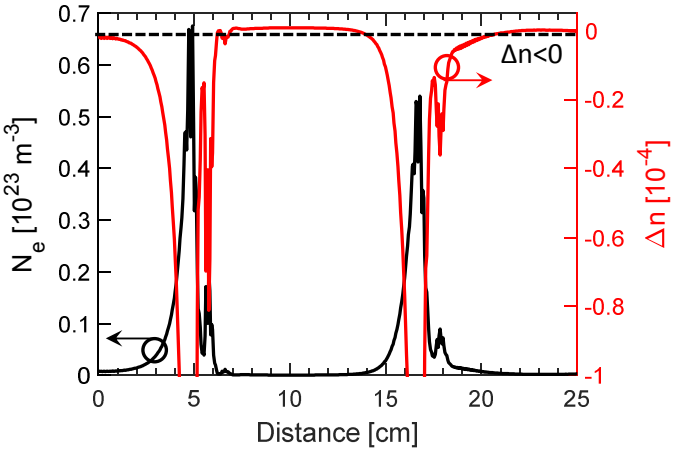

Figure 7.7. Calculated free electron density (left) and nonlinear refractive index change (right) as a function of propagation distance for a 20 μJ, 100 fs long pulse filled with 1.2 bar Xe in an HC-AR fiber.

minimum value and the ionization process continues few cm of the fiber. After that, the free electron drops to its minimum value and fails to have further ionization until 16 cm. The ionization process starts again after 16 cm. The pulse again undergoes strong temporal compression at 16.8 cm. Therefore nonlinear refractive index change drops and emerging broadband blue edge of the spectrum (see Fig. 7.5(a)). This process continues over few cm of the fiber until 18 cm.

7.4.4 Supercontinuum generation and mechanisn of multiple soliton-compression stage

In this section, we will discuss the main mechanism behind the multiple soliton-compression stages in Xe-filled HC-AR fiber. In Fig. 7.8 we plot intensity vs. time, the spectrogram and the normalized PSD vs. frequency at selected distances. Figure 7.8(a) shows that at $z = 3$ cm self-focusing SPM dominates giving a positive nonlinear chirp across the pulse (indicated by the dashed line through pulse center; in the wave-

length vs. time spectrogram we remind that a negative slope corresponds to a positive chirp in this representaion). At the maximum compression point ($z = 4.8$ cm, see Fig. 7.8(b)), the pulse is compressed down to 7 fs. The nonlinear refractive index change (Δn, see the black curve inside the spectrogram) is here strongly negative across the trailing edge of the pulse due to the high intensity in the leading edge of the compressed pulse; this is the nonlocal action of the competing plasma-induced self-defocusing nonlinearity, which results in a negative chirp across the trailing pulse edge that prevents soliton compression of this part of the pulse. In contrast, at the early SPM stage at $z = 3$ cm Δn has only a weak negative value at the trailing edge. It should be emphasized that the maximum nonlinear refractive index change $\Delta n \approx -5 \times 10^{-4}$ and the maximum nonlinear plasma index is ~9 times higher than the nonlinear Kerr refractive index. Such a significant change in the nonlinear refractive index indicates that the plasma contribution is dominant over the Kerr effect. After the first compression, the soliton relaxes, leading to a drop in peak intensity (see Fig. 7.8(c)), and the free electron density drops quickly making the plasma disappear a few cm after the self-compression point. Essentially now a second stage starts with self-focusing SPM dominating (from $z = 6 - 15$ cm). In Fig. 7.8(c) the spectrogram at $z = 15$ cm shows that this allows the trailing edge to accumulate enough positive nonlinear phase shift to flip the chirp from negative to positive. This chirp is then subsequently compensated by the anomalous GVD to give another soliton self-compression stage at 16.5 cm, Fig. 7.8(d), this time down to 10 fs and 60 TW/cm^2 peak intensity. The same dynamics is now seen as in the first stage: a plasma forms during the compression that nonlocally induces a negative chirp on the trailing edge (dashed line), again preventing complete compression. The energy in the trailing edge is reduced compared to the first compression.

It is clear that the steep onset and extinction of the plasma and the nonlocal action of the plasma nonlinearity are key in explaining the multiple compression stages. During the first compression stage self-focusing SPM dominates, but as the plasma turns on ignited by the increasing intensity of the leading edge it induces in a nonlocal fashion a large negative chirp across the trailing edge, which prevents the soliton in forming symmetrically across the pump pulse profile. Consequently only little energy is then retained in the soliton.
The negative nonlinearity of the plasma is then subsequently turned off as the peak intensity of the soliton drops after the self-compression point, the peak power in the uncompressed trailing edge is large enough to initiate an SPM-induced self-focusing chirp-reversal stage leading to an overall positive chirp again and thus build up to another soliton self-compression stage. This will happen repeatedly until the negatively-chirped trailing pulse edge has insufficient peak power to sustain the SPM chirp-reversal stage following the self-compression point and the extinction of the self-defocusing plasma nonlinearity; one could imagine in this way to engineer a sequence of ultrafast few-cycle pulses.

7.4.5 Coherence of the spectrum

Figure 7.9 shows the power spectral density (PSD) and coherence of the spectrum at selected distances. In order get an averaged spectrum and coherence properties, we carried out 50 simulations with different noise seeds. The first order coherence $g_{12}^{(1)}(\omega)$ was calculated using [24]

$$|g_{12}^{(1)}(\omega)| = \frac{< A_i^*(\omega)\tilde{A}_j(\omega) >}{\sqrt{< |\tilde{A}_i(\omega)|^2 >< |\tilde{A}_j(\omega)|^2 >}} \tag{7.27}$$

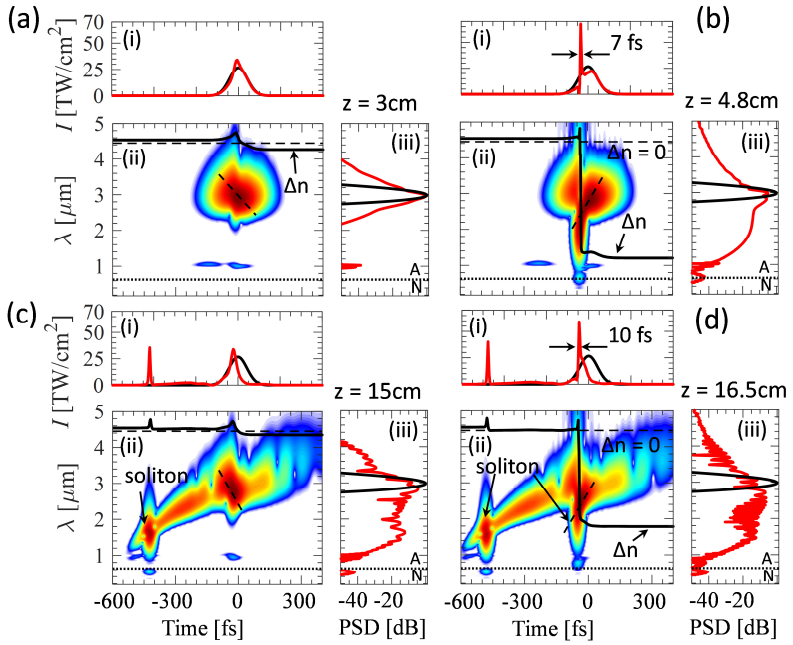

Figure 7.8. Intensity vs. time (i), spectrogram (ii), and norm. PSD vs. frequency (iii) for (a) $z = 3$ cm, (b) $z = 4.8$ cm, (c) $z = 15$ cm, and (d) $z = 16.5$ cm of the simulation in Fig. 7.5. In the spectrogram the horizontal dashed and dotted black lines indicates $\Delta n = 0$ and the ZDW, respectively, the slanted dashed black line through the pulse center indicates the slope of the chirp across the compressed pulse, and the black curve shows the nonlinear refractive index change. The spectrogram was calculated using a 25 fs Gaussian gate pulse. The spectrogram is represented by a dB scale from 0 dB to -50 dB.

where angle brackets denote an ensemble average and complex conjugate is denoted by asterisk . The spectral coherence function allows to investigate stability of an supercontinuum and is primarily a measure of the shot-to-shot phase fluctuations, with $|g_{12}^{(1)}| \approx 1$ signifying perfect coherence. Figure 7.9(b) shows that the spectrum for $z = 4.8$ cm has a good coherence ≈1 over a broad range, while the coherence drops for the second compression stage at the second compression stage $z = 16.5$ cm. The coherence drops at the later propagation stage which is probably due to the fact that the free electron density is sensitive to the

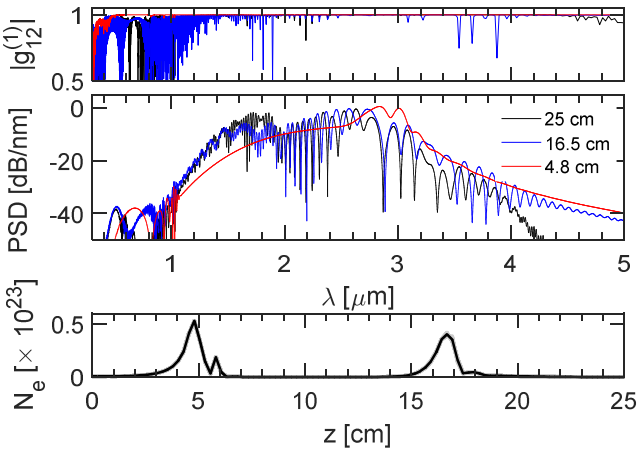

Figure 7.9. (a) Complex degree of first order coherence, (b) power spectral density at z = 4.8 cm (red curve), z = 16.5 cm (blue curve), and z = 25 cm (black curve), and (c) free electron density vs. propagation distance obtain with 20 μJ, 100 fs long pulse filled Xe-filled HC-AR fiber under 1.2 bar. The averaged spectra and coherence properties were found by averaging over 50 simulations with one photon per mode different noise seeds.

noise fluctuation or spectral interference fringes formed after the first compression stage. Figure 7.9 (c) shows that the free electron density is insensitive to the noise fluctuation at the initial propagation stage whereas it is quite sensitive at the later stage of the propagation.

7.5 Soliton-plasma dynamics in the near-IR

We have also investigated the soliton-plasma dynamic in the near-IR pumping at 1 μm. To do so, we simply scale down the fiber parameters and pulse duration by a factor of ~3 compared with mid-IR simulations shown in Fig. 7.5. We fixed the gas pressure to 2 bar. The effective mode index of the LP_{01} mode was caluclated using mMSM method. The simulation results are shown in Fig. 7.10 for 1 μJ (top panel) and 2 μJ (bottom panel). From Fig. 7.10(a-b) it can be seen that multiple soliton compression stages can also be obtained in the near-IR as we observed in the mid-IR.

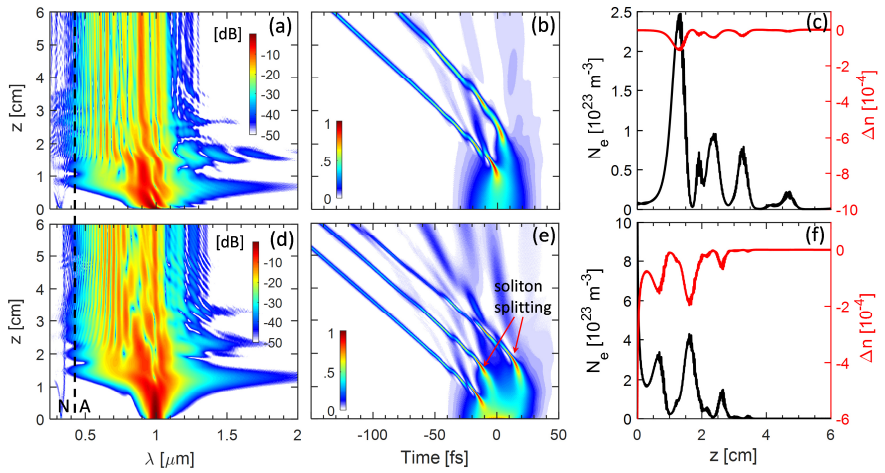

Figure 7.10. (a-d) Spectral, (b-e) temporal evolution, and (c-f) free electron density (left) and nonlinear refractive index change (right) as a function of propagation distance of a 33 fs long pulse in a 14.56 µm core Xe-filled HC-AR fiber under 2 bar for 1 μJ (top panel) and 2 μJ (bottom panel). The vertical dashed line indicates the location of the zero dispersion wavelength (ZDW = 0.42 µm). N: normal dispersion regime; A: anomalous dispersion regime. The effective mode index of the LP_{01} was calculated using mMSM and transmission loss was not considered in the model.

Next we increased the energy to 2 μJ while kept the pressure to 2 bar. Now we observed soliton pulse splitting as in [25]. Due to the increased energy, the gas becomes ionized at the very initial stage of the pulse which is sufficient to form plasma. The soliton pulse splitting happens when the plasma appears at the very initial stage [25].

7.6 Conclusion

In this chapter, soliton-plasma dynamic in a xenon-filled hollow-core anti-resonant silica fiber in the mid-IR has been numerically investigated. Due to the competing self-focusing and self-defocusing nonlinearities from the soliton-plasma interaction we found an intriguing multiple soliton self-compression stage dynamics. This was caused by a sudden onset and quenching of the

plasma during and after self-compression allowing distinct propagation stages with either self-focusing or self-defocusing nonlinearity dominating, as well as the nonlocal action of the plasma, where the leading edge of the self-compressing self-focusing soliton ionizes the gas to affect the trailing edge with a competing self-defocusing nonlinearity. This process could be a novel way of generating a few-cycle pulse sequence. The coherence of such a multi-pulse soliton train is not high. We attribute this to the noise sensitivepulse splitting dynamics, which after the first compression stage results in a fluctuating plasma density that further adds to the noise sensitivity of the second pulse splitting event. This noise amplification of the fluctuating plasma was not observed before, but we have shown that it is an effect that should be taken into consideration, in particular in potential noise sensitive applications.

While we presented simulations using the simplified MS capillary model, we as mentioned found qualitatively similar results using a full FEM model, except for interference from phase-mathcing to narrow-band resonances. It is evident here there is a challenge in designing the anti-resonant wavelengths of the fiber to interfere as little as possible with the soliton-plasma dynamics.

References

[1] W. Chang *et al.*, "Influence of ionization on ultrafast gas-based nonlinear fiber optics," *Opt. Express*, vol. 19, no. 21, pp. 21018, 2011.

[2] W. Chang, P. Hölzer, J. C. Travers, and P. S. J. Russell, "Combined soliton pulse compression and plasma-related frequency upconversion in gas-filled photonic crystal fiber," *Opt. Lett.*, vol. 38, no. 16, pp. 2984, 2013.

[3] K. F. Mak, "Nonlinear optical effects in gas-filled hollow-core photonic-crystal fibers," *PhD Thesis*, 2014.

[4] L. V. Keldysh, "Ionization in the field of a strong electromagnetic wave," *Sov. Phys. JETP*, vol. 20, no. 5, pp. 1307, 1965.

[5] A. M. Perelomov, V. S. Popov, and M. V. Terent'ev, "Ionization of atoms in an alternating electrical field," *Sov. Phys. JETP*, vol. 23, no. 5, pp. 924, 1966.

[6] M. V. Ammosov, N. B. Delone, and V. P. Krainov, "Tunnel ionization of complex atoms and of atomic ions in an alternating electromagnetic field," *Sov. Phys. JETP*, vol. 64, pp. 1191, 1986.

[7] P. Hölzer, "Nonlinear Fiber Optics in Gases and Dilute Plasmas," *PhD Thesis*, 2013.

[8] M. F. Saleh *et al.*, "Theory of photoionization-induced blueshift of ultrashort solitons in gas-filled hollow-core photonic crystal fibers," *Phys. Rev. Lett.*, vol. 107, no. 20, pp. 203902, 2011.

[9] Chang Zenghu, "fundamentals of attosecond optics," *Taylor Fr. Gr.*, vol. 83, no. 15, pp. 2930–2933, 2011.

[10] S. C. Rae and K. Burnett, "Detailed simulations of plasma-induced spectral blueshifting," *Phys. Rev. A*, vol. 46, no. 2, pp. 1084, 1992.

[11] A. V Husakou and J. Herrmann, "Supercontinuum generation of higher-order solitons by fission in photonic crystal fibers," *Phys. Rev. Lett.*, vol. 87, no. 20, pp. 203901, 2001.

[12] P. Sprangle, J. R. Peñano, and B. Hafizi, "Propagation of intense short laser pulses in the atmosphere," *Phys. Rev. E - Stat. Nonlinear, Soft Matter Phys.*, vol. 66, no. 4, pp. 046418, 2002.

[13] Y. Fei, "Hollow core negative curvature optical fibers," *PhD Thesis*, 2013.

[14] D. Novoa, M. Cassataro, J. C. Travers, and P. S. J. Russell, "Photoionization-Induced Emission of Tunable Few-Cycle Midinfrared Dispersive Waves in Gas-Filled Hollow-Core Photonic Crystal Fibers," *Phys. Rev. Lett.*, vol. 115, no. 3, p. 33901, 2015.

[15] P. Hölzer *et al.*, "Femtosecond nonlinear fiber optics in the ionization regime," *Phys. Rev. Lett.*, vol. 107, no. 20, pp. 203901, 2011.

[16] A. N. Kolyadin, A. F. Kosolapov, A. D. Pryamikov, A. S. Biriukov, V. G. Plotnichenko, and E. M. Dianov, "Light transmission in negative curvature hollow core fiber in extremely high material loss region," *Opt. Express*, vol. 21, no. 8, pp. 9514, 2013.

[17] F. Yu and J. C. Knight, "Spectral attenuation limits of silica hollow core negative curvature fiber," *Opt. Express*, vol. 21, no. 18, pp. 21466, 2013.

[18] M. S. Habib, O. Bang, and M. Bache, "Low-loss hollow-core silica fibers with adjacent nested anti-resonant tubes," *Opt. Express*, vol. 23, no. 13, pp. 17394, 2015.

[19] M. Michieletto, J. K. Lyngsø, C. Jakobsen, J. Lægsgaard, O. Bang, and T. T. Alkeskjold, "Hollow-core fibers for high power pulse delivery," *Opt. Express*, vol. 24, no. 7, pp. 7103, 2016.

[20] M. A. Finger, N. Y. Joly, T. Weiss, and P. S. J. Russell, "Accuracy of the capillary approximation for gas-filled kagomé-style photonic crystal fibers," *Opt. Lett.*, vol. 39, no. 4, pp. 821, 2014.

[21] J. C. Travers, W. Chang, J. Nold, N. Y. Joly, and P. St. J. Russell, "Ultrafast nonlinear optics in gas-filled hollow-core photonic crystal fibers [Invited]," *J. Opt. Soc. Am. B*, vol. 28, no. 12, pp. A11, 2011.

[22] M. S. Habib, O. Bang, and M. Bache, "Low-loss single-mode hollow-core fiber with anisotropic anti-resonant elements," *Opt. Express*, vol. 24, no. 8, pp. 8429, 2016.

[23] S. Zahedpour, J. K. Wahlstrand, and H. M. Milchberg, "Measurement of the nonlinear refractive index of air constituents at mid-infrared wavelengths.," *Opt. Lett.*, vol. 40, no. 24, pp. 5794, 2015.

[24] J. M. Dudley and S. Coen, "Coherence properties of supercontinuum spectra generated in photonic crystal and tapered optical fibers," *Opt. Lett.*, vol. 27, no. 13, pp. 1180, 2002.

[25] F. Köttig, F. Tani, J. C. Travers, and P. S. J. Russell, "PHz-Wide Spectral Interference Through Plasma-Induced Fission of Higher Order

Solitons," in Conference on Lasers & Electro-Optics (OSA, San Jose, CA, 2016), paper STu1I.4.

Chapter 8

Conclusion

Hollow-core anti-resonant (HC-AR) fiber filled with noble gas allows to study and control many nonlinear interaction between light and gas. In this chapter, a brief overview of the main results found in this thesis is presented.

Chapter 2 presented the basic linear and nonlinear effects in fibers. The interactions between dispersive and nonlinear effects were discussed in which both effects have important effect on the pulse propagation. New frequencies are generated due to the nonlinear effects whereas dispersion changes the temporal profile of the pulse.

Chapter 3 described the guiding mechanism and modal properties of HC-AR fiber. We proposed a novel HC-AR fiber in which the larger cladding tubes have three smaller adjacent nested anti-resonant (ANAR) tubes inside them. We have thoroughly investigated the effects of the ANAR tubes on the fiber losses and modal properties. Our numerical results confirm that the ANAR tubes play an important role to reduce fiber loss and allow broadband effectively single-mode guidance. These essential properties do not appear when the nested tubes are not adjacent. Our results suggest that the proposed fiber is useful to study gas based nonlinear optics in the mid-IR.

In Chapter 4 we have thoroughly investigated the effect of the shape and position of a single nested anti-resonant element on the overall loss performance of a HC-AR fiber. We intentionally allowed the circular nested element tube to become semi-circular (the nested tubes become semi-circle during fabrication). From the numerical investigations we found that, it is not crucial to have a nested element with a negative

curvature, but its position is much more crucial. These results should give a better intuition when designing anti-resonant fibers with nested elements, and we expect that this will lead to novel designs with improved performance.

Chapter 5 a novel HC-AR fiber is proposed in which the cladding tubes are anisotropic in shape rather than regular circular tubes. We found that the anisotropic shape has improved performance because it simultaneously offers: (a) strong negative curvature in the core, (b) node-free (non-touching) anti-resonant elements, and (c) larger distance from the core to the outer capillary for a given core curvature. We also presented some fabricated HC-AR fibers in this chapter. The transmission and measured loss of HC-AR fibers show that the fibers have broad transmission window and low loss. These properties of HC-AR fibers make an ideal medium to study ultrafast nonlinear optics.

Chapter 6 discussed the modal properties of gas-filled HC-AR fiber. The excellent properties of HC-AR fiber i.e., broad band guidance, low loss (much lower than Kagome fiber), low-light glass overlap, and weakly anomalous dispersion make it possible to study gas-based nonlinear optics. Soliton dynamics and UV light generation is also discussed in this chapter.

Finally, Chapter 7 presented a numerical investigation of the pulse propagation in a xenon-filled hollow-core anti-resonant silica fiber in the mid-IR in the high intensity regime. We observed multiple soliton compression stages which is due to the competing self-focusing and self-defocusing nonlinearities from the soliton-plasma interaction. We explored that they required a sudden onset and quenching of the plasma during and after self-compression allowing distinct propagation stages with either self-focusing or self-defocusing nonlinearity dominating, as well as the nonlocal action of the plasma, where the leading edge of the self-compressing self-focusing soliton ionizes the gas to affect the trailing edge with a competing self-defocusing nonlinearity. The coherence

of such a multi-pulse soliton train is not high. We attribute this to the noise sensitive pulse splitting dynamics, which after the first compression stage results in a fluctuating plasma density that further adds to the noise sensitivity of the second pulse splitting event. This noise amplification of the fluctuating plasma was not observed before, but we have shown that it is an effect that should be taken into consideration, in particular in potential noise sensitive applications.

The results presented in this thesis have identified several areas of research and potential applications for the future investigations. The thesis mainly focuses on the design of various state-of-the-art low-loss HC-AR fibers in the near-IR and mid-IR regime. However, optical properties of HC-AR fiber are still unexplored in the short wavelength (i.e., deep ultra-violet) and longer wavelength regime (i.e., >5 μm) where surface scattering loss and material attenuation of silica is the main limiting factor respectively. Therefore, the future research is suggested to focus on the new HC-AR fiber designs which may have superior optical properties, low attenuation, truly single-mode fiber, and insensitive to bending. Development of this kind HC-AR fiber might be an ideal candidate to generate supercontinuum source beyond 5 μm for various mid-IR applications. Design and fabrication of novel HC-AR fiber taper can be of a particular interest and is also suggested for possible future work. HC-AR fiber taper filled with noble gas can be used to generate bright multiple dispersive waves in the deep ultra-violet or even shorter wavelength range.